

Università degli Studi di Bologna

DOTTORATO DI RICERCA IN FISICA
XXI Ciclo

**METHODS FOR
THE DETERMINATION
OF LUMINOSITY
IN ATLAS WITH LUCID**

Candidate:
DAVIDE CAFORIO

Promoter:
Chiar.^{mo} Prof. MAURIZIO PICCININI

Supervisor:
Dott. ANTONIO SBRIZZI

Doctorate coordinator:
Prof. FABIO ORTOLANI

FIS/01

Contents

1	Introduction	7
2	The Standard Model	11
2.1	Introduction	11
2.2	Gauge theories	12
2.2.1	Electromagnetic interactions	12
2.2.2	Weak interactions	13
2.2.3	Spontaneous symmetry breaking	13
2.2.4	The Standard Model	16
2.3	The search for the Higgs boson in ATLAS	17
2.4	Conclusions	18
3	The ATLAS experiment at the Large Hadron Collider	21
3.1	Introduction	21
3.2	The Large Hadron Collider	22
3.2.1	LHC physics goals	22
3.2.2	LHC design	24
3.2.3	The injection chain	25
3.2.4	Beam structure	25
3.2.5	Beam pipe vacuum and bake-out	26
3.2.6	LHC experiments	26
3.3	The ATLAS detector	27
3.3.1	Magnetic system	29
3.3.2	The Inner Detector	30
3.3.3	Calorimetric System	33
3.3.4	Muon spectrometer	36
3.3.5	Trigger chambers	37
3.3.6	Forward Detectors	38
3.3.7	BCM and MBTS	39
3.3.8	Trigger, Data Acquisition and Detector Control System	40
3.4	Conclusion	43

4	Luminosity	45
4.1	Introduction	45
4.2	Luminosity	46
4.2.1	Definitions	46
4.2.2	Importance of measuring luminosity	46
4.2.3	Relation with collider parameters	49
4.3	Absolute luminosity measurement	50
4.3.1	LHC parameters	50
4.3.2	Physics channels	52
4.3.3	Coulomb scattering amplitude	53
4.4	Relative luminosity monitors	53
4.5	Conclusion	54
5	The LUCID detector	57
5.1	Introduction	57
5.2	Goal of the detector	58
5.3	LUCID project	58
5.4	Principle of detection	59
5.5	Phase I design	61
5.6	Electronics	63
5.7	Calibration	64
5.8	Conclusion	65
6	The LUCID Detector Control System	67
6.1	Introduction	67
6.2	Detector Control System	68
6.2.1	The ATLAS DCS	68
6.3	Finite State Machine	73
6.4	DCS implementation for LUCID	75
6.4.1	LUCID Local Control Station	75
6.4.2	High and low voltage control and monitoring	75
6.4.3	Pressure monitoring	76
6.4.4	Temperature monitoring	79
6.4.5	DCS/TDAQ Communication	82
6.5	FSM implementation for LUCID	82
6.5.1	FSM panels	84
6.5.2	First Beam events	85
6.6	Conclusion	86

7	LUCID Simulation	87
7.1	Introduction	87
7.2	Detector description	88
7.3	Response to a particle gun	92
7.4	Response to inelastic pp collisions	95
7.4.1	Track propagation inside ATLAS and LUCID	98
7.4.2	Tube based information	101
7.4.3	Track based information	103
7.5	Conclusion	106
8	Luminosity monitoring	109
8.1	Introduction	109
8.2	Definition of detected interaction	110
8.3	Monte Carlo simulation	111
8.4	Zero counting method	113
8.4.1	Single side mode	113
8.4.2	Coincidence mode	114
8.5	Hit counting method	118
8.5.1	Single side mode	118
8.5.2	Coincidence mode	120
8.6	Ad-hoc parameterization method	124
8.6.1	Single side mode	126
8.6.2	Coincidence mode	126
8.7	Conclusions	129
9	Conclusions	131

Chapter 1

Introduction

The Standard Model is currently the most reliable description of the fundamental components of nature. Yet, a crucial element of the model is still missing: the Higgs boson, which is meant to be responsible for the spontaneous symmetry breaking of electroweak interactions, necessary to give mass to particles.

The main goal of the Large Hadron Collider (LHC), the largest and most powerful particle collider ever built in the world, is the discovery of the Higgs boson. After the first proposal in the early 1980s, in September 2008 the first beams were circulating along the 27 km rings of the LHC. Physics runs are now expected at the end of 2009.

ATLAS is one of the experiments instrumented at LHC aiming at the discovery of the Higgs boson. Other fundamental discoveries are also expected: for example the evidence of supersymmetric particles and the presence new physics.

Besides the energy delivered by LHC, 14 TeV in the center of mass, another feature of a particle collider is crucial to accomplish this programme: luminosity, which correlates the event rate of a given process to its cross-section. The higher the luminosity, the higher the probability to see a rare event. LHC design instantaneous luminosity is $L = 10^{34} \text{ cm}^{-2} \text{ s}^{-1}$, a value considered high enough to allow discovering of the Higgs boson. A good knowledge of luminosity delivered by LHC is very important because it allows to calculate the cross-sections of any processes by measuring the event rate. Luminosity monitoring is also important to optimize the performance of the collider and of the experiment.

Luminosity in ATLAS can be initially measured by means of the LHC parameters. At a later stage, a dedicated detector (ALFA) will perform accurate measurements of the elastic proton scattering in the Nuclear-Coulomb interference region during low luminosity runs, allowing calibration of the lu-

minosity monitors. A third independent method which can be applied at any stage of the machine operation will exploit physics channels of well known cross-sections like inelastic events or W/Z vector boson production to measure luminosity from event rates.

The LUCID detector is the main luminosity monitor of ATLAS. It is a Cerenkov radiator aimed at detecting the primary particles produced in the pp interactions. The detector is designed to monitor luminosity bunch by bunch over the whole dynamic range of the LHC luminosities and to provide also a measurement of the integrated luminosity for a given physics run.

My PhD. work concerned two subjects:

1. implementation of a Detector Control System for the LUCID detector;
2. study of the performance of LUCID as luminosity monitor.

Soon after the approval of the LUCID project in February 2007, a Detector Control System has been developed and tested during several test beams. It was ready for commissioning in spring 2008 and is now fully integrated into the ATLAS DCS. The development of a Detector Control System is not only a matter of code writing and debugging. A crucial part of the work is concerned with a proper choice of the parameters used to monitor the detector and with learning the principle of functioning of different electronic devices and technologies in order to be able to correctly build up a reliable slow control system and efficiently interface it to the software. Deep knowledge of the physics behind the detectors, the data acquisition techniques and of the overall organization of a complex experiment like ATLAS is also necessary.

Besides the installation and commissioning of LUCID, a fundamental activity in the development of the detector has concerned Monte Carlo simulations. I participated in the analysis of the results of simulations and in the study of the features of the detector. The research activity was focused on linearity issues. Various methods have been developed and their range of validity assessed. The results are promising, and further investigations are foreseen. This thesis is a summary of the work done during these years.

In Chapter 2 an overview of the Standard Model and of the features of the Higgs boson is given. The Large Hadron Collider and the ATLAS experiment are described in Chapter 3. The concept of luminosity is the argument of Chapter 4. Definitions and issues are discussed; the methods for measuring luminosity in ATLAS are described. In Chapter 4 the LUCID detector is described. Special attention has been set on the main features of the detector, such as the pointing geometry which allows background suppression,

the radiation hardness to cope with the severe conditions of the ATLAS environment, and the fast response which allows luminosity monitoring bunch by bunch.

The implementation of the DCS for LUCID is treated in Chapter 6. After a general introduction concerning the goals of the ATLAS DCS, the tools developed for a safe operation of LUCID are described. A description of the first beam event as an example of a realistic physics run condition is also given.

In Chapter 7 the response of LUCID is studied by means of Monte Carlo simulations. The behaviour of the detector is investigated beginning from simple and well defined conditions up to a more realistic situation of a pp event at the interaction point of ATLAS.

Finally, the performance of LUCID as a luminosity monitor is studied in detail in Chapter 8. Several methods for luminosity monitoring are described and discussed, and for each of them accuracies are calculated.

The work described in this thesis has been carried out within the Bologna group of the ATLAS collaboration. Most of the research activities were developed at the CERN laboratories near Geneva.

I wish to thank Paola Giovannini, Adriana Rossi and Jan Soukup for providing me useful information.

I also wish to thank Marco Bruschi, Laura Fabbri, Benedetto Giacobbe, Per Grafström, Vincent Hedberg, Witold Kozanecki, Nicola Semprini Cesari, Roberto Spighi, Sara Valentinetti, Mauro Villa and Simon Mathieu White for stimulating discussions.

Special thanks to Maurizio Piccinini, Carla Sbarra and Antonio Zoccoli for their patience and care.

And very special thanks to my friend Antonio Sbrizzi.

Chapter 2

The Standard Model

The Standard Model foresees the existence of the Higgs boson, which allows spontaneous breaking of electroweak symmetry, explaining how particles acquire mass. The Higgs boson will be searched for at CERN in proton-proton collisions at a center-of-mass energy of 14 TeV in several decay channels. The Branching Ratio of each possible final state depends on the Higgs mass. In any case, experiments aimed at its discovery must cope with the background due to concurrent processes.

2.1 Introduction

The Standard Model is currently the best description of the fundamental structure of matter. During its development, predictions about the existence of new particles have been made: the discovery of the W^\pm and Z^0 gauge bosons in 1983 is regarded as one of the most brilliant achievements in modern physics. Within the framework of the Standard Model, the Higgs boson is responsible for electroweak symmetry to be broken giving mass to the particles. No evidence for the Higgs boson has been observed so far.

An overview of the theoretical basis of the Higgs boson are given in Section 2.2. In Section 2.3 the characteristics of the Higgs boson produced at the LHC collider are summarized, and the relevant features for a detector aimed at its discovery are discussed.

2.2 Gauge theories

Progress in scientific knowledge has shown that symmetry can be regarded as a fundamental principle in nature. In physics, symmetries translate into conservation laws: energy, electric charge etc. Classical electrodynamics is indeed invariant under Lorentz's transformations.

An accurate description of microscopic world ($\sim 10^{-10} m$) needs the formalism of quantum field theories. A gauge theory is a quantum field theory whose Lagrangian is invariant under certain transformations of field variables. These transformations form a symmetry group of the theory: they leave the basic physics of the quantum field unchanged (gauge invariance). Each group parameter is correlated to a vector field (or gauge field). The quanta of a gauge field are referred to as gauge bosons.

2.2.1 Electromagnetic interactions

The Quantum Electrodynamics (QED) is a gauge theory describing the interactions between electrons, positrons and photons which are the quanta of the electromagnetic field. The QED Lagrangian is:

$$L = \bar{\Psi}(i\gamma^\mu\partial_\mu - m)\Psi + e\bar{\Psi}\gamma^\mu A_\mu\Psi - \frac{1}{4}F^{\mu\nu}F_{\mu\nu} \quad (2.1)$$

where Ψ is the electron-positron Dirac spinor, γ are the Dirac matrices, m and e are the electron-positron mass and charge, A_μ is the electromagnetic vector field and $F_{\mu\nu}$ is the gauge invariant field strength tensor defined by:

$$F_{\mu\nu} = \partial_\nu A_\mu - \partial_\mu A_\nu \quad (2.2)$$

The first term in Eq. 2.1 represents the matter field of electrons and positrons, the second term represents the interaction between the electron-positron matter field and the electromagnetic field and the third term represents the electromagnetic field self-interaction.

QED is the simpler example of a gauge theory. The Lagrangian density and all the observables are invariant under the transformation laws:

$$\begin{aligned} \Psi &\rightarrow \Psi' = \exp[iq\alpha(x)]\Psi \\ A_\mu &\rightarrow A'_\mu = A_\mu - \partial_\mu\alpha(x) \end{aligned} \quad (2.3)$$

where $\alpha(x)$ is a real differentiable function. In Group Theory this property is expressed by saying that $U(1)$ is a symmetry group for the theory. This fact has two major consequences:

- according to Noether's theorem, a symmetry of the Lagrangian implies a conserved quantity. In particular, the current $j^\mu = -e\bar{\Psi}\gamma^\mu\Psi$ is conserved, which corresponds to the electrical charge conservation law;
- the theory is renormalizable: it is possible to calculate the expectation value at each order in perturbation theory, for each momentum.

2.2.2 Weak interactions

The first historical evidence of the weak interactions was the neutron β -decay

$$n \rightarrow p + e^- + \bar{\nu} \quad (2.4)$$

observed at the beginning of the twentieth century. The first theoretical explanation of neutron β -decay was given by Fermi who proposed a four fermions point-like interaction in analogy with the QED electron-proton scattering:

$$L_{weak} = \frac{G_F}{\sqrt{2}}(\bar{\Psi}_p\gamma_n\Psi_n)(\bar{\Psi}_e\gamma_n\Psi_\nu) \quad (2.5)$$

The Fermi Lagrangian was generalized one year later by Gamow and Teller in order to explain the transition with nuclear spin flip:

$$L_{weak} = \frac{G_F}{\sqrt{2}} \sum_i C_i (\bar{\Psi}_p \Gamma^i \Psi_n) (\bar{\Psi}_e \Gamma_i \Psi_\nu) \quad (2.6)$$

where Γ^i indicates the scalar ($\Gamma^S = 1$), pseudo-scalar ($\Gamma^P = \gamma_5$), vector ($\Gamma_\mu^V = \gamma_\mu$), axial ($\Gamma_\mu^A = \gamma_\mu\gamma_5$) and tensor ($\Gamma_{\mu\nu}^Y = \sigma_{\mu\nu}$) relativistically covariant operators. The discovery of the parity non conservation in weak interactions and the observation of the existence of only one state of neutrino (left handed neutrino) led, thirty years after the first Fermi proposal, to the V-A theory of weak interactions:

$$L_{weak} = \frac{G_F}{\sqrt{2}} [\bar{\Psi}_p \gamma_n (1 - \gamma_5) \Psi_n] [\bar{\Psi}_e \gamma_n (1 - \gamma_5) \Psi_\nu] \quad (2.7)$$

The main problem with the V-A theory is that it is badly divergent (not renormalizable) for $p_{cm} \simeq 300 \text{ GeV}$.

2.2.3 Spontaneous symmetry breaking

One of the main difficulties in the formulation of the theory of weak interactions is that the vector boson mediating the interaction must be very

massive due to the short range of the weak interaction. Adding a mass term to a Lagrangian is not straightforward since the generic mass term

$$L_A^m = -\frac{1}{2}A_\mu A^\mu \quad (2.8)$$

for a gauge field is not gauge invariant. The mechanism of spontaneous symmetry breaking has been introduced in order to give mass to particles without spoiling the gauge invariance of the theory. In general, given a Lagrangian each continuous symmetry implies the existence of a conservation law (Noether's theorem). When a conservation law is not exact it is possible to introduce in the Lagrangian a term that breaks the symmetry:

$$L = L_{sym} + \epsilon L_{sb} \quad (2.9)$$

Another case of symmetry breaking (spontaneous symmetry breaking) occurs when the Lagrangian of the system is symmetrical but the fundamental state of the Lagrangian breaks the symmetry.

Spontaneous symmetry breaking is not only a quantum related topic: an example in classical physics is the behaviour of ferromagnetic crystals. In ferromagnetic crystals the Lagrangian describing the spin-spin interactions is invariant for $SO(3)$. Above the critical temperature T_C the vacuum describing the spin orientation is symmetrical for $SO(3)$, below the critical temperature the vacuum symmetry is broken to $SO(2)$ and the crystal shows a magnetization along the crystal axis.

A first example of spontaneous symmetry breaking is given by Goldstone mechanism: if an exact global symmetry of a system is broken, the theory contains one massless scalar boson for each broken generator of the symmetry group.

Massive bosons can be introduced in the theory requiring local gauge invariance rather than global invariance (Higgs mechanism). The starting point is the Lagrangian for a complex scalar field

$$L = \partial_\mu \Phi^* \partial^\mu \Phi - V(\Phi^* \Phi) \quad (2.10)$$

with the potential given by

$$V(\Phi^* \Phi) = \mu^2 (\Phi^* \Phi) + \lambda (\Phi^* \Phi)^2 \quad (2.11)$$

The minimum of the potential depends on the value of μ^2 . If $\mu^2 \geq 0$ the minimum of the potential is given by

$$\Phi_1 = \Phi_2 = 0 \quad (2.12)$$

If $\mu^2 < 0$ the minimum of the potential (vacuum expectation value of the Higgs field) is degenerate and is located on the curve

$$\langle |\Phi|^2 \rangle = \frac{\langle \Phi_1^2 \rangle + \langle \Phi_2^2 \rangle}{2} = \frac{-\mu^2}{2\lambda} \equiv \frac{v^2}{2} \quad (2.13)$$

having redefined the complex field in terms of two scalar fields

$$\Phi = \frac{\Phi_1 + i\Phi_2}{\sqrt{2}} \quad (2.14)$$

and v is proportional to the vacuum expectation value of the Higgs field

$$v = \sqrt{\frac{-\mu^2}{\lambda}} \quad (2.15)$$

A one dimensional picture of the Higgs potential is given in Figure 2.1. If we

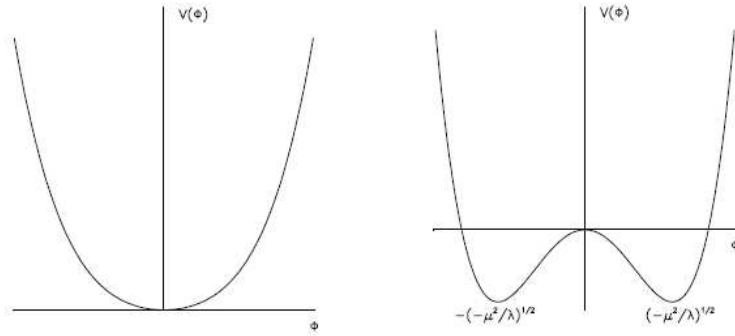


Figure 2.1: *Higgs potential for $\mu^2 \geq 0$ (left) and $\mu^2 < 0$ (right). For $\mu^2 < 0$ the vacuum is degenerate and the symmetry can be spontaneously broken.*

make the substitution

$$\partial_\mu \rightarrow D_\mu = \partial_\mu + iqA_\mu \quad (2.16)$$

and add to the Lagrangian the free gauge fields Lagrangian density

$$-\frac{1}{4}F_{\mu\nu}F^{\mu\nu} \quad (2.17)$$

with

$$F_{\mu\nu} = \partial_\nu A^\mu - \partial_\mu A^\nu \quad (2.18)$$

we get the Lagrangian

$$L = D_\mu \Phi D^\mu \Phi - V(\Phi^* \Phi) - \frac{1}{4} F_{\mu\nu} F^{\mu\nu} \quad (2.19)$$

The Lagrangian in Eq. 2.19 is now invariant for local $U(1)$ gauge transformations:

$$\begin{aligned} \Phi &\rightarrow \Phi' = \exp[iq\alpha(x)]\Phi \\ A_\mu &\rightarrow A'_\mu = A_\mu - \partial_\mu \alpha(x) \end{aligned} \quad (2.20)$$

which means that the electrical charge q is a conserved quantity of the theory. Having imposed the local gauge invariance it is now possible to make a gauge transformation in order to have

$$\Phi = \frac{1}{\sqrt{2}}(\Phi'_1 + v) \quad (2.21)$$

With the choice of this gauge (called unitary gauge) the Lagrangian density is

$$\begin{aligned} L = & \partial_\mu \Phi'_1 \partial^\mu \Phi'_1 - \frac{1}{2}(-2\mu^2)\Phi_1'^2 - \frac{1}{4}F_{\mu\nu}F^{\mu\nu} + \frac{q^2 v^2}{2}A'_\mu A'^\mu + \\ & + \frac{1}{2}q^2(\Phi'_1 + 2v)\Phi'_1 A'_\mu A'^\mu - \frac{\lambda}{4}\Phi_1'^3(\Phi'_1 + 2v) \end{aligned} \quad (2.22)$$

Comparing Eq. 2.19 and Eq. 2.22 it is possible to see that, without destroying the gauge invariance of the theory, a massive complex scalar field (2 degrees of freedom) plus a massless real vector field (2 degrees of freedom) have turned in a massive real scalar field (1 degree of freedom) plus a massive real vector field (3 degrees of freedom).

2.2.4 The Standard Model

According to the Standard Model, all particles can be divided into three categories:

- three families of fundamental fermions:

$$\left\{ \left(\begin{array}{c} \nu_e \\ e \end{array} \right)_L, e_R, \left(\begin{array}{c} u \\ d \end{array} \right)_L, u_R, d_R \right\} \quad (2.23)$$

$$\left\{ \left(\begin{array}{c} \nu_\mu \\ \mu \end{array} \right)_L, \mu_R, \left(\begin{array}{c} c \\ s \end{array} \right)_L, c_R, s_R \right\} \quad (2.24)$$

$$\left\{ \left(\begin{array}{c} \nu_\tau \\ \tau \end{array} \right)_L, \tau_R, \left(\begin{array}{c} t \\ b \end{array} \right)_L, t_R, b_R \right\} \quad (2.25)$$

where ν_e, ν_μ, ν_τ and e, μ, λ are leptons and u, d, c, s, t, b are quarks. Since there is no right handed component of the neutrino, the left handed component is arranged in a doublet while the right handed component is arranged in a singlet;

- four gauge bosons which mediate the electromagnetic and weak interactions between the fundamental fermions. The W^+, W^- and Z^0 are massive bosons mediating weak interactions while the photon γ is massless and mediates the electromagnetic interactions;
- one Higgs boson which is the quantum of the Higgs field used to give mass to the gauge bosons and to the fundamental fermions without destroying the gauge invariance of the theory.

2.3 The search for the Higgs boson in ATLAS

Two limits are given for the Higgs boson mass m_H . The direct search at the e^+e^- collider LEP has led to a lower bound on its mass of 114.4 GeV [1]. Assuming the overall validity of the Standard Model, a global fit [2] to all electroweak data leads to the 95% C.L. $m_H < 144 \text{ GeV}$. Including the 95% C.L. lower limit obtained from LEP, the upper limit is increased to 182 GeV [2]. On the basis of the present theoretical knowledge, the Higgs sector in the Standard Model remains largely unconstrained; yet, an upper limit of 1 TeV can be inferred from unitarity arguments [3]. Further constraints can be derived under the assumption that the Standard Model is valid only up to a cutoff energy scale Λ , beyond which new physics becomes relevant. For a cutoff scale of the order of the Planck mass, the Higgs boson mass is required to be in the range $130 \text{ GeV} < M_H < 180 \text{ GeV}$. If new physics appears at lower mass scales, the bound becomes weaker, e.g., for $\Lambda = 1 \text{ TeV}$ the Higgs boson mass is constrained to be in the range $50 \text{ GeV} < M_H < 800 \text{ GeV}$ [4] [5].

The Higgs boson couples directly to all particles which get mass through the spontaneous symmetry breaking mechanism. The Higgs boson is then expected to be produced in association with heavy particles and to decay in the heaviest particles according to the kinematics of the reaction. The Higgs boson can also couple to $\gamma\gamma, Z\gamma$ and to gluons at one loop level.

The Higgs boson will be searched for at CERN in proton-proton collisions at a center-of-mass energy of 14 TeV , and thus the expected cross-section for

the Higgs boson production in pp interactions must be compared with the cross-section of all the concurrent processes (background). The cross-section for all these processes is reported in Figure 2.2. The Higgs boson will be searched in ATLAS in the following physics channels:

- $H \rightarrow b\bar{b}$ from WH , ZH and ttH in the mass range $80 < m_H < 100 \text{ GeV}$. In this mass range this decay has a branching ratio nearly 100% since the b -quark is the heaviest accessible particle. This channel is difficult to trigger due to the $pp \rightarrow b\bar{b}$ direct reaction;
- $H \rightarrow \gamma\gamma$ in the mass range $90 < m_H < 150 \text{ GeV}$. The background of this channel is given by the processes $q\bar{q} \rightarrow \gamma\gamma$, $gg \rightarrow \gamma\gamma$, $gq \rightarrow q\gamma\gamma$ and $Z \rightarrow e^+e^-$. Reduction of this background relies on the performance of the electromagnetic calorimeter;
- $H \rightarrow ZZ^* \rightarrow 4l$ in the mass range $130 \text{ GeV} < m_H < 2m_Z$. On this channel are crucial the performances of the inner detector and of the electromagnetic calorimeter for electron identification, and of the inner detector in conjunction with the muon spectrometer for muon identification;
- $H \rightarrow ZZ \rightarrow 4l, 2l2\nu$ in the mass range $2m_Z < m_H$. The first of these two decay channels is the same looked for in the $130 \text{ GeV} < m_H < 2m_Z$ range and thus identical requirements are posed on the inner detector, electromagnetic calorimeter and muon spectrometer. The second decay channel requires measurement of the event missing energy due to the escaping neutrino;
- $H \rightarrow WW, ZZ \rightarrow l\nu jj, lljj$ in the mass range $m_H < 1 \text{ TeV}$. The detectors involved in these decay channels are inner detector, electromagnetic calorimeter and muon spectrometer, and hadronic calorimeter for event missing energy measurements.

2.4 Conclusions

According to the Standard Model, the Higgs boson allows electroweak symmetry to be broken, explaining how particles acquire mass. The Higgs boson will be searched for at CERN in proton-proton collisions at a center-of-mass energy of 14 TeV . The Higgs boson is expected to be produced in association with heavy particles and to decay in the heaviest particles according to the kinematics of the reaction. It can also couple to $\gamma\gamma$, $Z\gamma$ and to gluons at one loop level.

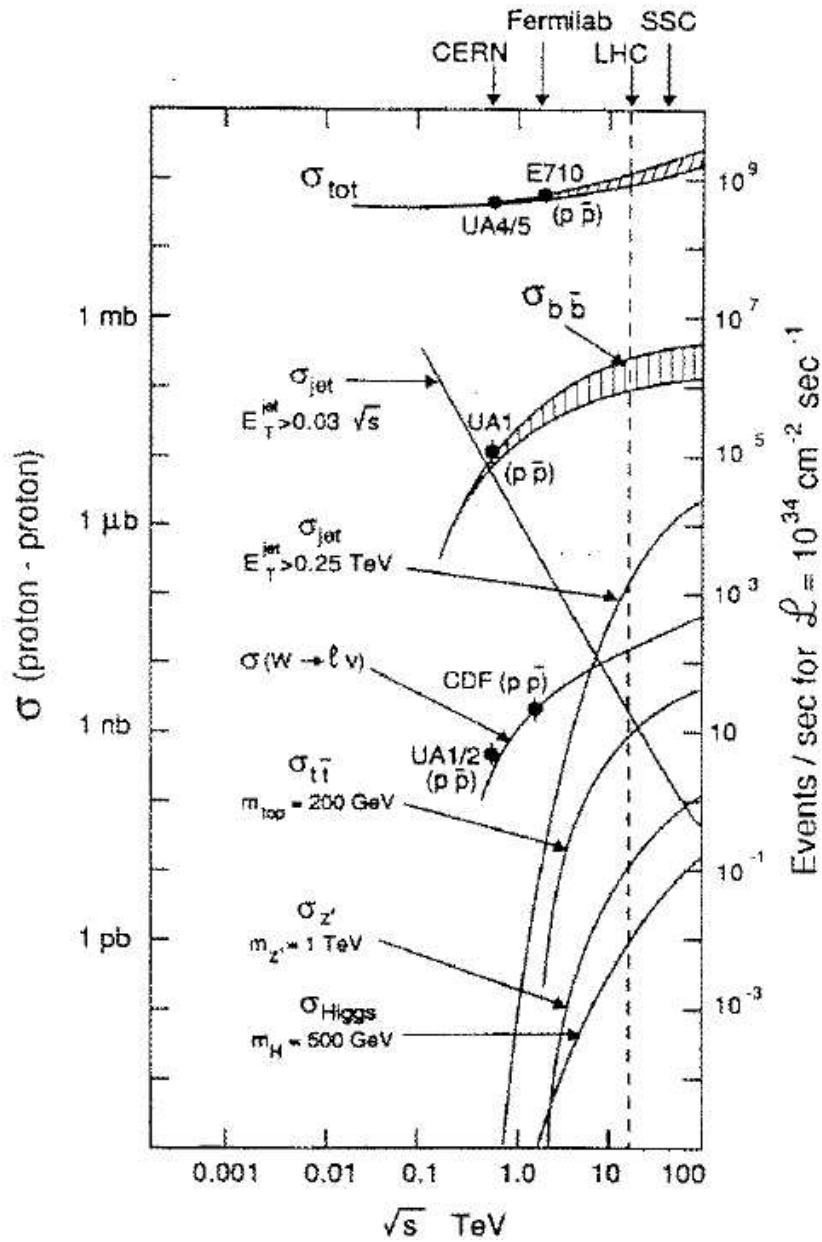


Figure 2.2: Cross-sections for various processes at a center-of-mass energy of 14 TeV and with a luminosity $L = 10^{34} \text{ cm}^{-2} \text{ s}^{-1}$.

A series of features are required to detectors aimed at its discovery in order to reduce the background due to concurrent processes.

Chapter 3

The ATLAS experiment at the Large Hadron Collider

The Large Hadron Collider is a proton-proton collider with a design center-of-mass energy of 14 TeV and a luminosity of $L = 10^{34} \text{ cm}^{-2}\text{s}^{-1}$. Six experiments have been instrumented. Among them, the ATLAS experiment will search for the Higgs boson and new particles, and perform precise measurements W and top -mass.

3.1 Introduction

The Standard Model is a phenomenological model which describes the behaviour of all known elementary particles. The Standard Model predicts the existence of a particle which has not yet been discovered: the Higgs boson, which governs the mechanism of generation of leptons and quarks mass. The Higgs boson is characterized by high mass, in the range $50 \text{ GeV} < m_H < 1 \text{ TeV}$, and low production cross section. Thus any experiment searching for the Higgs boson must rely on colliders which allow exploration on a mass scale beyond the TeV and a high rate for rare events.

In Section 3.2 the Large Hadron Collider, designed so as to reach the highest center of mass energy, and to the highest rates so far, is described.

The ATLAS experiment is a multi-purpose experiment aimed at exploiting the full discovery potential of LHC. The features of the ATLAS experiment are described in Section 3.3.

3.2 The Large Hadron Collider

3.2.1 LHC physics goals

The primary physics goal of LHC is to solve the mass problem of the Standard Model: the Higgs boson. The Higgs mechanism allows the electroweak symmetry to be broken explaining how particles acquire mass. The mass of the Higgs boson, which is unspecified by the theory, is expected to be in the range $50 \text{ GeV} < m_H < 1 \text{ TeV}$. Other physics topics that will be investigated include:

- Supersymmetry: an extension of the Standard Model where every particle has a supersymmetric partner. Supersymmetry is regarded as a solution to the hierarchy problem (difference between theoretical and measured fundamental parameters – couplings or masses). Many of the supersymmetric particles are expected to have masses in the energy range of the LHC;
- evidence of quarks and leptons substructures. Unlike the Standard Model, so-called preon models do not consider quarks and leptons fundamental particles but composed themselves by more fundamental constituents. The goals of this approach are, among the others, to reduce the number of fundamental particles and explain the problem of mass without the Higgs boson;
- evidence of new gauge bosons. Additional gauge bosons are predicted in Grand Unified Theories as mediators of interactions between quarks and leptons and, among other effects, cause proton decay (not yet seen);
- precision measurements of W and top -mass, as well as study of B -physics.

Discovery of new and rare processes relies on luminosity, a quantity which relates event rate R of a given process to its cross-section σ : $R = L \cdot \sigma$. Luminosity is a process independent quantity and depends on the intensity of the beams. The high luminosity requirement (see Figure 3.1) is the reason for the choice of a proton-proton collider. While a proton-antiproton machine has the advantage that both counter-rotating beams can be kept in the same beam pipe, producing the enormous amounts of antiprotons required for the high luminosity is not realistic and it would be more expensive than the proton-proton solution with separated beam pipes.

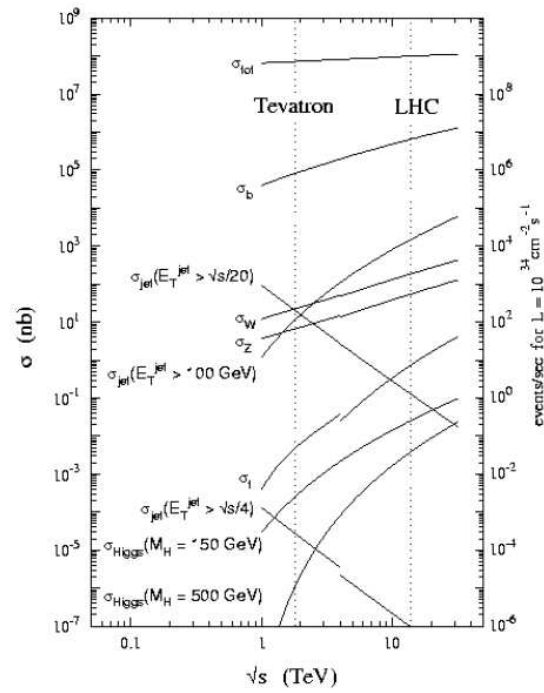


Figure 3.1: *Expected proton-proton cross section as a function of the energy in the centre of mass system at a given luminosity.*

3.2.2 LHC design

The Large Hadron Collider (LHC) is a proton-proton collider built at the CERN laboratories near Geneva in the same tunnel used for the LEP collider. LHC consists of two rings of 27 km circumference located from 50 to 175 m below the ground level (see Figure 3.2).

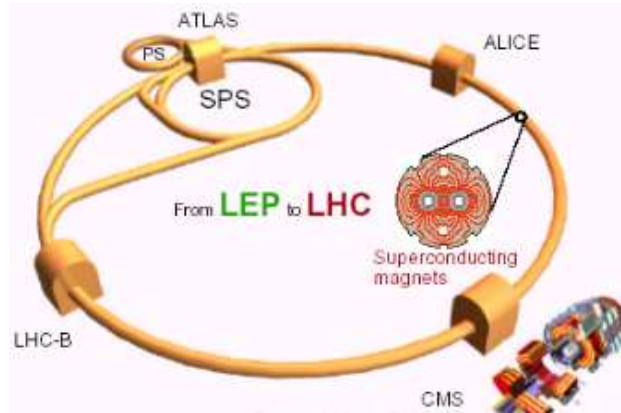


Figure 3.2: Pictorial representation of the LHC tunnel and the experimental caverns.

LHC is designed to produce both proton-proton and heavy ions collisions. The upper limit of the energy which can be reached at LHC is imposed by both geometrical and magnetic constraints. The magnetic field strength required to force particle beams around the collider increases linearly with the beam energy. The highest operational magnetic field for affordable superconducting magnets (8.65 T), together with the requirement that the LHC has to fit inside the existing LEP tunnel, gives the maximum energy of 7 TeV per beam. Hence the protons collide with a center-of-mass energy of 14 TeV . In order to keep the beam onto its circular trajectory, 1232 superconducting dipole magnets generate a magnetic field of 8.4 T at a current of 11.85 kA and a temperature of 1.9 K . The design pp center-of-mass energy is a factor ~ 7 higher than that of the predecessor, the Tevatron $p\bar{p}$ collider at the Fermi National Accelerator Laboratory (Fermilab).

Beams are structured in bunches of particles separated by 25 ns . Two separate beams circulate in opposite directions into two separate ultrahigh vacuum chambers at a pressure of 10^{-10} Torr . Beams are identified by a number: beam 1 travels in the clockwise direction (seen from above), beam 2 runs counterclockwise. Beams share magnetic fields and vacuum chambers in the interaction regions, for a length of about 130 m .

The focusing system consists of 392 superconducting magnetic quadrupoles generating a field of 6.8 T .

3.2.3 The injection chain

In this section only protons will be considered. The source of protons is a *duoplasmatron* [6] which produces beam currents of about 300 mA .

Before entering into the LHC, protons are accelerated through a chain of accelerators.

Linac 2 First operated in 1978, is a linear accelerator for protons and ions. Delivers to the next stadium (PSB) pulsing beams with a rate of 1 Hz and intensity at least 175 mA and energy of 50 MeV . The duration of each pulse ranges from 20 to 150 μs depending on the number of required protons.

Proton Synchrotron Booster (PSB) First operated in 1972, speeds up the beam coming from the Linac 2 to an energy of 1.4 GeV . The accelerator is composed of four superimposed rings, all hosted into a single magnet. Five bunches circulate in each ring. They are then focused and sent through a magnetic deflector into a single line for insertion into the PS.

Proton Synchrotron (PS) Built in 1959 to accelerate protons up to an energy of 28 GeV , is a ring of 600 m in circumference. Changes have been done in order to make it able to set a separation of 25 ns between the bunches.

Super Proton Synchrotron (SPS) First operated in 1976, is a ring of 2 km in circumference originally designed to accelerate protons up to an energy of 300 GeV . It has been adapted so as to accelerate antiprotons, electrons, positrons and heavy ions. It is used as final injector for the LHC bringing the energy of the protons from 26 GeV up to 450 GeV .

In LHC the beams are further accelerated by 16 radiofrequency cavities with a maximum electric field of 5.5 MV/m .

3.2.4 Beam structure

Depending on the operational status of LHC, various filling schemes are foreseen.

During the initial physics operation and machine commissioning, very large bunch spacing is desirable. With large distance between bunches, there are no unwanted collisions in the common vacuum chambers of the experimental insertions and there is no need to force the beams into bended trajectories. This simplifies operations significantly. The simplest schemes use single bunches from the pre-injectors. A total of 44 bunches can be arranged equidistantly around the machine. Leaving one bunch space empty for the beam dump kicker rise time gives 43 bunches arranged around the ring with a spacing of $2.025 \mu s$ [7].

At the design energy, each (nominal) beam contains 2808 bunches separated by $25 ns$. The bunches are gathered in “trains” of 80 (72 filled and 8 empty) separated by 30 empty bunches. In total there are 3564 bunches per beam, of which only 2808 are filled. The time between bunches is limited by the requirements that there should be no additional interactions on each side of the interaction region and the time resolution of the experiments. Each bunch contains $1.15 \cdot 10^{11}$ protons and is $7.55 cm$ long with a transverse length of order mm , except in the interaction points where it reduces to $16 \mu m$.

3.2.5 Beam pipe vacuum and bake-out

If air or other gases are present into the beam pipe serious problems may arise: limitation of the lifetime of the beams, due to interactions between the particles of the beams and the gas molecules; inability to sustain the high electric fields required by various devices such as radio-frequency cavities, separators, etc.

Molecules have a tendency to attach to the surface of metal, and slowly break away when the surface is under reduced pressure. The process of releasing gases from the surface of a material under reduced pressure is known as outgassing. Out gassing can be a source of seemingly spurious vacuum bursts, and must be overcome when re-evacuating a component that has been brought from a vacuum up to atmospheric pressure. Out gassing is sometimes intentionally induced in high vacuum components to remove trapped gases or to boil off any oils collected on the inner surfaces. This procedure is known as a bake out. Raising the temperature of the vacuum vessel frees any gases trapped on the inner surface and forces the molecules back into the system where they can be pumped out.

3.2.6 LHC experiments

Four interaction regions have been instrumented along the tunnel. They host the following experiments:

- **ATLAS (A Toroidal Lhc ApparatuS)** is a multipurpose experiment which will work mainly at a high luminosity of $L = 10^{34} \text{ cm}^{-2}\text{sec}^{-1}$ to discover the Higgs and signatures of new physics;
- **CMS (Compact Muon Solenoid)** pursues the same physics programme of ATLAS by using different and complementary technologies. It will work mainly at a high luminosity of $L = 10^{34} \text{ cm}^{-2}\text{sec}^{-1}$;
- **LHCb** will perform accurate measurements in the flavour physics of the B meson (CP violation) at a luminosity of $L = 10^{32} \text{ cm}^{-2}\text{sec}^{-1}$;
- **ALICE (A Large Ion Collider Experiment)** is dedicated to the study of the gluon-quark plasma and will work with a luminosity $L = 10^{27} \text{ cm}^{-2}\text{sec}^{-1}$.

Two more experiments are placed along the tunnel:

- **LHCf** will measure γ and π^0 spectra in the very forward region at luminosity $L = 10^{29} \text{ cm}^{-2}\text{sec}^{-1}$. The aim is the calibration of Monte Carlo simulations in cosmic rays studies.
- **TOTEM** is aimed at measuring the elastic pp cross section with a luminosity of $L = 10^{29} \text{ cm}^{-2}\text{sec}^{-1}$.

3.3 The ATLAS detector

ATLAS (A Toroidal LHC ApparatuS) is a general-purpose particle detector designed to exploit the full discovery potential of the LHC [8] [9] [10]. The overall detector has a cylindrical symmetry with a total length of 42 m and a radius of 11 m (see Figure 3.3). The detector is installed 100 m under ground level at the interaction Point 1 of the LHC. The underground facilities of the experiment are shown in Figure 3.4.

The observable cross-section of the most interesting processes occurring in pp collisions at $\sqrt{s} = 14 \text{ TeV}$ is small over a large part of mass range, hence it is an important design consideration to operate at high luminosity and to perform high resolution measurements. The detector requirements are the following:

- very good electromagnetic calorimetry for electron and photon identification and measurements, complemented by fully-coverage hadronic calorimetry, for accurate jet and missing transverse energy (E_T^{miss}) measurements;

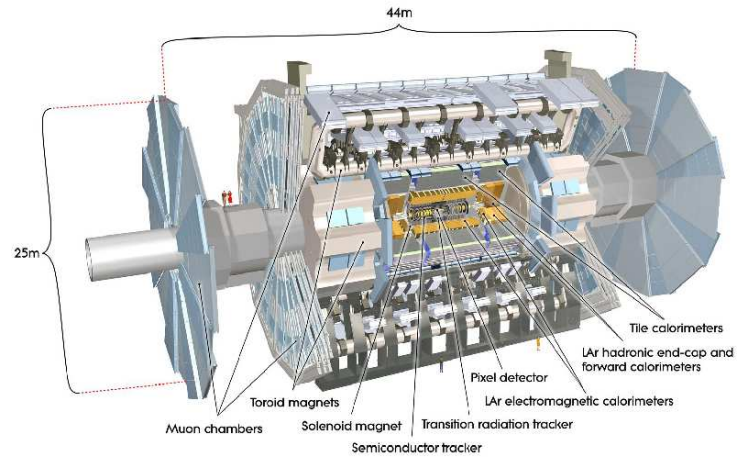


Figure 3.3: *The ATLAS detector.*

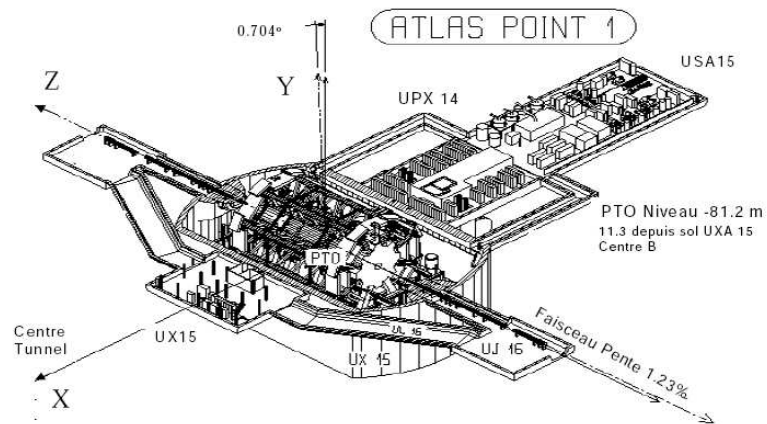


Figure 3.4: *Overview of the underground facilities at Interaction Point 1. UX15 is the experimental cavern where the ATLAS detector is mounted. USA15 is the service area hosting the back-end electronics. The ATLAS coordinate system is also shown.*

- high precision muon momentum measurements, with the capability to guarantee accurate measurements at the highest luminosity, using the external muon spectrometer alone;
- efficient tracking at high luminosity for high p_T lepton momentum measurements, electron and photon identification, τ lepton and heavy flavour identification and full event reconstruction capability at lower luminosity;
- large acceptance in pseudorapidity (η) with almost full azimuthal angle (ϕ) coverage. The azimuthal angle is measured around the beam axis, whereas pseudorapidity relates to the polar angle θ , measured from the beam direction: $\eta = -\ln\left(\tan\frac{\theta}{2}\right)$;
- triggering and measurements of particles at low p_T thresholds, providing high efficiencies for most physics process of interest for the ATLAS experiment.

The detector is composed by five parts: the Inner Detector (ID), the calorimeters, the muon spectrometer, the forward detectors and the magnetic system. The ID tracks the particles trajectory, then the particle energy is measured by the calorimeters, and at the end of the detector the muon spectrometer detects the very penetrating muons. The magnetic system is designed to bend the charged particle trajectory in the ID and in the muon spectrometer, in order to measure the particle momentum.

In the following, the standard ATLAS coordinate system is used: the beam direction defines the z -axis, and the $x - y$ plane is transverse to the beam direction, the x -axis pointing to the center of the LHC ring whereas the y -axis points to the surface.

3.3.1 Magnetic system

ATLAS is characterized by two different magnetic field systems required for particle identification and momentum measurements:

Central Solenoid (CS), a super-conducting solenoid, providing a magnetic field of $2 T$, installed around the Inner Detector cavity with a radius of $1.2 m$ and a length of $5.3 m$. It is optimized to minimize the amount of material in front of the electromagnetic calorimeter;

a large super-conducting air-core toroid system, with an open structure to minimize the contribution of multiple scattering to the momentum

resolution, constituted by eight **Barrel Toroids (BT)** and two **End-Cap Toroids (ECT)**, providing a magnetic field of $1.5 T$, arranged outside the calorimetry. Over the range $|\eta| \leq 1$, magnetic bending is provided by the large barrel toroid, extending over a length of $25 m$, with an inner bore of $9.4 m$ and an outer diameter of $20.1 m$. For $1.4 < \eta < 2.7$, charged tracks are bent by the two end-cap magnets inserted into both ends of the barrel toroid. They have a length of $5 m$, an inner bore of $1.64 m$ and an outer diameter of $10.7 m$. Over $1 < \eta < 1.4$, usually referred to as the transition region, magnetic deflection is provided by a combination of barrel and end-cap. Each toroid consists of eight flat coils assembled radially and symmetrically around the beam axis. This magnet configuration provides a $2 T$ field that is mostly orthogonal to the muon trajectories. The average toroidal magnetic field will be $\simeq 0.5 T$.

3.3.2 The Inner Detector

The Inner Detector (ID) is designed to reconstruct tracks and decay vertexes. Using additional information from the calorimeter and muon systems, the inner detector also contributes to electron, photon, and muon identification, and supplies extra signatures for short-lived particle decays. The momentum and vertex resolution requirements from physics call for high-precision measurements to be made with fine granularity detectors, given the very large track density expected at the LHC. The layout of the Inner Detector is shown in Figure 3.5. The outer radius of the ID cavity is $105 cm$. It consists of three

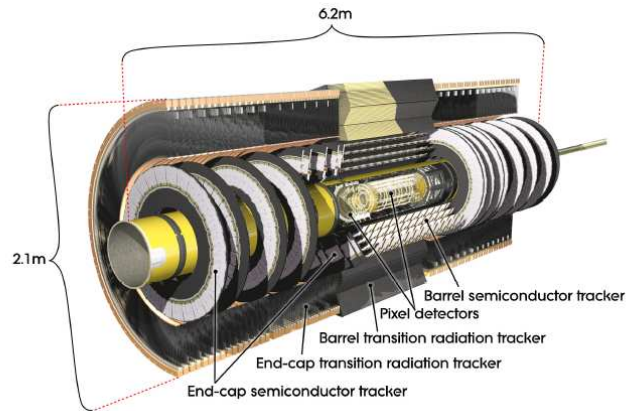


Figure 3.5: *The Inner Detector.*

units: a barrel section extending over ± 80 cm with respect to the interaction point, and two identical end-caps covering the rest of the cylindrical part. In the barrel region, high-precision detector layers are arranged on concentric cylinders around the beam axis, while the end-cap detectors are mounted on disks perpendicular to the beam axis. The highest granularity around the vertex region is provided by semi-conductor pixel and strip detectors, also called ‘‘Precision tracking detectors’’. The difference between strips and pixels is mainly geometry, pixels being closely spaced pads capable of good two dimensional reconstruction while strips give a better spatial resolution in one coordinate than the other. The number of layers of the semiconductor detectors must be limited due to the material they introduce and their high cost.

The inner detector will see of the order of 1000 charged particle tracks for every beam crossing at the design luminosity of the LHC [11].

Pixel detector

The Pixel Detector is the nearest detector to the interaction point. It measures the particle impact parameters and the decay vertexes of short living particles such as B hadrons and τ leptons.

A Pixel sensor is a 16.4×60.8 mm² wafer of silicon with 46,080 pixels, 50×400 μ m² each. The pixel layers are segmented in $R - \phi$ and z and arranged such that at least three pixel layers are crossed by each track (see Figure 3.6). The intrinsic accuracies in the barrel are 10 μ m ($R - \phi$) and

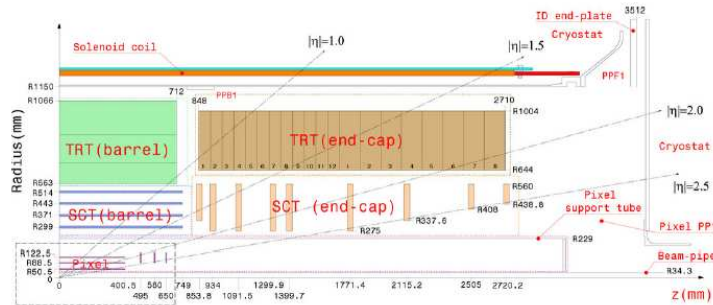


Figure 3.6: Plan view of a quarter-section of the ATLAS inner detector showing each of the major elements with its active dimensions.

115 μ m (z) and in the disks are 10 μ m ($R - \phi$) and 115 μ m (R).

The system consists of three barrels at average radii of $\simeq 5$ cm, 9 cm and 12 cm respectively, and five rings on each side, with 11 cm inner radius and

20 *cm* of outer radius, which complete the angular coverage. The thickness of each layer is expected to be about 1.7% of a radiation length (X_0) at normal incidence. The Pixel detector provides three precision measurements over the full acceptance, and mostly determines the impact parameter resolution and the ability of the Inner Detector to find short-lived particles such as B hadrons and τ leptons.

The readout of the pixels, approximately 80.4 million channels, requires the use of advanced techniques. In addition each chip must be radiation-hard to withstand over 300 *kGy* of ionizing radiation and more than $5 \cdot 10^{14}$ neutrons per *cm*² over ten years of operation of the experiment.

Semiconductor Tracker

The semiconductor tracker (SCT) system is designed to provide track precision measurements in the intermediate radial range, contributing to the measurement of momentum, impact parameter and vertex position. The modules are arranged such that eight strip layers are crossed by each track (see Figure 3.6). In the barrel region, this detector uses small-angle (40 *mrad*) stereo strips to measure both coordinates, with one set of strips in each layer parallel to the beam direction, measuring $R - \phi$. Each side of a detector module consists of two 6.4 *cm* long, daisy-chained sensors with a strip pitch of 80 μm . In the end-cap region, the detectors have a set of strips running radially and a set of stereo strips at an angle of 40 *mrad*. The mean pitch of the strips is also approximately 80 μm . The intrinsic accuracies per module in the barrel are 17 μm ($R - \phi$) and 580 μm (z) and in the disks are 17 μm ($R - \phi$) and 580 μm (R). The total number of readout channels in the SCT is approximately 6.3 million. Tracks can be distinguished if they are separated at least by $\sim 200 \mu\text{m}$.

Transition Radiation Tracker

A large number of hits (typically 30 per track, with a maximum of 36, [11]) is provided by the 4 *mm* diameter straw tubes of the Transition Radiation Tracker (TRT), which enables track-following up to $|\eta| = 2.0$. The TRT only provides $R - \phi$ information, for which it has an intrinsic accuracy of 130 μm per straw. In the barrel region, about 50000 straws are parallel to the beam axis and are 144 *cm* long, with their wires divided into two halves, approximately at $\eta = 0$. In the end-cap region, about 320000 37*cm* long straws are arranged radially in wheels. The total number of TRT readout channels is approximately 351000.

3.3.3 Calorimetric System

The ATLAS calorimetric system is composed by an electromagnetic liquid argon calorimeter (EM) covering the pseudorapidity region $|\eta| < 3.2$, an iron-scintillating tiles hadronic calorimeter (HCAL) covering the pseudorapidity region $|\eta| < 1.7$, two liquid argon hadronic calorimeters (HEC) covering the region $1.5 < |\eta| < 3.2$ and two forward liquid argon calorimeters (FCAL) covering the region $3.1 < |\eta| < 4.9$ (see Figure 3.7). Over the pseudorapidity

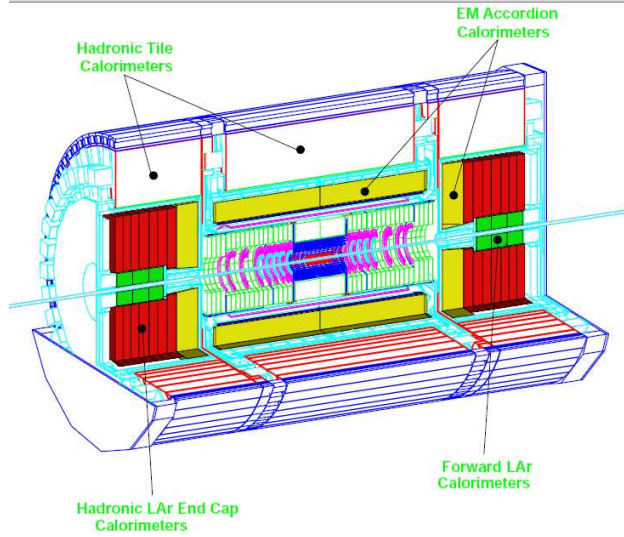


Figure 3.7: *The ATLAS calorimetric system.*

range $|\eta| < 1.8$ the EM calorimeter is preceded by a presampler detector, used to correct for electron energy losses in the material upstream the calorimeter.

The design goal for the energy resolution for the electromagnetic, hadronic and forward calorimeters are:

- $\frac{\Delta E}{E} = \frac{10\%}{\sqrt{E}} + 1\%$ for the electromagnetic calorimeter
- $\frac{\Delta E}{E} = \frac{50\%}{\sqrt{E}} + 3\%$ for the hadronic calorimeters
- $\frac{\Delta E}{E} = \frac{100\%}{\sqrt{E}} + 10\%$ for the forward calorimeter.

Electromagnetic calorimeter

In order to realise the full physics potential of the LHC, the ATLAS electromagnetic calorimeter must be able to identify efficiently electrons and

photons within a large energy range (5 GeV to 5 TeV), and to measure their energies with a linearity better than 0.5 %.

The ElectroMagnetic calorimeter is divided in a barrel region ($|\eta| < 1.475$) and an end-cap region ($1.375 < |\eta| < 3.2$). The end-cap EM calorimeter is composed by two concentric wheels. Due to the high radiation level the EM calorimeter makes use liquid argon as active medium and lead as absorber medium. The output signal is read by accordion-shaped kapton electrodes. The lead thickness of the absorber plates has been tuned as a function of the pseudorapidity in order to optimize the calorimeter energy resolution. The total thickness of the EM calorimeter is more than $24 X_0$ in the barrel and more than $26 X_0$ in the endcap. In the region dedicated to precision measurements (the barrel and the outer end-cap wheel) the EM calorimeter is divided in three longitudinal samplings. The first sampling uses longitudinal strips in the η direction (the η strips have a pitch of 4 mm). This sampling is used as a preshower detector in order to enhance particle identification and to perform precise position measurement in the η direction. The first sampling has a constant thickness of $6X_0$ all along the η direction and is segmented with a constant granularity $\Delta\phi = 0.1$ along ϕ and with a granularity varying from $\Delta\eta = 0.003$ and $\Delta\eta = 0.1$ along η . The second sampling has a thickness of $24X_0$ and is segmented in squares of $\Delta\eta \times \Delta\phi = 0.025 \times 0.025$. The third section has a granularity of $\Delta\eta \times \Delta\phi = 0.05 \times 0.025$ and a thickness varying from $2X_0$ to $12X_0$. For $|\eta| > 2.5$ (end cap inner wheel) the calorimeter is segmented in two longitudinal sections (two samplings). All the calorimeter cells point to the interaction region and the total number of channels is $\simeq 200000$. In order to correct for the energy loss in the material before the EM calorimeter, a presampler constituted by an active liquid argon layer between 1 and 0.5 mm is used. In the region between the barrel and the endcap the presampler is complemented with a scintillator slab.

Hadronic calorimeters

An important parameter in the calorimeter design is its thickness: it has to provide good containment for hadronic showers and reduce punch-through into the muon system to a minimum. The total thickness of the calorimeter support. This thickness has been measured to be sufficient to reduce punch-adequate to provide good resolution for high energy jets.

The ATLAS hadronic calorimeter is divided in three different detectors due to the radiation level dependence on the pseudorapidity. In the region $|\eta| < 1.7$ an iron scintillating tile calorimeter is used, for the end-cap and forward calorimeters liquid argon detectors are used. The ATLAS hadronic calorimeter system has been designed with a thickness of about 10 inter-

action lengths. The large coverage in pseudorapidity permits good E_T^{miss} measurement.

The hadronic **Tile Calorimeter** is a sampling calorimeter using iron and scintillating tiles. It is divided in a barrel ($|\eta| < 1.0$) and two extended barrels ($0.8 < |\eta| < 1.7$). Radially it extends from 2.28 m to 4.23 m. Longitudinally it is made of three layers (1.4, 4.0 and 1.8 interaction lengths). Each of the three sections is divided in 64 wedges. Each wedge is made of a set of iron tiles partially staggered in the z direction. The void space between the iron tiles is filled with scintillating tiles. The scintillating tiles are readout with optical fibres located along the outside faces of each wedge. Several optical fibres are grouped and read out by a single photomultiplier. The readout cells are fully projective in ϕ but only partially projective in η and the readout granularity is in the first two sections and in the third section.

Liquid Argon end-cap Calorimeter Each end-cap liquid forward calorimeter is composed of two wheels of 2.03 m outer radius. The wheel near the interaction point is composed by 25 mm copper plates, while the wheel farther from the interaction point is composed by 50 mm copper plate as a cost saving solution. In both wheels the 8.5 mm gap between the various plates is filled with liquid argon and divided in four gaps by three parallel electrodes. Longitudinally the first wheel is divided in two sections of 8 and 16 layers respectively, the second wheel is divided in 16 layers. Along the azimuth each wheel is divided in 32 wedges. The readout granularity for both wheels is up to $|\eta| < 2.5$ and up to $|\eta| < 3.1$.

The **Liquid Argon Forward Calorimeter** covers the pseudorapidity region $3.1 < |\eta| < 4.9$ and is located at a distance of 4.7 m from the interaction point (the front face of the forward calorimeter is recessed of about 1.2 m with respect to the electromagnetic calorimeters front face). The location of the detector imposes severe conditions due to the high level of radiation. In order to install 9.5 interaction lengths in the forward liquid argon calorimeter a high density design is needed. The forward calorimeter is constituted by three sections (a first copper section and two tungsten sections). Each section is constituted by a metal matrix of equally spaced longitudinal channels. The channels are filled with concentric rods and tubes. The gap between the rod and the tube (245 mm) is filled with liquid argon. The total number of channels (for the sum of the two half forward calorimeters) is 3584.

3.3.4 Muon spectrometer

Only a tiny fraction of pp collisions corresponds to interesting standard model processes and an even smaller fraction to new physics. Muons, especially those with high- p_T (transverse momentum) and those that are isolated (from other activity in the detector), will be much more common in these interesting events than in the background, and thus provide important means to identify such events and to determine their properties. The ATLAS detector has been designed to be efficient in the detection of muons and to provide precise measurement of their kinematics up to one TeV .

The Muon Spectrometer dominates the size of the ATLAS experiment with its outer diameter of $\simeq 22\text{ m}$ (see Figure 3.8). The ATLAS Muon

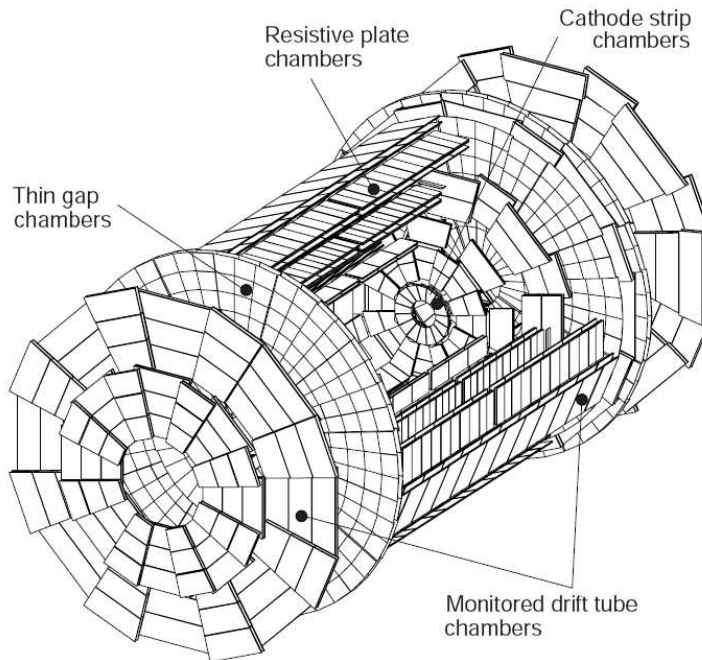


Figure 3.8: *ATLAS muon spectrometer layout.*

Spectrometer is based on deflection of muon tracks in the magnetic field provided by a system of three large super-conducting air-core toroid magnets instrumented with separate function trigger, the Resistive Plate Chambers (RPC) and the Thin Gap Chambers (TGC), and high-precision tracking chambers, the Monitor Drift Tubes (MDT) and the Cathode Strip Chambers (CSC). The trigger chambers must identify bunch crossings, trigger with well-defined p_T thresholds and measure a second coordinate orthogonal to that measured in the muon chambers. In the barrel, the chambers are arranged

on three concentric cylinders whereas in the end-caps they are arranged in four disks. This arrangement is such that particles from the interaction point traverse three stations of chambers.

Precision chambers

The positions of these stations are optimized for full coverage and momentum resolution. The barrel chambers form three concentric cylinders with the beam axis, at radii of about 5, 7.5 and 10 m . They cover the pseudorapidity range $|\eta| < 1$. The end-cap chambers cover the range $1 < |\eta| < 2.7$ and are arranged in four disks at distances 7, 10 and 14 and 21 m from the interaction point, concentric with the beam axis. The precision measurement of the muon tracks is made in the $R - z$ projection, in a direction parallel to the bending direction of the magnetic field; the axial coordinate (z) is measured in the barrel and the radial coordinate (R) in the transition and end-cap regions. Over most of the η -range, a precision measurement of the track coordinates in the principal bending direction of the magnetic field is provided by Monitored Drift Tubes (MDT). At large pseudo-rapidities and close to the interaction point, Cathode Strip Chambers (CSC) with higher granularity are used in the innermost plane over $2 < |\eta| < 2.7$, to withstand the demanding rate and background conditions. Optical alignment systems have been designed to meet the stringent requirements on the mechanical accuracy and the survey of the precision chamber.

3.3.5 Trigger chambers

The trigger system covers the pseudorapidity range $|\eta| < 2.4$. Resistive Plate Chambers (RPC) are used in the barrel and Thin Gap Chambers (TGC) in the end-cap regions as shown in figure 1.10. The trigger chambers for the ATLAS spectrometer serve a threefold purpose:

- bunch crossing identification, requiring a time resolution better than the LHC bunch spacing of 25 ns ;
- a trigger with well-defined p_T cut-offs in moderated magnetic fields, requiring a granularity of the order of 1 cm ;
- measurement of the second coordinate in a direction orthogonal to that measured by the precision chambers, with a typical resolution of 5 – 10 mm .

Alignment

The requirements on the momentum resolution of the spectrometer call for an accuracy of the relative positioning of chambers traversed by a muon track of the order of the intrinsic resolution and the mechanical tolerances of the precision chambers. Over the large global dimensions of the spectrometer, however, it is not possible to stabilize the dimensions and positions of the chambers at the $30 \mu m$ level. Therefore, chamber deformations and positions are constantly monitored by means of optical alignment systems and displacements up to $\sim 1 cm$ can be corrected for the offline analysis.

3.3.6 Forward Detectors

The Forward Detectors of the ATLAS experiment are designed to perform a variety of measurements ranging from the absolute luminosity determination, the measurement of the total pp cross section (σ_{tot}) and a wide program of forward physics, including diffractive processes, both inclusive and exclusive ones.

LUCID

LUCID is a Cerenkov detector consisting of 32 projective aluminium tubes filled with C_4F_{10} mounted at a distance of $17 m$ on each side of the interaction point. The pseudo-rapidity range covered is $\eta = [5.6, 5.9]$.

LUCID is the ATLAS detector dedicated to monitoring of LHC luminosity, and is designed to have a sufficient time resolution in order to identify individual bunch crossings.

A complete description of the detector is given in Chapter 5.

Zero Degree Calorimeters

The Zero Degree Calorimeters are compact calorimeters located at approximately zero degrees to the incident beams on either side of the interaction point of ATLAS (IP1), $140 m$ downstream from the IP in a slot in the neutral beam absorbers (Target Absorber Neutral, TAN), at the point where the beam pipe branches off into two pipes, covering a pseudorapidity range $\eta > 8.3$. They thus observe forward going neutral particles that are produced in heavy ion (HI), pA or pp collisions.

The proposed ZDCs are versatile devices in that they serve to study heavy ion physics, pp physics, and provide a tool to tune both the HI and pp beams. They are designed to be as radiation hard as practicable, since the radiation levels in the position of the ZDC are extremely high.

The ZDCs would be run as a subsystem of ATLAS, and as such would allow correlation of forward particle production with those particles observed in the main ATLAS detector. While their resolution will eventually deteriorate due to radiation, they will serve as an adjunct to ATLAS in detecting neutral particles in the forward direction for some time after the start of high luminosity operation.

In Heavy Ion running the ZDCs have proven to be a valuable tool in luminosity calibration.

ALFA

The main purpose of the ALFA (Absolute Luminosity For ATLAS) detectors is to measure the LHC absolute luminosity with unprecedented accuracy for hadron colliders ($\sim 3\%$ [12]). The basic idea is to measure the rate of elastic scattering of protons in the Nuclear-Coulomb interference region at angles order of microrad which, for LHC, means detecting particles at ~ 1 mm from the beam. ALFA will thus be placed close to the LHC beam, using “Roman Pots”.

The system is constituted by two Roman Pot stations mounted at a distance of 240 m on each side of the interaction point containing plastic scintillator fibers with a spatial resolution of 30 μ m. The pots are cylindrical vessels, which are separated from the machine vacuum and equipped with bellows that allow the pots to approach the beam.

3.3.7 BCM and MBTS

Beam Conditions Monitor

Circulating beam losses, occurring far from the ATLAS region, will most likely be detected by machine protection devices. However, local magnet failures occurring close to P1 are also possible. The primary goal of the BCM system is to detect the early signs of beam instabilities and protect the experiment against damaging beam losses by initiating a beam abort if necessary. Moreover, BCM will provide real-time monitoring of instantaneous particle rate close to the interaction point and will be able to distinguish between normal collisions and background events. The separation between signals and background is based on the timing of the BCM signals.

Two BCM detector stations are placed symmetrically around the interaction point at $|z| = 1.84$ m. Each BCM station is made of 4 detector modules placed symmetrically around the beam line at $\phi = 0^\circ, 90^\circ, 180^\circ$ and 270° . The detector modules are mounted on the Beam Pipe Support

structure which supports the Pixel detector as well, with sensors located at $r \simeq 55 \text{ mm}$, corresponding to pseudorapidity of $\eta \simeq 4.0$. It is worth mentioning that BCM in ATLAS will be the first BCM system based on bunch-by-bunch measurements.

In order to distinguish between normal collisions and background, the BCM should be sensitive to single minimum ionising particles (MIPs). This sensitivity is also required for the luminosity measurement. The hostile radiation environment and high rate of interactions pose harsh requirements for BCM sensors and electronics. In 10 years of LHC operation, the radiation field at sensor location is expected to amount to about 10^{15} particles (mostly pions) per cm^2 and an ionisation dose of $\simeq 0.5 \text{ MGy}$.

Minimum Bias Trigger Scintillator

The Minimum Bias Trigger Scintillator (MBTS) will be used to trigger on Minimum Bias events at early days running. The MBTS counters consist of one plane with 2×8 scintillator segments on each side of the interaction point, mounted in front of the LAr end-cap connected to different photomultiplier tubes. There are 2 segments in η (inner and outer), 8 segments in ϕ . The MBTS detector covers a pseudorapidity range of $1.9 < |\eta| < 3.8$.

3.3.8 Trigger, Data Acquisition and Detector Control System

There are three major systems that enable the coherent operation of the different subdetectors as a single entity, namely the High Level Trigger (HLT), the Data Acquisition (DAQ) and the Detector Control System (DCS). These three systems are addressed in the common framework of the TDAQ/DCS project.

Trigger system

The trigger system selects bunch crossings containing interesting interactions. The bunch crossing rate at LHC being of 40 MHz , at design luminosity there will be about 25 interactions per bunch crossing leading to an interaction rate of $\simeq 10^9 \text{ Hz}$. The online triggering system will be capable of selecting only interesting physics signatures reducing the acquisition rate to approximately 100 Hz . Therefore, within seconds the data flow from the detector has to be reduced by a factor 10^7 while retaining an excellent efficiency for new physics channels such as Higgs boson decays. This is achieved by defining

different trigger levels (LVL1, LVL2 and LVL3 also called Event Filter) as shown in Figure 3.9.

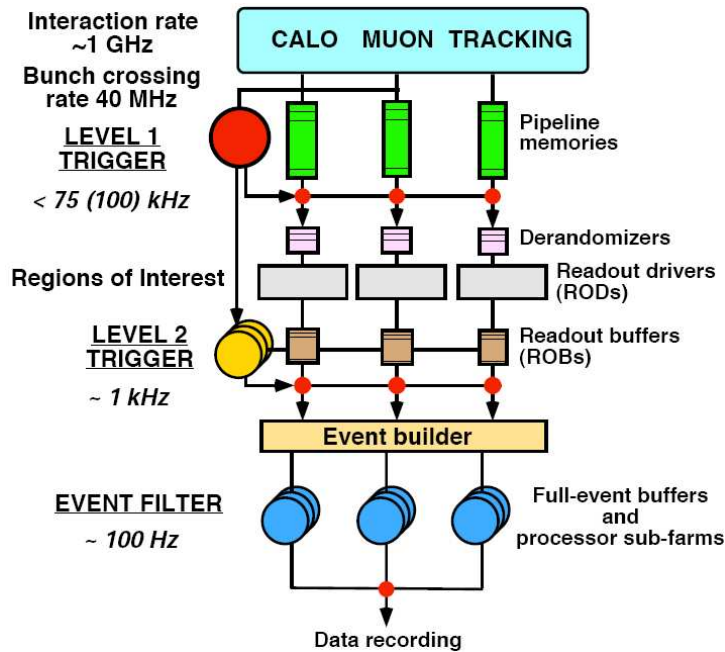


Figure 3.9: *The ATLAS trigger and data acquisition system. The data accepted by the Level 1 trigger are stored in the derandomizers before the serial readout.*

Level 1 Trigger The LVL1 trigger uses reduced-granularity data from a subset of detectors (mainly muon trigger chambers and calorimeters, with prescaled contributions of MBTS and LUCID). The LVL1 trigger accepts data from these detectors at the full LHC bunch-crossing rate of 40 MHz. At this stage, the subdetectors are treated individually. The LVL1 latency, which is the time to form and distribute the LVL1 trigger decision, is 2 μs and the maximum output rate is limited to 100 kHz by the capabilities of the subdetector readout systems and the LVL2 trigger. During the LVL1 processing, the data from all parts of the ATLAS detector are held in pipeline memories of the front-end electronics. The LVL1 trigger must identify unambiguously the bunch crossing containing the interaction of interest and introduce negligible dead-time.

Level 2 Trigger The LVL2 trigger reduces the rate from about 100 kHz to 1 kHz, with a latency ranging from 1 to 10 ms depending on the

event. Events passing the LVL1 trigger are held in Read Out Buffers (ROB) until the LVL2 trigger takes the decision to either discard the event or to accept it. After an event is accepted, the full data are sent to the Event Filter processors via the event builder. In order to reduce the data transfer bandwidth from the ROBs to the LVL2 trigger processors the LVL2 algorithms work on subsets of the detector data called Regions of Interest (RoI) and defined in the LVL1.

Event Filter The Event Filter trigger uses the full event data together with the latest available calibration and alignment to make the final selection of events for permanent storage. At LVL3 a complete reconstruction is possible with decision times up to about 1 s. The Event Filter must achieve a data storage of 10 – 100 MB/s by reducing both the event rate and the event size.

Data Acquisition system

The Data Acquisition system (DAQ) system handles the distribution of data from the Read Out Drivers (ROD) filled by the front-end electronics to mass storage, and the overall monitoring and control of the data taking. For this reason, the system has been factorized in two major components: DataFlow and Online Software. The DataFlow provides the functionality of receiving and buffering detector data from the ROD, distributing events to the High Level Triggers (HLT) and forwarding selected events to mass storage. The Online Software system controls the overall experiment: it provides run control, configuration of the HLT and DAQ system and manages data taking partitions. This component constitutes the interface point between the DAQ system and the DCS.

Detector Control System

A Detector Control System must ensure the safe and coherent operation of the whole experiment. The system is based on the experience gained during the design and maintenance of the slow controls of the OPAL experiment [13] at LEP.

A detailed description of the ATLAS Detector Control System is given in Chapter 6.

3.4 Conclusion

The Large Hadron Collider is a proton-proton ring collider recently completed at the CERN laboratories in the outskirts of Geneva. The beam pipe is placed in a tunnel 27 *km* long, at about 100/*m* under the ground level. The collider features a center-of-mass energy of 14 *TeV* with a design luminosity of $L = 10^{34} \text{ cm}^{-2} \text{ s}^{-1}$.

Six experiments have been set up along the tunnel. Among them, ATLAS is a multi-purpose experiment, the main physics goals being the discovery of the Higgs boson, evidence for supersymmetric particles and new gauge bosons, *W* and *top*-mass, study of CP-violation and B-decays.

Chapter 4

Luminosity

In the first phase, absolute luminosity in ATLAS will be measured by means of LHC parameters with an accuracy of $\sim 20\%$. An accuracy of 10% can be reached by measuring event rates of well known physics processes. At a later stage, a measurement of the elastic scattering amplitude with the ALFA detector will provide the most accurate result (3%).

4.1 Introduction

The event rate of a physical process in a collider is a function of both beam energy and luminosity of the collider. As an example, for a Higgs boson of mass $m_H = 150$ GeV in the production channel $gg \rightarrow H$, the cross-section is predicted to increase by 3 orders of magnitude by increasing the center-of-mass energy from 1 to 14 TeV [14].

As will be discussed in Section 4.2, luminosity depends on the number of particles circulating into the beams and on the transverse dimensions of the beams: the higher the number of particles and the smaller the beam size, the higher the number of collisions.

Luminosity measurement techniques used in the ATLAS experiment are described in Section 4.3.

A fundamental step in the luminosity measurement programme is the calibration of the luminosity monitors in order to extrapolate the luminosity under the different LHC beam conditions, as shown in Section 4.1.

4.2 Luminosity

4.2.1 Definitions

Given a certain physical process of cross-section (σ), *instantaneous* luminosity (L) is the interaction rate (R) per cross section unit:

$$L = \frac{R}{\sigma}. \quad (4.1)$$

Integrated luminosity (\mathcal{L}) is the number of interactions (N) per cross section unit in a certain time interval (t):

$$\mathcal{L} = \frac{N}{\sigma}. \quad (4.2)$$

Then \mathcal{L} can be expressed as the integral of L over t :

$$\mathcal{L} = \int_0^t L(t') dt' \quad (4.3)$$

Instantaneous luminosity is expressed in units of $cm^{-2}s^{-1}$, whereas integrated luminosity is expressed in units of cm^{-2} . Instantaneous and integrate luminosity are two definitions of *absolute* luminosity. The term *relative* luminosity indicates a variation of luminosity in a certain period of time.

Absolute luminosity can be obtained either by measuring the event rate (R) of a physical process with a well known cross-section (σ) or by means of the collider parameters.

4.2.2 Importance of measuring luminosity

LHC center-of-mass energy of 14 TeV is expected to be high enough to allow the discovery of the Higgs boson. Yet, there exist different models describing the production mechanism of the Higgs boson. A measurement of Higgs boson production cross section would allow to discriminate the model which best describes the characteristics of this particle. In Figure 4.1, the expected uncertainty in the measurement of the Higgs boson production cross section at LHC is plotted against its mass for various decay channels [8]. In the mass region where the Higgs boson is expected, the main sources of systematics uncertainty on cross section measurements is given by the luminosity which set a lower limit on the precision of the measurement.

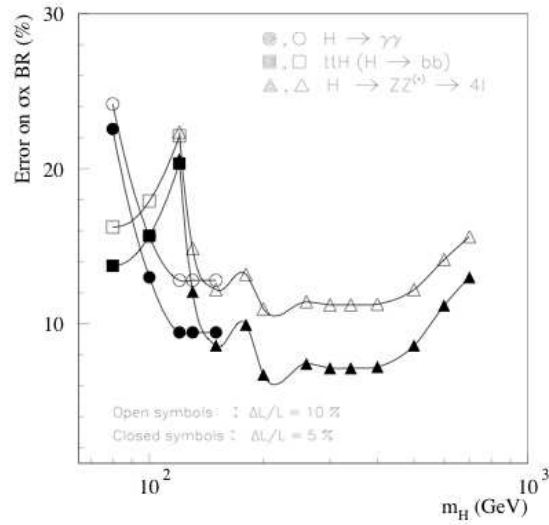


Figure 4.1: Total systematic uncertainty on the measurement of the Higgs-boson production cross section times branching ratio as a function of the Higgs mass, assuming an integrated luminosity of 300 fb^{-1} . Results are shown for various decay channels and two values of the systematic uncertainty on the luminosity (10% and 5% [8]).

Measuring instantaneous luminosity is also important to monitor beam conditions. Luminosity decreases exponentially with time ($\tau \simeq 14$ h [15]) because of loss in intensity and beam emittance. The reduction is due to collisions at the interaction points, collisions with the residual gas molecules in the LHC beam pipe, and a blow up of the RMS beam sizes due to the Coulomb interaction of the particles within each bunch [8].

Luminosity block

One important issue in measuring the integrated luminosity is insuring that it stays constant over the integration time interval. The smallest possible time interval depends on the method of luminosity measurement and could be chosen such that the statistical uncertainty is smaller than the systematical error. Typical values from other experiments are $O(\text{min})$. A luminosity block [16] is “a time interval, for which the integrated, dead-time- and prescale-corrected luminosity can be determined”. Luminosity blocks help to keep the losses to a minimum in view of failure scenarios in DAQ, data production, analysis, detector and machine operation. This is usually done by excluding from the analysis luminosity blocks in which failures occur. The biggest amount of tolerable losses due to these failures sets an upper limit on the size of a luminosity block. A complete run of length $O(1 h)$ would, under realistic failure scenarios, be too big to be taken as a single luminosity block. In particular, as is the case in currently running experiments, runs are often terminated just after failures have occurred. In this respect it seems difficult to find a solution without sub-dividing a run into smaller pieces of time.

The instantaneous luminosity of the machine decreases exponentially with a time constant of $O(6..28 h)$, with a nominal time constant of $14 h$. This would mean that under nominal conditions, the luminosity would drop by 1% after 10 minutes. In order to open up trigger bandwidth, it is expected to change the pre-scale values at time intervals $O(1 h)$. Also, some aspects of data taking, event reconstruction or data analysis depend on the instantaneous luminosity. The size of the luminosity block should be small enough compared to the required granularity from these aspects.

In order to calculate the corrected luminosity for each luminosity block, a complete set of parameters needs to be determined, recorded and made available. For the analysis of a specific dataset, this complete set consists of the name of the trigger chain used to trigger the dataset; at least one luminosity measurement; level-1 live-time fraction for this trigger chain; pre-scale values for the trigger chain; information (counter values) on lost events due to failures at Level-2, EF, production, and skimming; data quality information. Most of the items above are all time dependent. The most natural

way to store this information is in a database, where the relevant numbers are retrieved as a function of a unique index that identifies the relevant luminosity block. This index is called a Luminosity Block Number (LBN) [16]: “a number, which uniquely tags a luminosity block within a run”.

4.2.3 Relation with collider parameters

By definition, luminosity is a process-independent quantity and is completely determined by the properties of the colliding beams.

In case of colliders with bunched beams, absolute luminosity is related to the geometrical and kinematic characteristics of the beams [17]:

$$L = f N_1 N_2 \sqrt{(\vec{v}_1 - \vec{v}_2)^2 - \frac{(\vec{v}_1 \wedge \vec{v}_2)^2}{c^2}} \int \rho_1(\vec{x}, t) \rho_2(\vec{x}, t) d\vec{x} dt \quad (4.4)$$

where f is the bunch revolution frequency, N_1 and N_2 are the number of particles in the bunches (protons in LHC), \vec{v}_1 and \vec{v}_2 are the velocities of the particles and ρ_1 and ρ_2 are the densities of the particles in the bunches and \vec{x} is the spatial coordinate. Particle densities are normalized such that their integral on the whole space is 1. Under the assumption that:

- a) the two bunches are identical in transverse profile;
- b) their charge distribution on the plane perpendicular to the direction of motion is gaussian;
- c) the profiles of the bunches are independent of position along the bunch;
- d) the particle distributions are not altered during collision;

Equation 4.4 can be written as [18]:

$$L = f \frac{N_1 N_2 n_b \gamma}{4\pi \epsilon_n \beta^*} F \quad (4.5)$$

where n_b is the number of bunches per beam, γ the relativistic factor, ϵ_n the normalized transverse emittance (the average action related to phase space density and reflects the process of bunch preparation), β^* the *beta function* of Courant-Snyder [19] at the collision point (it describes the focusing properties of the magnetic lattice) and F a reduction factor due to the vertical crossing angle at the interaction point. A crossing angle between the beam directions is needed when the number of bunches is larger than 156 in order to avoid additional collisions not at the Interaction Point.

The crossing angle reduction factor is expressed as [18]:

$$F = \frac{1}{\sqrt{1 + \left(\frac{\theta_c \sigma_z}{2\sigma^*}\right)^2}} \quad (4.6)$$

where θ_c is the crossing angle between the two beams at the interaction point, σ_z the mean square length of the bunches along z axis and σ^* the transverse dimension of the bunches. If collisions are perfectly head-on (i.e. crossing angle is zero), luminosity is given by [18]:

$$L = f n_b \frac{N_1 N_2}{4\pi \sigma_x \sigma_y} \quad (4.7)$$

where $\sigma_{x,y}$ characterize the Gaussian transverse profiles of the beams (standard deviations of the bidimensional gaussians in the transverse directions x and y) and are assumed to be equal for the two bunches.

Equation 4.7 can be used to evaluate L by measuring the geometrical and kinematic parameters of the beams. Alternatively, if the cross section of a given reaction is known, luminosity can be evaluated from Equation 4.1 by measuring the event rate of that reaction.

4.3 Absolute luminosity measurement

4.3.1 LHC parameters

Absolute luminosity can be extracted from LHC machine parameters under specific beam conditions [20] in which systematic uncertainties are minimized by means of Equation 4.5.

The number of particles circulating N_1 and N_2 will be continuously measured to roughly 10^{-2} accuracy and maybe better under certain conditions [21]. Bunch number and frequency are also well known.

The reduction factor F due to crossing angle can be removed by reducing the number of bunches such that no crossing angle is needed. Another effect giving rise to systematic uncertainties is the beam-beam effect, due to electromagnetic forces experienced by the beams as they cross each other. This effect may result in beam blow-up and reduced beam lifetime. This effect can be reduced by both reducing the number of bunches and the beam intensities.

Van der Meer scan

A general formula for the absolute luminosity as a function of the beam displacement (d), valid under the assumption that the crossing angle between the beams is equal to zero can be written as follows [18], [20]:

$$L(d) = fn_b \frac{N_1 N_2}{2\pi \sqrt{\sigma_{1x}^2 + \sigma_{1y}^2} \sqrt{\sigma_{2x}^2 + \sigma_{2y}^2}} e^{-\frac{d^2}{2\sqrt{\sigma_{1x}^2 + \sigma_{1y}^2} \sqrt{\sigma_{2x}^2 + \sigma_{2y}^2}}} \quad (4.8)$$

where f is the revolution frequency, n_b the number of bunches, N_1 and N_2 the number of particles constituting each bunch (beam intensities), d the separation between the beams and σ_{ix} and σ_{iy} , with $i = 1, 2$, the transverse dimensions of the bunches. If we make the further assumption that the transverse dimensions of the bunches are equal ($\sigma_{ix} = \sigma_{iy} = \sigma$), then the formula assumes the following simplified form:

$$L(d) = fn_b \frac{N_1 N_2}{4\pi\sigma^2} e^{-\frac{d^2}{4\sigma^2}} \quad (4.9)$$

This formula can be used to directly measure the transverse dimensions of the two colliding beams. This method is called separation scan (or Van der Meer scan [22]). The idea is to displace the beams with respect to each other at regular steps and measure the counting rate, which is proportional to luminosity (see Eq. 4.1), with an appropriate monitor. The LHC will operate with round beams. Separation scans will be performed in both the vertical (y) and horizontal (x) directions. The counting rate is plotted versus the separation (an example for a scan on a plane is reported in Figure 4.2) and a fit is performed to calculate the σ of the beams.

Taking into account the assumption under which Equation 4.9 is valid (no crossing angle, thus a reduced number of bunches with respect to the nominal filling scheme) and that beam-beam effects at design luminosity are negligible only for separations within 0.3σ [23], separation scans are performed at a low luminosity ($L \simeq 10^{30}/cm^{-2}s^{-1}$), with less than 156 bunches per beam and at reduced beam intensity $N \simeq 10^{10}$.

The main sources of systematics from the collider which have to be taken into account concern the relative position of the beams at the interaction point (nominal separation); the beam intensities; the differences between the real beam shape and the assumed one (gaussian); the background. These contributions depend both on the instrumentation (LHC monitors) and the beam quality and their values are under study.

In the beginning, the overall uncertainty with this method is expected to be of the order of 20 %, while the aim is to reduce it to below 5 % after some years of experience [24].

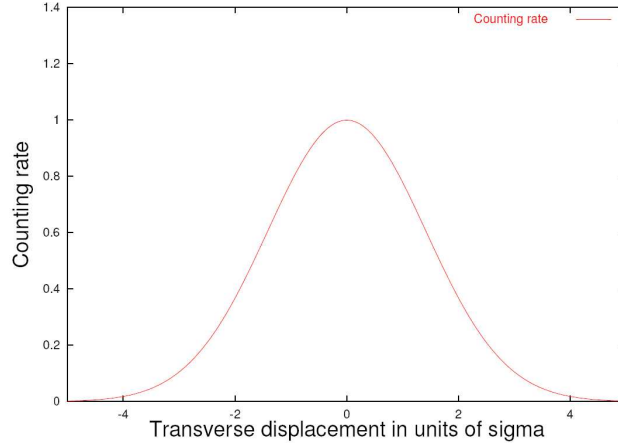


Figure 4.2: *Principle of luminosity measurement using transverse beam displacement.*

4.3.2 Physics channels

As mentioned in section 4.2, absolute luminosity can be determined by measuring the event rate R of a process with a well known cross-section, i.e. by counting the number of particle decays reconstructed inside a detector. The more abundant and well known the production mechanism of the particle, the more accurate the resulting luminosity measurement. Two methods can be used:

- a) measurement of the event rate R of inelastic events. This processes can be easily measured but the cross-section is known with low accuracy;
- b) measurement of the event rate R of more rare events. The cross-section is well known.

A precise knowledge of the parton distribution functions (PDF) in the proton and of the partonic cross-section is needed.

With current PDF uncertainties and taking into account detector related effects, absolute luminosity can be determined from leptonic decays of W/Z bosons to about 10% [16]. Using early LHC data to constrain the PDFs will help to reduce this uncertainty.

The high rate of W/Z decays allows online relative luminosity monitoring with high statistical precision. At $10^{34} \text{ cm}^{-2} \text{ s}^{-1}$, a statistical precision of 5% (1%) is expected after 10 s (3 min) [16].

4.3.3 Coulomb scattering amplitude

Absolute luminosity can be determined by measuring the elastic scattering amplitude.

The elastic scattering amplitude is a superposition of the strong (f_s) and Coulomb (f_c) amplitudes. The latter dominates at small values of the momentum transfer $-t = (p\theta)^2$, where p is the beam momentum and θ the forward scattering angle. A simplified expression of the differential elastic cross section is [18]:

$$\lim_{t \rightarrow 0} \frac{d\sigma_{el}}{dt} = \frac{1}{L} \frac{dN_{el}}{dt} \Big|_{t=0} = \pi |f_c + f_s|^2 \simeq \pi \left| \frac{2\alpha_{em}}{-t} + \frac{\sigma_{tot}}{4\pi} (\rho + i) e^{B\frac{t}{2}} \right|^2 \quad (4.10)$$

where α_{em} is the electromagnetic fine-structure constant, ρ is the ratio between the real and the imaginary parts of the forward elastic scattering amplitude and B is the nuclear slope for pp scattering. If the differential cross section is measured over a large enough range, the unknown parameters σ_{tot} , ρ , B and L can be determined by a fit to the data.

The advantage of this method is that by measuring only elastic scattering it allows to measure luminosity, total cross section (elastic + inelastic) and the interference parameter ρ .

At the nominal energy of the LHC, the strong amplitude is expected to equal the electromagnetic amplitude for $|t| = 0.00065 \text{ GeV}^2$. This corresponds to a scattering angle of $3.5 \text{ } \mu\text{rad}$ [25]. The measurement of the Coulomb amplitude requires detectors sitting a few millimeters from the beam (e.g. with so-called Roman Pots). A reduced intensity and zero crossing angle are required. To measure scattering angle of order of microrads, beam divergence is reduced with a high β^* at the collision point ($\beta^* = 2625 \text{ m}$ [12]).

This measurement will only be made at low luminosity ($L = 10^{27} \text{ cm}^{-2} \text{ s}^{-1}$), during which ATLAS luminosity monitors are calibrated. Low luminosity allows easier detection of scattered protons at small angles since the beam is spread over a larger transverse area than at higher luminosity. The simulation of the ALFA detector with the proposed beam optics indicates that luminosity can be measured with a precision of 3% [12].

4.4 Relative luminosity monitors

A luminosity monitor is a detector which is used to extrapolate a measurement of absolute luminosity (see Section 4.3) to any other running condition. The response of an ATLAS luminosity monitor must be:

- a) linear over a large dynamic range (from 10^{27} to $10^{34} \text{ cm}^{-2}\text{s}^{-1}$);
- b) fast;
- c) stable in time;
- d) stable under different beam conditions.

The hypothesis of linearity is tested on the basis of Monte Carlo simulations. Algorithms can be applied to the raw detector response to minimize non-linear effects. This topic is discussed in more details in Chapter 8.

A fast detector response (order of nanoseconds) allows for monitoring of individual bunches. The stability of the response is necessary because the extrapolation is done on different time scales.

The list of the ATLAS luminosity monitors with their main features is reported in Table 4.1.

	pseudo-rapidity range	luminosity range ($\text{cm}^{-2}\text{s}^{-1}$)	resolution
LUCID	[5.6, 5.9]	$10^{27} \div 10^{34}$	BX
MBTS	[1.9, 3.8]	$10^{27} \div 10^{33}$	
Tile Calorimeter	[-1.7, 1.7]	$10^{27} \div 10^{34}$	
Liquid Argon	[-5.0, 5.0]	$10^{27} \div 10^{34}$	
BCM	[3.9, 4.1]	$10^{27} \div 10^{34}$	BX

Table 4.1: *Luminosity monitors of the ATLAS experiment.*

4.5 Conclusion

Besides the center-of-mass energy, the performance of a collider is characterized by its luminosity, a quantity directly correlated to the number of interactions which can be provided to physicists for analysis.

Since luminosity only depends on the specifications of the collider, a first evaluation will be made by measuring the LHC parameters, with an expected accuracy of 20 %, reduced to 5 % after some years of experience.

A different method is based on the definition of luminosity as the ratio between the event rate and the cross-section of a given process. For W/Z production from leptonic decays the accuracy is expected to reach 10 %.

A dedicated detector, ALFA, will measure the Coulomb scattering amplitude at a luminosity $L = 10^{27} \text{ cm}^{-2}\text{s}^{-1}$ with a goal accuracy of 3 %.

LUCID is the main luminosity monitor in ATLAS. Other detectors such as BCM, MBTS, Liquid Argon and Tile calorimeters will also perform luminosity monitoring.

Chapter 5

The LUCID detector

LUCID (LUminosity measurement using a Cerenkov Integrating Detector) is the main ATLAS luminosity monitor. It consists of 40 Cerenkov tubes pointing to the primary pp collision region. The Cerenkov gas (C_4F_{10}) is chosen for its radiation-hardness, the pointing geometry allows background suppression. Luminosity calculations, as well as triggering, are performed at the LHC bunch crossing rate (40 MHz) by a reprogrammable device hosting up to four luminosity algorithms.

5.1 Introduction

LUCID is the main luminosity monitor of the ATLAS experiment.

The project was proposed at a later stage of the ATLAS development, when most of the physical space was already taken by other detectors and a tight space in the ATLAS forward region, in the pseudo-rapidity range [5.6, 5.9], was available for the installation of new sub-systems.

The project was approved in February 2007 and the installation of the detector was completed in June 2008.

In Section 5.2 the goals of LUCID are presented. A detailed description of the mechanics and the electronics is given in Sections 5.3-5.6, whereas calibration method and implementation are the argument of Section 5.7.

5.2 Goal of the detector

The primary goal of LUCID is to monitor luminosity in the ATLAS experiment. For a given physics process with cross section σ , the integrated luminosity per bunch crossing is proportional to the average number of interactions per bunch crossing μ :

$$\mathcal{L} = \frac{\mu}{\sigma}. \quad (5.1)$$

Luminosity monitoring means monitoring the average number of interactions μ of a certain physics process. Given a certain luminosity, the larger the cross section, the larger μ .

According to Monte Carlo simulations (PHOJET, PYTHIA [11]), inelastic collisions are the physical processes which are most like to happen in pp collisions at a center-of-mass energy of 14 TeV in the pseudo-rapidity range [5.6, 5.9]. The aim of LUCID is to monitor μ_{inel} by counting the number of primary charged particles produced in inelastic pp collisions.

Together with primary particles (those which are produced at the interaction point), secondary particles are also produced through interaction of primaries with the material between the interaction point and the place where LUCID is located. LUCID design is aimed at detecting charged particles in the ATLAS forward region ($\eta = [5.6, 5.9]$).

Luminosity monitoring is performed both bunch by bunch, and integrated over a luminosity block.

5.3 LUCID project

After a first phase of operation at instantaneous luminosity $L = 10^{33} \text{ cm}^{-2} \text{ s}^{-1}$, the LHC collider will switch to the design luminosity of $L = 10^{34} \text{ cm}^{-2} \text{ s}^{-1}$. The LUCID project consists of two phases (Phase I and Phase II), according to the two phases of LHC operation. The difference in expected dose of radiation requires the choice of different technologies when building the detector. In this thesis, LUCID Phase I design is addressed.

In Phase I, the dose of radiation expected in the region where LUCID is placed is $0.5 \div 0.7 \text{ Mrad/yr}$, with a neutron flux of $5 \times 10^{13} \text{ cm}^{-1} \text{ yr}^{-1}$ [26] (see Figure 5.1). An important requirement for the detector is radiation hardness. Furthermore, it must have fast response to follow the bunch crossing rate of 40 MHz.

A Cerenkov gaseous radiator suits the above constraints since it is radiation hard and Cerenkov light is emitted promptly. Light detection and

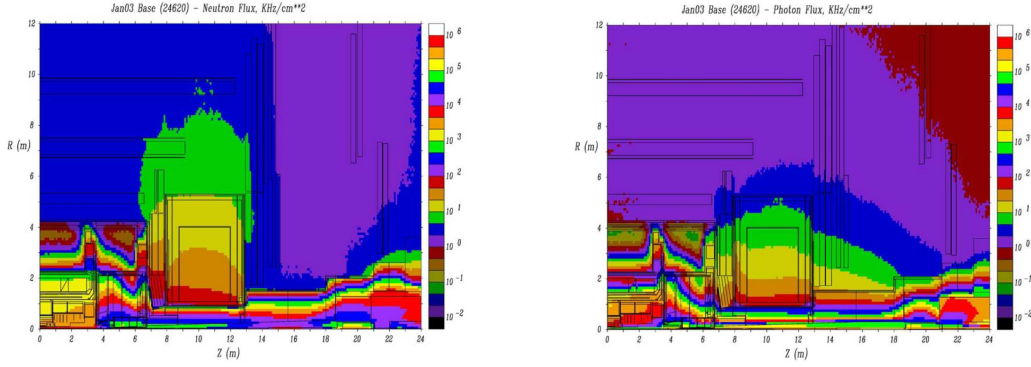


Figure 5.1: Total neutron (left) and photon (right) flux simulations in a full ATLAS quadrant at LHC design luminosity ($10^{34} \text{ cm}^{-2} \text{ s}^{-1}$) [26]. LUCID is placed at $17 \text{ m} < Z < 18.5 \text{ m}$, $|R| < 15 \text{ cm}$.

read-out are performed by means of photomultipliers tubes having a time response of the order of few nanoseconds.

5.4 Principle of detection

LUCID detects charged particles by means of the light emitted in Cerenkov tubes (see Figure 5.2).

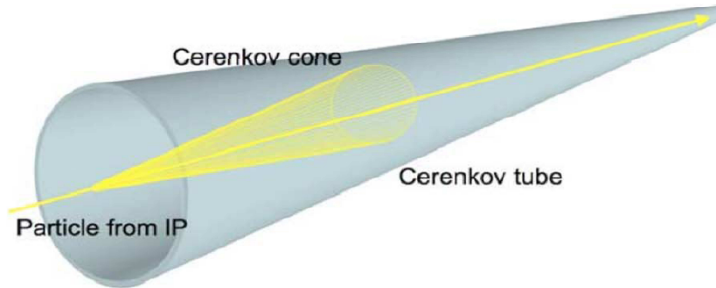


Figure 5.2: Schematic view of a particle entering the tube and emitting Cerenkov light.

Two classes of particles are defined: primary and secondary particles. A primary particle is produced at the interaction point, directly from the primary pp collision or from a prompt decay, and travels along a straight trajectory until it reaches the volume occupied by LUCID. A secondary particle is the product of primary particle interactions with any other material

(detector, machine elements, etc.), and travels along scattered trajectories before reaching the volume occupied by LUCID. Typical primary particles are charged pions and photons from π^0 decays. As far as LUCID is concerned, secondary particles are mainly photons and electrons (see section 7.4.1 for more details) produced in interactions of primaries with the material of the beam pipe.

Background suppression is achieved by means of tight aluminium tubes, arranged so as to exploit the kinematic features of particles emerging from the interaction point (IP). Since tubes are pointing at the interaction point, a primary particle typically enters a tube from the front and travels inside the tube along a path parallel to the axis. A secondary particle is expected to enter from the lateral wall of the tube and travel a shorter path inside the tube (see Figure 5.3).

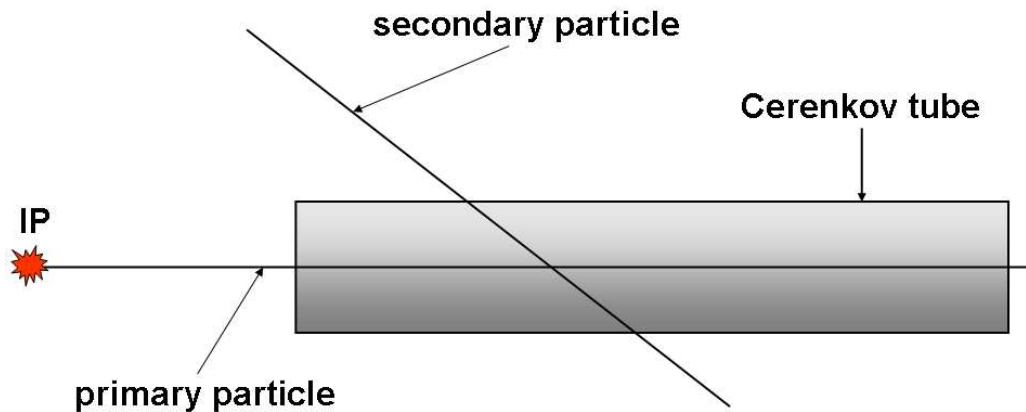


Figure 5.3: A LUCID Cerenkov tube (not in scale). Comparison between the path travelled by a primary and a secondary particle.

Since light is emitted continuously over the tube length, a primary particle is expected to release a larger amount of Cerenkov light than a secondary particle. Proper threshold cuts on the light detected by photomultipliers are expected to reduce the contribution due to secondary particles.

Validity of the pointing geometry

During several On-Beam test of LUCID prototypes, angular scans have been carried out in order to verify the validity of the pointing geometry concept. In Figure 5.4 the number of photoelectrons registered from a 180 GeV pion

entering a tube is plotted as a function of the angle between the tube axis and the particle direction.

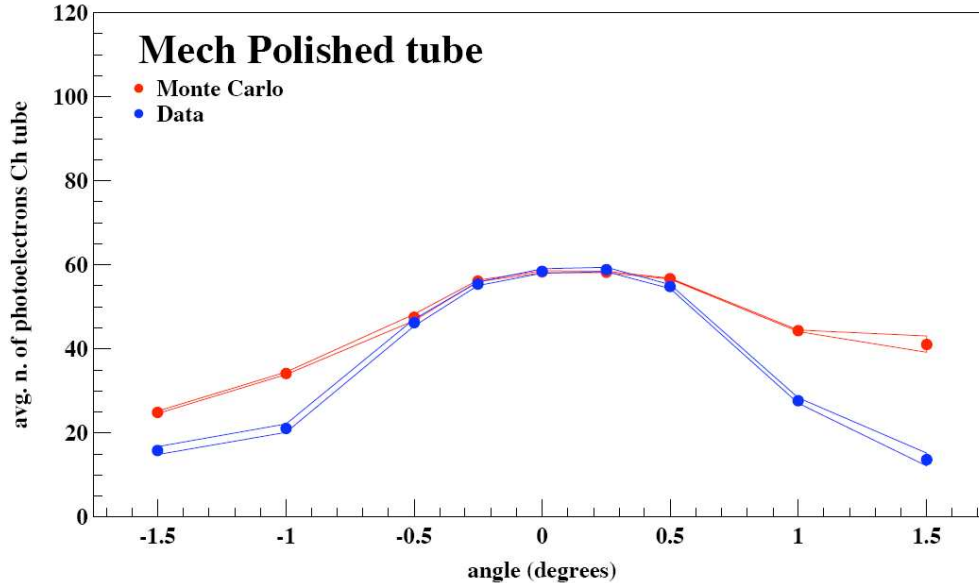


Figure 5.4: Angular scan for a mechanically polished prototype tube, read out by a PMT. The average number of photoelectrons is shown both for real data and Monte Carlo simulations. [27].

The plot shows the average number of photoelectrons emitted by a charged particle as a function of the angle between the particle trajectory and the tube axis. For angles larger than 0.6° there is a drop in the photoelectron number of 25 % [27]. The discrepancy between data and simulation at large angles is due to an inaccurate description of the beam and tube optical properties.

5.5 Phase I design

LUCID consists of two modules (vessels) placed in the ATLAS forward region at a distance of ~ 16.7 m from the interaction point. Vessels are ~ 1.5 m long and closely arranged around the beam pipe. They have an inner radius of ~ 8.5 cm and outer radii of ~ 12.5 cm at the side facing to the interaction point and ~ 14.7 cm at the opposite side to allow a projective geometry. Each vessel contains 20 aluminium tubes 1.495 m long, with an inner radius of 7

mm and a thickness of 1 mm. A LUCID module is shown in Figure 5.5.



Figure 5.5: *Cutaway view of single LUCID module. Cerenkov tubes surround the beam pipe and are read-out by PMTs (yellow) or fibers (red).*

Cerenkov light is emitted inside the gas at an average angle $\sim 3^\circ$ with respect to the particle trajectory, and converges at the end of the tube by means of multiple reflections on the inner tube surface. The inner tube surface is mechanically polished so as to increase its reflective power.

Sixteen tubes are arranged in two rings of eight tubes and constitute the relevant part of the Phase I design. To point at the interaction region, the angle with the beam axis of the two rings are $\theta_{ring1} = 0.33^\circ$ and $\theta_{ring2} = 0.39^\circ$. Taking into account the size of the tube radius, the angular coverage corresponds to a pseudorapidity range between $5.61 \leq \eta \leq 5.92$. Light is converted into electrical signals by a photomultiplier (PMT) placed at the tube end (Hamamatsu R762). The PMT diameter matches exactly the transversal dimension of the tube (14 mm diameter). The quartz window in front of the PMT has a thickness of 1.2 mm and is chosen for its transparency to the Cerenkov radiation down to 160 nm.

Four tubes are placed in between the two rings and are readout with Multianode PhotoMultiplierTube (MaPMT) via optical fiber bundles. This type of read-out is a test for a Phase II design when direct coupling of photomultipliers to Cerenkov tubes cannot be used due to increase in radiation doses (ten times Phase I values [26]).

An LED calibration system is provided for each tube with a fibre-optic distribution of the light.

Vessels are filled with C_4F_{10} gas at 1.1 bar. Such Cerenkov radiator is chosen because it is radiation hard, non flammable and has a good transparency for photons in the UV region where most of the Cerenkov light is emitted (see section 7.2). The overpressure is necessary in order to prevent air to filter inside the Cerenkov tubes, which would reduce their reflectivity features due to oxydation of the aluminium surface.

5.6 Electronics

The signal provided by LUCID for analysis is the result of a series of steps.

Cerenkov photons hitting a PMT are converted into a current. The current is then integrated over time, yielding a charge. Detected photons are

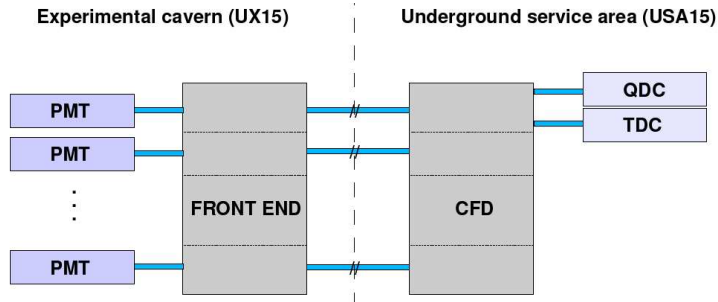


Figure 5.6: *Schematic view of LUCID electronics setup.*

called photoelectrons. The analog signal from each photomultiplier is sent to a Front End (FE) board placed 10 meters away from the detector (see Figure 5.6). The signal is amplified and sent over a 100 m long cable to the electronics rack in the Underground Service Area (USA15), where it is fed to four 8-channel discriminator units (CFD, Constant Fraction Discriminator).

Each CFD sends the signals to a Charge to Digital Converter (QDC) for amplitude measurements and to a Time to Digital Converter (TDC) for time-of-arrival measurements. This hardware sampling constitutes a local dataflow, with a trigger independent of ATLAS trigger, aimed at checking detector operation and data quality (charge distribution, time of arrival with respect to the bunch crossing).

If the signal coming from one of the tubes is above the corresponding CFD threshold, the related CFD trigger and logical output are set and internal scalers are incremented. The logical OR of all CFD triggers opens the gate to the QDC and starts a trigger window in the TDC. As a consequence, both the signal amplitudes and arrival times are sampled. They build up the local Lucid event, which is stored on disk for analysis. Nothing is sent to the ATLAS Data Flow, although two kinds of trigger signals can be sent to the Local Trigger Processor (LTP).

Luminosity algorithms

Luminosity calculations and trigger signals are handed over by the LUMAT (LUMinosity Algorithm and Trigger) card. The LUMAT card processes logical signals, namely the tube hits (signals over threshold), and is synchronized with the ATLAS clock. Four algorithms for luminosity calculation are foreseen.

For each algorithm, luminosity is integrated over a luminosity block (time over which luminosity variation is negligible). The length of a luminosity block is currently set to 1 minute [16]. The LUMAT card provides luminosity values for each one of the 3564 bunches, and a value which is the sum of the luminosity value of all bunches. The latter is also calculated over a locally defined luminosity block.

All algorithms and methods are implemented so as to take into account busy conditions (when an event is triggered and subsequently no other event is processed until the gate is open) and dead-times (e.g. every 5 seconds a “reset” signal is sent over the whole detector and data-taking is suspended for 1 ms before and after that signal).

All algorithms are foreseen for two detector operation modes: single side (when an interaction is detected if at least one module registers a hit) and coincidence mode (when an interaction is detected only if both modules register a hit). The LUMAT card is re-programmable, thus algorithms can be tuned even at later stages. A study of the algorithms implemented in the LUMAT is reported in Chapter 8.

5.7 Calibration

The electric charge collected by each photomultiplier tube is converted in a digital value by the QDC. Calibration is needed in order to evaluate how many QDC channels correspond to a single photoelectron.

The calibration is performed by using the single photoelectron method [28]; the basic idea is to measure the number of QDC channels due to a single photon convoluting the photomultiplier spectrum as a sum of $n = 1, 2, 3, \dots$ photoelectrons contributions. In the low statistics case, when the expected number of photoelectrons is $\mu < 5$, the spectrum shows a typical distribution from which it is possible to evaluate the number of QDC channels due to a single photoelectron through a fitting procedure.

In Figure 5.7 a typical spectrum of a calibration run with an installed tube is shown, with a special emphasis on the different photoelectron contributions to the total spectrum. The first peak is the pedestal, independent of the

light collected at the photocathode and mainly due to dark current (random generation of electrons and holes within the depletion region of the device), and thermoionic emission, and is expected to show a Poissonian behaviour.

The second peak is the single photoelectron contribution, whereas the other peaks represent the contributions of the subsequent photoelectrons. The number of QDC channels associated to a single photoelectron is obtained by subtracting the pedestal (Q_0 in the plot) from the single photoelectron positions (given by the parameter Q_1). The pedestal is not purely Poisso-

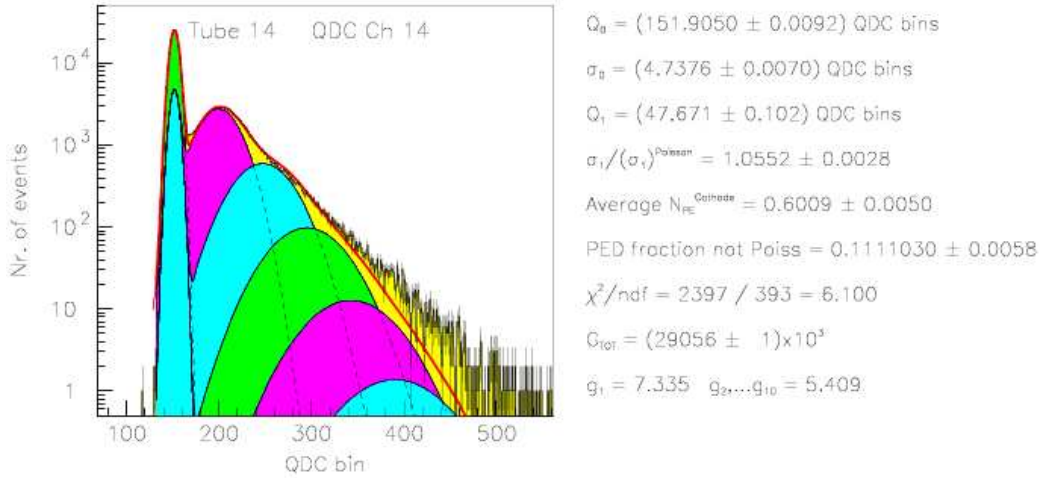


Figure 5.7: *Photoelectron spectrum. Pedestal and single photoelectron peaks are visible.*

nian as expected, but accounts for the electronic noise: the non-Poissonian contribution is represented by the blue peak inside the pedestal peak.

After calibration, the gain of the electronics chain is adjusted so as to exploit the whole dynamic range of the QDC while avoiding saturation.

5.8 Conclusion

LUCID is a Cerenkov detector aiming at monitoring luminosity for the ATLAS experiment.

It is located at about 17 m from the interaction point and covers the pseudo-rapidity range of $\eta = [5.6, 6.0]$. It is made of 40 Cerenkov tubes read-out by photomultipliers and pointing to the pp collision region. It is designed to be resistant to the high radiation doses present in the site and to provide measurements and trigger bunch by bunch.

On-Beam tests confirm the projective geometry of LUCID showing that charged particles travelling along directions more than 0.6° away from the tube axis causes losses of 25% of the signal.

An electronic card (LUMAT) calculates luminosity and provides a trigger based on the signals registered in LUCID. It is able to run up to four algorithms and is reprogrammable, thus featuring redundancy and flexibility. The LUMAT card provides bunch by bunch luminosity at the event rate of ATLAS of 40 MHz.

Chapter 6

The LUCID Detector Control System

The LUCID Detector Control System (DCS) continuously monitors all relevant detector parameters, like high voltage channels and vessels pressure. Archiving and alert handling for all relevant data are implemented for bug tracking and offline analysis. LUCID DCS has been successfully tested during LHC first beam event in September 2008.

6.1 Introduction

The presence of an overall Detector Control System (DCS) became necessary with the complexity of the LEP experiments in the late 1980s. Controls became no longer stand-alone systems, but part of the experiment which ties physics and technology. In this new approach, a system was splitted into subsystems put at different layers, so as to form a coherent framework offering high levels of scalability and modularity.

Within this scheme, the ATLAS experiment is seen as a complex system composed by sub-components (detectors, infrastructures) in a chain which ends up in the real devices (magnets, photomultipliers, temperature probes). Commands propagate from the top to the bottom of the hierarchy (like the start a physics run), and statuses propagate from the devices to the top (like the dataflow, or alarms for critical conditions) according to well established rules defined in the Finite State Machine.

In Section 6.2 the main features of the ATLAS DCS are discussed. The DCS tools developed for LUCID are described in Section 6.4, whereas the implementation of Finite State Machine is described in Section 6.3.

6.2 Detector Control System

The DCS ensures the coherent and safe operation of a given device and serves as a homogeneous interface to all sub-detectors and to the technical infrastructure of the experiment. DCS continuously monitors all operational parameters, signals any abnormal behaviour to the operator, allows automatic or manual corrective actions to be taken.

Concerning the hardware of the detector, all actions initiated by the operator and all errors, warnings and alarms are handled by DCS. The interaction of technical experts with their sub-detector is managed through DCS, in order to verify internally that the operations requested are safe for a given device. Besides that, DCS must enable a homogeneous way of communication with the Data Acquisition system (DAQ) and the external systems, like CERN services and the LHC collider.

DAQ and DCS act like the glue of the experiment, making all the different integrating systems to work coherently like a whole. DAQ and DCS are complementary. The former treats all aspects of the physics event-data, which are identified by an event number. The latter deals with all other types of data, normally categorized with a time stamp, which are needed for understanding detectors behaviour for physics analysis.

6.2.1 The ATLAS DCS

The ATLAS Detector Control System [29] provides complete control over all sub-detectors, all infrastructure and services, and all interactions with the LHC machine. All operator actions on the detector, as well as presentation of all error messages, warnings and alarms to the operator will be carried out by means of the DCS.

DCS performs the following tasks:

- i - parameter monitoring, loading, logging and setting;
- ii - on line status display;
- iii - issuing of commands for certain actions;
- iv - correlating parameters from different parts of the detector;
- v - collaborating with the DAQ system via the Run Control layer;
- vi - control calibration and alignment processes;
- vii - supervising the safety of the detector in collaboration with the Detector Safety System (DSS);

viii - triggering alarms, emergency procedures, etc.;

ix - handling of error messages.

The essential features of ATLAS DCS are reliability, robustness, scalability and modularity since its configuration will undergo modifications and extensions throughout the lifetime of the experiment. Due to the decomposition of the ATLAS experiment into subsystems, the DCS also follow this partitioning into independent control and monitoring applications in charge of single sub-detectors or subsystems. Each of these sub-detector control applications also uses common hardware and software components such as a global database, an error reporting and logging system, and software to control and monitor actions on the different devices.

The system must be flexible and accommodate new functions corresponding to operations of new types of devices. Modularity and standardization of components satisfy the individual requirements for each sub-detector, while assuring the coherency and homogeneity of the system.

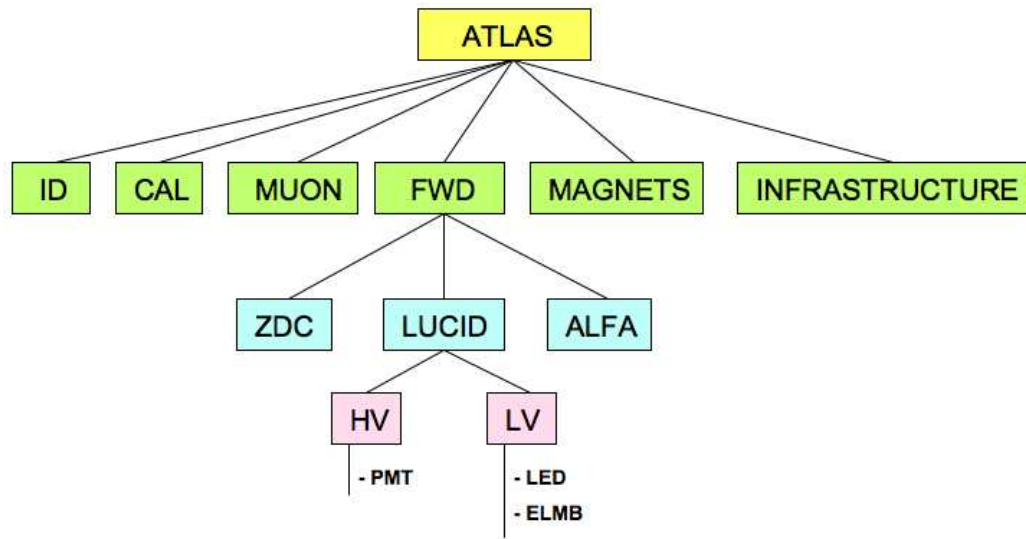
Organization

The DCS of the ATLAS experiment is implemented using a hierarchical structure of the participating systems to obtain a fully integrated and coherent detector operation. From the point of view of controls, the detector is composed of largely independent units, organized in a tree-like structure of many levels as shown in Figure 6.1. This is composed by system layers and clear interfaces between them.

The first layer of this structure is composed by the inner detector, the calorimetric system, the muon spectrometer and the forward detectors, together with the control of the magnets and the common infrastructure of the experiment like electronics crates, racks and cooling. On the next layer, the sub-systems include the relevant sub-detectors: Forward detectors (FWD) groups LUCID, ZDC and ALFA, and so on for the other sub-systems. Each sub-detector is sub-divided in further units, depending on functional or topological reasons. Functional reasons can be for example by the cooling system, the high and low voltage power supplies, the gas systems etc. A topological grouping is foreseen for devices placed in a certain region of the ATLAS cavern: end cap A or C, barrel.

Structure of the DCS

For each sub-system, the ATLAS DCS consists of a distributed Supervisory Control And Data Acquisition system (SCADA) running on PCs and called



2

Figure 6.1: *Hierarchical organization of the ATLAS DCS.*

Back-End (BE), and of the Front-End (FE) systems (see Figure 6.2). The SCADA system, based on PVSS II 3.8, acquires data from the front-end equipment and offers supervisory control functions, such as data processing, presenting, storing, archiving and alert handling. An Oracle database contains records of all equipment where the data values are stored.

DCS architecture is divided into three logical layers: process, control and supervisory layers. The SCADA component is distributed on the two last layers while the front-end equipment is in the process layer. This layered structure follows the geographical distribution of the equipment in three different areas as shown in Figure 6.2.

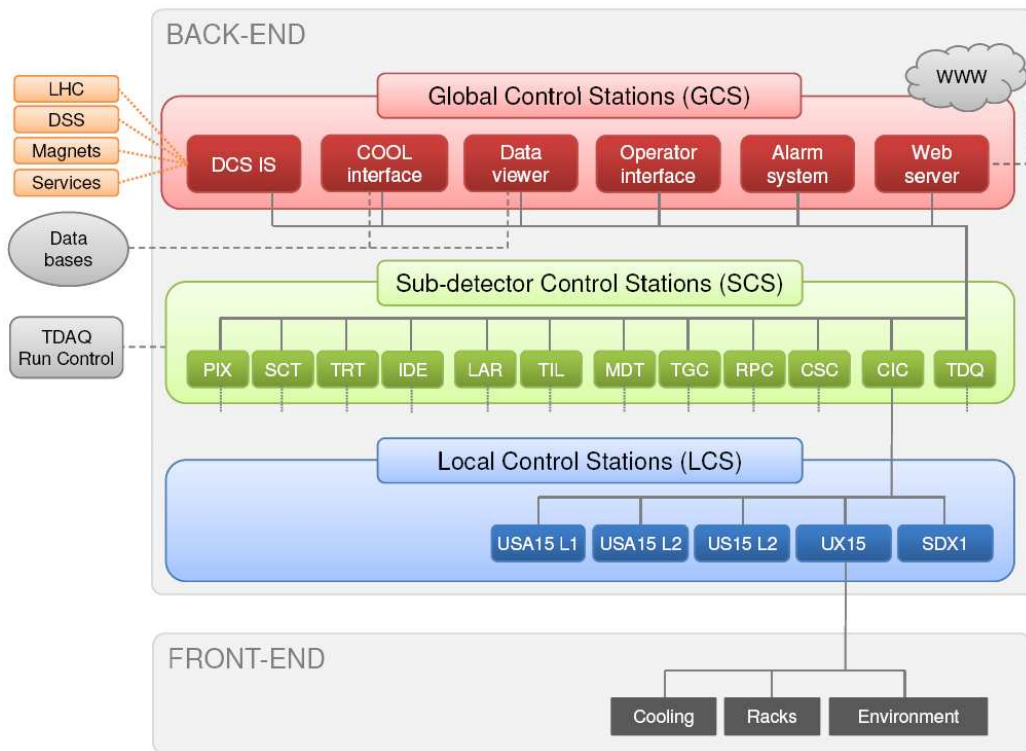


Figure 6.2: *ATLAS DCS architecture.*

Process Layer The Front-End (FE) electronics in the experimental cavern (UX15) is exposed to radiation and to strong magnetic fields. The instrumentation in the cavern must be radiation-hard or tolerant to levels of $1 \div 10^5$ Gy per year in the muon sub-detector and inner tracker, respectively. In addition, depending on the location, a magnetic field of up to 1.5 T has to

be tolerated. The DCS equipment at this level consists of controllers, which connect to the hardware, either as separate modules or as microprocessors incorporated in the front-end electronics. This equipment is distributed over the whole volume of the detector with cable distances up to 200 *m*. The distribution underground is organized by fulfilling two competing constraints. On one hand, because of the radiation level, the magnetic field and the inaccessibility at UX15 during beam time, the equipment should be located in USA15. On the other hand, complexity, cost and technical difficulties suggest condensing the devices in UX15 and transferring only the results to USA15.

The control layer The process equipment is interfaced to multipurpose front-end computers. The equipment of this layer is installed in the underground electronics room USA15 and consists of:

- workstations, allowing supervision of individual partitions, mainly during commissioning and maintenance periods;
- dedicated stations, running real-time operating systems, usually distributed around the installation, which control the equipment. These systems are called Local Control Stations (LCS) in figure Figure 6.2. They run the SCADA software collecting data from the front-end devices in their partition. The LCS allows to run a partition either independently in standalone mode or integrated as part of the whole detector.

Supervisory layer The equipment of this layer is installed in the main control room in building SCX1. The equipment consists of general-purpose workstations which are linked to the control layer through a LAN providing TCP/IP communication. These workstations retrieve information from the Local Control Stations of the different partitions and can be used to interact with them by means of commands or messages. This system provides a limited set of macroscopic actions to generate the sequence of operations necessary to bring the experiment to a giving working mode. In addition, this system monitors the operation of all sub-systems, generates alarms and provides the interlock logic where necessary. Information for these sub-systems will be used to build the overall status of the experiment. This layer is also responsible for the dynamic splitting of the experiment into independent partitions and the possibility of concurrent data taking from the partitions. Nevertheless, the direct access to each sub-system in order to gain detailed

information and control will always be possible. This layer represents the interface to DAQ and safety system.

Sub-detector organization

All sub-detectors in ATLAS will have their own local DCS with a minimum of one Local Control Station per sub-detector. Each local DCS controls and monitors the operation of a sub-detector and related equipment.

Although each sub-detector is responsible for the implementation and for the internal organization of the subsystems, they must fulfill the requirements defined in the ATLAS DCS User Requirements Document [30]. The central DCS team defines the standards to be followed and provides the tools needed for their implementation; the general DCS also aims at providing common solutions for histogramming, trending, error reporting and alarm handling. This will make it easier to maintain the system by any DCS expert.

The overall system has connections to centrally provided services: the Global DCS, the Central Safety System (CSS), the DAQ system and the LHC machine control system.

6.3 Finite State Machine

The Finite State Machine allows:

- 1) integration between DCS and TDAQ;
- 2) management of the experiment as a whole.

Finite State Machine (FSM) is based on the concept of *objects* that are in a definite *state* and to which one can send at any moment an *action request* that is meant to bring it into another state.

As an example, when the run leader decides to start a physics run, a command is issued to all the subdetectors, and checks on their status are performed. The run leader does not have to tune his commands to each specific sub-detector at the lower levels: each subsystem must handle the “start run” command in the appropriate way. On the opposite direction, if the state of a device changes, it propagates to the higher levels which take the appropriate decisions according to well established rules. Two types of objects can be defined:

Abstract objects: they may send or receive action requests to/from other objects and their state is determined usually as a result of the change of states of other objects.

Associated objects or **Device unit nodes**: they represent real devices of the system. Their behaviour in response to actions consists in a real interaction with hardware.

The ATLAS implementation of FSM [31] is composed at the higher levels by abstract objects which represent the set up of the detector from a logical point of view such as sub-detector arrangement, specific device grouping (high and low voltage power supplies) and common services grouping (infrastructure). Real devices (high and low voltage channels, temperature probes, communication devices etc.) are represented only at the lowest level and are the associated objects.

All these objects are connected to form a tree, the highest levels representing the abstract objects whereas the lowest level consists only of the associated objects (also referred to as device units).

6.4 DCS implementation for LUCID

6.4.1 LUCID Local Control Station

LUCID DCS is fully integrated in the central ATLAS DCS. LUCID Local Control Station hosts the necessary tools for communication with the hardware devices:

- i - high and low voltage power supplies;
- ii - temperature and pressure probes.

The Local Control Station also runs the DCS SCADA software. All the software tools like codes, panels and scripts have been developed by means of the tools offered by the SCADA software and were ready for the commissioning of the detector.

6.4.2 High and low voltage control and monitoring

High voltage channels supply the photomultiplier tubes. Monitoring the high voltage is fundamental for two reasons: to avoid PMT damage due to voltage values higher than the maximum allowed (1350 V for Hamamatsu R762); and to get reliable data, since the response of a PMT depends on the voltage applied. Low voltage channels supply back-end electronics such as LED board, signal amplifiers, embedded micro-processors (ELMB¹). High and low voltage channels are operated through dedicated panels (see Figure 6.3). The operator is allowed to set several parameters for each channel. Critical settings are applied only if they pass a safety check. In case of failure (over-voltage, overcurrent etc.), a channel is automatically powered down and an alert is set.

The stability of the high voltage channels is also checked by means of a dedicated script. As soon as the channel has reached its setting value, the script calculates the difference between the setting value and the actual value. This information is sent to the TDAQ system which takes the decision if the channel (PMT) is valid or not for data-taking.

Figure 6.4 shows a stability plot for a high voltage power supply over a time period of seven hours. As one can see, both the voltage and the current are very stable.

¹The Embedded Local Monitor Board is a plug-on board to be used in LHC detectors for a range of different front-end control and monitoring tasks. It is based on the CAN serial bus system and is radiation tolerant and can be used in magnetic fields [32].

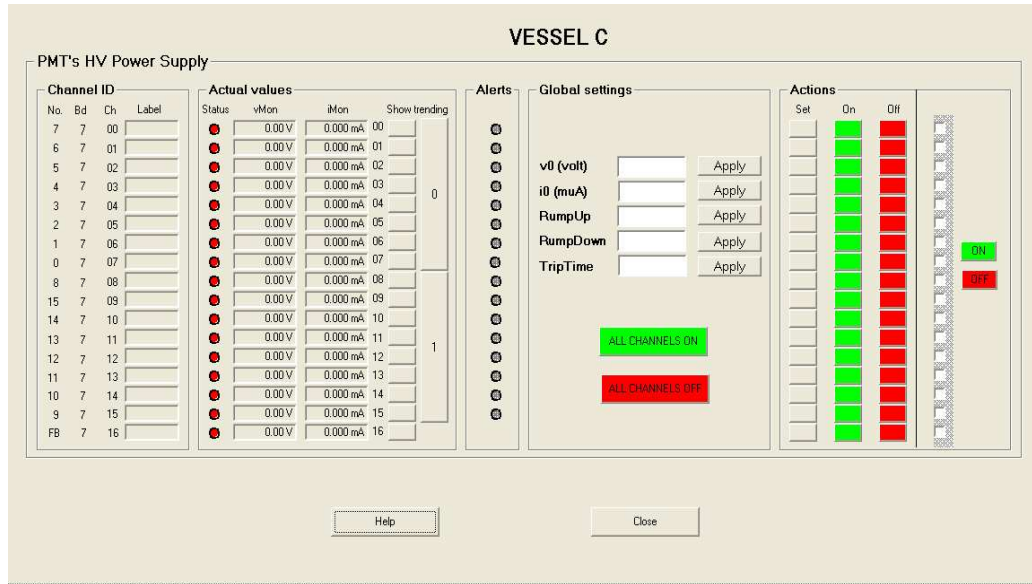


Figure 6.3: DCS panel for high voltage channels. A similar panel has been developed for low voltage channels.

The voltage accuracy is 0.05%, which means 0.5 V at 1000 V. Due to a limitation of the data flow to the archives, values are stored only for changes larger than 1% (10 V at 1000 V). For this reason, the statistical fluctuations of the measurements provided by the probes are not visible.

6.4.3 Pressure monitoring

The light yield of a charged particle crossing LUCID depends on the pressure of the Cerenkov gas radiator (see Eqs. 7.4-7.5). The chosen working pressure is 1.1 bar. Beam tests have shown that a pressure variation of 1% produce a light yield variation of 0.2%. Since both vessels are not perfectly pressure tight (20 mbar/day leakage), in order to keep the working pressure constant, a system to refill the vessels is installed.

Since exposure of aluminium tube walls to air may cause loss in reflectivity, vessels are filled with an inert gas (Argon) at a pressure larger than the external one, so as to prevent air entering into the vessel. A pump automatically feeds the gas into the vessels in order to keep a minimum overpressure of 50 mbar with respect to the ambient pressure in the experimental cavern. In these conditions, the system shows a stability of 1% against a variation of ambient pressure of 3% (see Figure 6.5).

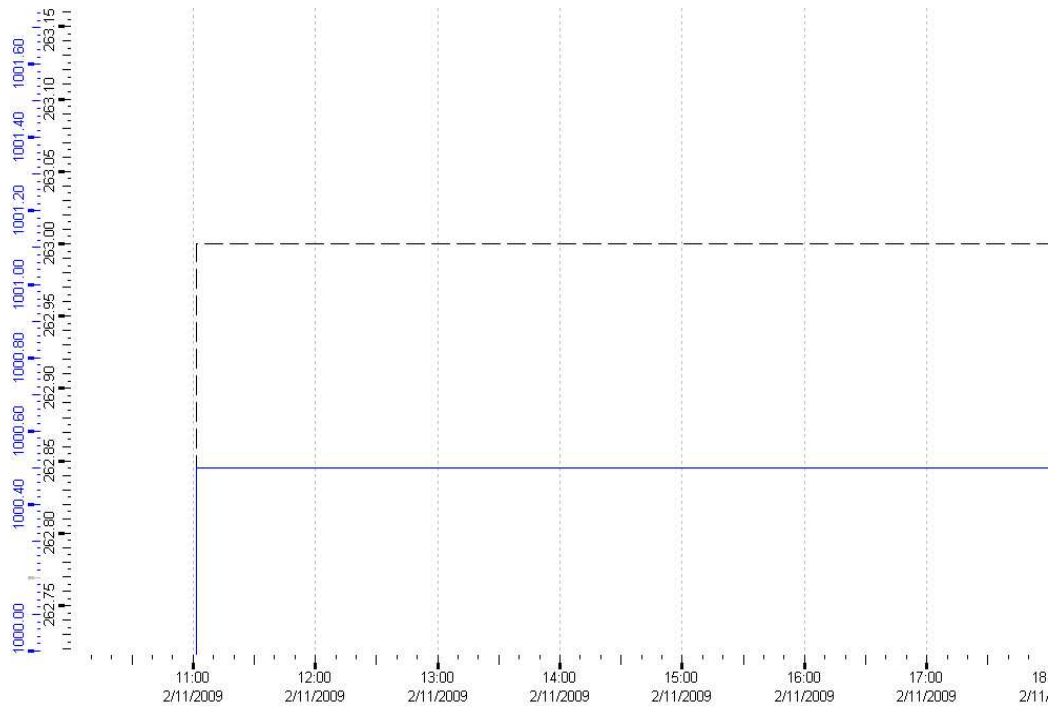


Figure 6.4: *Stability of high voltage power supply. Voltage (solid line) and current (dashed line) of a high voltage channel over a 7 hours time range.*

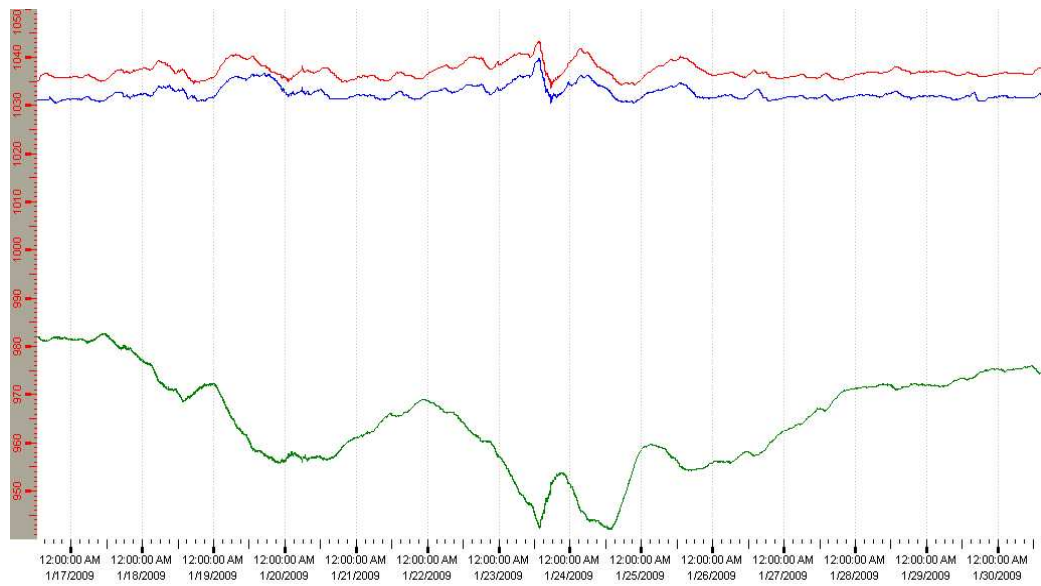


Figure 6.5: *DCS panel for pressure monitoring. Environment pressure is plotted in green, whereas the red and the blue lines represent the pressure of the gas in vessel A and C respectively. Systematic difference in pressure value between the two vessels is due to different gauges.*

In order to keep these conditions stable, a script has been developed to calculate the difference between the pressure of the gas contained into the vessels and the ambient pressure. If the pressure difference drops close to the atmospheric pressure, alerts are set.

6.4.4 Temperature monitoring

The variation of light yield due to the temperature is negligible and will not be taken into account in offline analysis.

Monitoring the temperature is instead crucial for the PMTs. During beam pipe bake out (see Section 3.2.5 for more details), temperatures as high as 220° Celsius can be reached in the region where LUCID is located. Electronic devices, as well as mechanical parts, do not resist to temperatures larger than 50° Celsius.

In order to prevent the vessels from overheating, a cooling system has been installed. A copper pipe of diameter 6 mm is placed between the beam pipe and the inner wall of the vessels are shown in Figure 6.6. Cool water

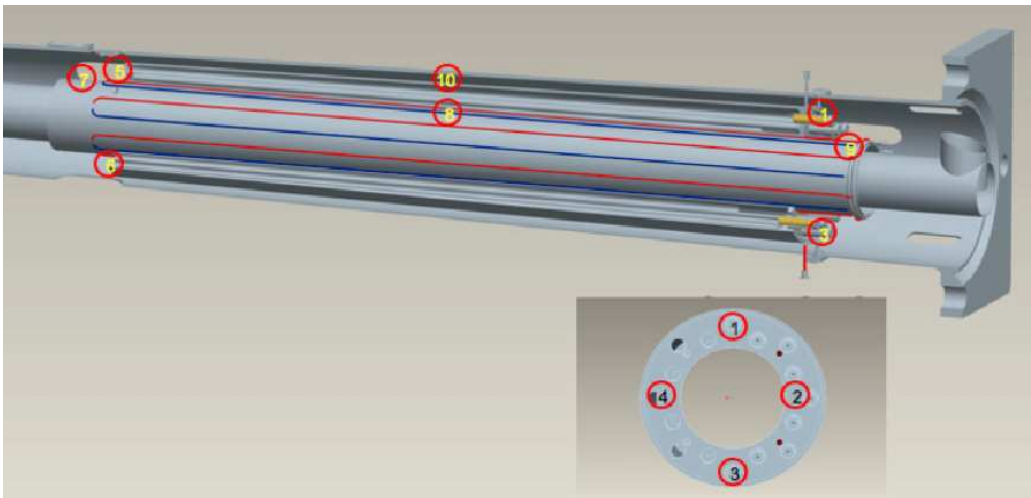


Figure 6.6: *Position of the temperature probes (numbers circled in red) and of the copper pipe (red and blue solid lines).*

is continuously fluxed into the pipe at a temperature between 15° and 18° Celsius. The refrigeration compressors start operation when the temperature reaches 18° Celsius and keep running until the water temperature goes below 15° Celsius.

In order to monitor the temperature, each vessel is equipped with 10 temperature probes. Their position is reported in Figure 6.6.

A control script checks the values of all temperature probes. If at least two temperature probes on the same side exceed the value 38° Celsius, a warning is raised. An interlock system is set such that, whenever at least two temperature probes on the same side exceed 45° Celsius, the bake-out circuit is automatically interrupted.

A comparison of the temperature of the beam pipe and of the side A vessel during the bake-out procedure is shown in Figure 6.7. In the LUCID

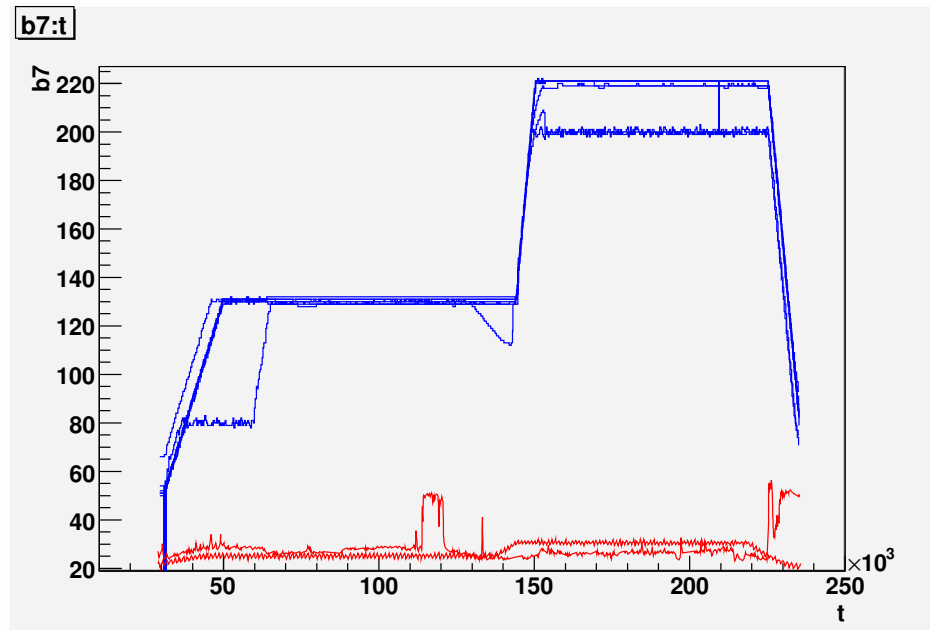


Figure 6.7: *Temperatures of the beam pipe (blue) and of the vessel (red) on side A during the bake-out.*

region, the maximum temperature reached by the beam pipe was 220° C, whereas the vessel temperature reached a maximum of 56° C with one of the probes for a very short period, being the other probes at temperatures below 30° C.

The same plot for the side C vessel is shown in Figure 6.8.

The maximum temperatures measured during the bake-out procedure are also summarized in table 6.1. As one can see, the LUCID cooling system kept the temperatures well below the critical value.

A maximum temperature of 56° C was detected by probe 8 on side A, far

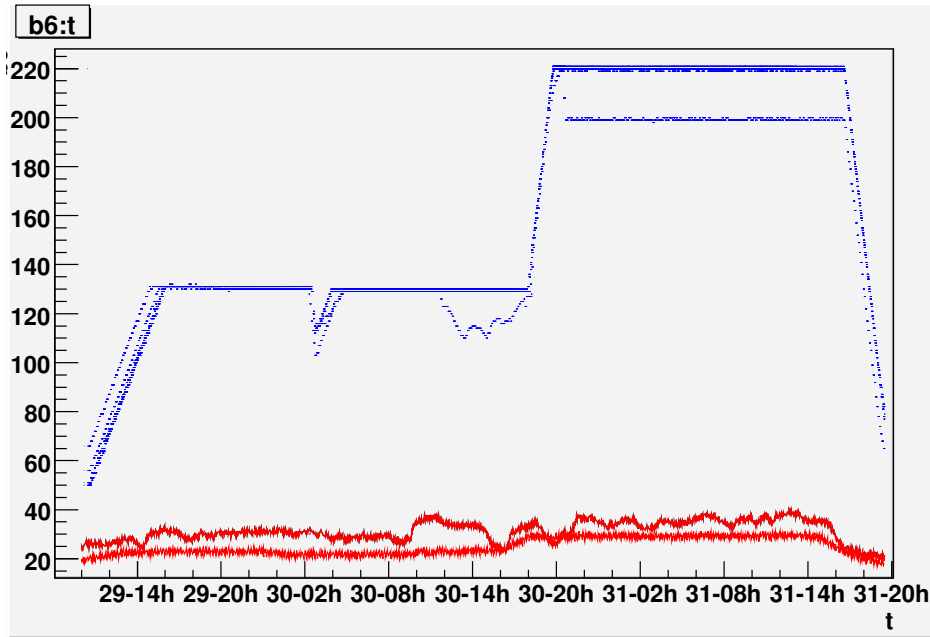


Figure 6.8: *Temperatures of the beam pipe (blue) and of the vessel (red) on side C during the bake-out.*

	<i>probe number</i>									
	1	2	3	4	5	6	7	8	9	10
<i>Vessel A</i>	27.5	27.5	25.6	26.5	27.8	27.6	32.1	56.3	22.6	27.8
<i>Vessel C</i>	39.6	n.d.	37.7	38.4	30.5	33.8	31.1	n.d.	22.0	33.8

Table 6.1: *Peak temperatures detected on the LUCID vessels during bake-out procedure (° Celsius).*

from the PMTs, whereas the other probes were below 40° C. Temperatures on side C are on average larger than those on side A due to different conditions in air circulation around the vessels, but always below 40° C.

6.4.5 DCS/TDAQ Communication

Data-taking may occur only if certain conditions are fulfilled. For example, a physics run may start only if at least one PMT on each side and the corresponding readout electronics are on. A dedicated script defines the readiness of the system according to the above mentioned criteria and publishes a flag (`Not_Ready_for_DAQ`).

LUCID DCS also subscribes and archives from the TDAQ information on calibration and thresholds according to the type of run (calibration or physics) and for offline analysis.

6.5 FSM implementation for LUCID

The structure of the LUCID FSM tree is sketched in Figure 6.9. The abstract objects are represented by green bubbles, whereas the device unit nodes are represented by orange rectangles.

The ATLAS node represents the top node. The sub-systems are grouped on the second layer: inner detector, calorimetric system, muon spectrometer, forward detectors (FWD), magnets and common infrastructure. Each sub-system groups the sub-detectors. LUCID is in turn sub-divided in three logical nodes: two for each vessel (A and C) and the infrastructure. The sub-structure of each vessel is identical, so only one is reported in figure. For each vessel, high voltage supplies PMTs. Low voltage supplies amplification of PMTs signals (TX), LED card for calibration, ELMB card (MONITOR) to allow reading temperature and pressure probes. The infrastructure comprises control over power supplies status, hardware drivers status, archiving and communication tools like connection with Oracle archive, status of communication tools (CAN bus).

LUCID node is hierarchically connected to the top node ATLAS through the FWD node, which groups the forward detectors.

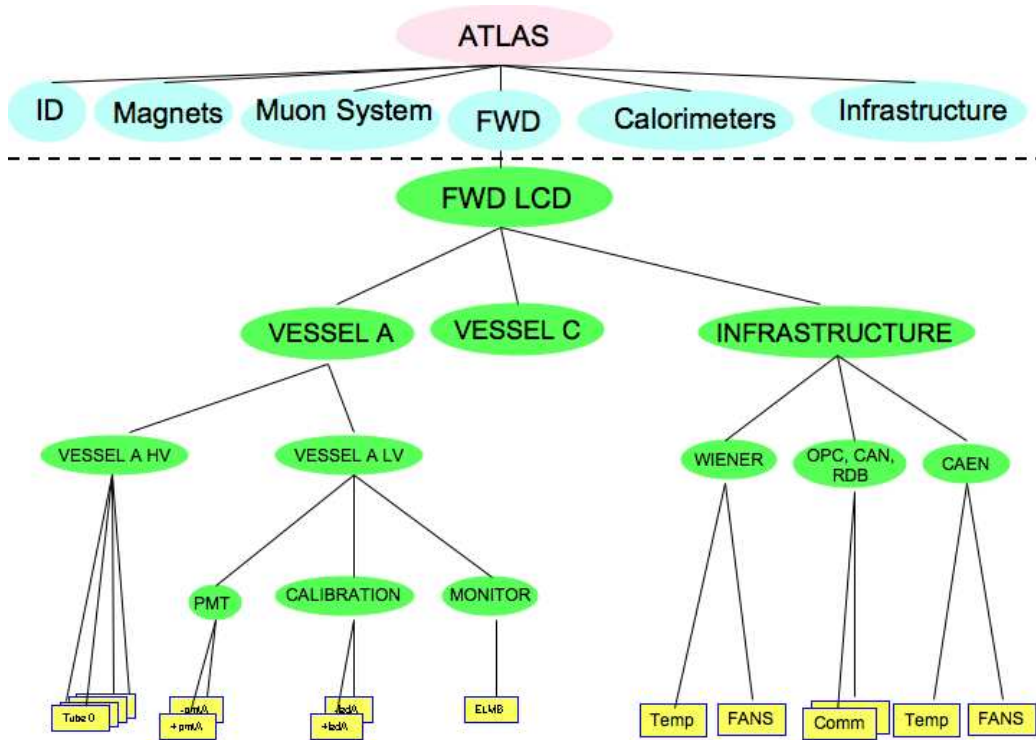


Figure 6.9: *LUCID FSM tree.*

6.5.1 FSM panels

ATLAS FSM allows monitoring the state of the detector and issuing commands, by means of panels. The main FSM panel of LUCID is shown in Figure 6.10.



Figure 6.10: *LUCID FSM main panel.*

The buttons on the top left (red bubble) allow to navigate through the other nodes of the tree by simply clicking on the node's name. Commands to set-up the detector for different tasks (calibration or physics) can be issued by clicking on the green buttons (yellow bubble).

A schematic overview of the detector is depicted in the central part of the panel (grey area). The top side of the drawing is divided into two sides, one for each module of the detector. In the upper part, labelled HIGH VOLTAGE, a prospective view of the vessel is given. The photomultipliers are represented through coloured circles. The colour indicates the status of the PMT: green means that the PMT is powered on, blue that it is powered

off. More colours are foreseen: yellow during the powering on and off period (it may take several seconds) and grey if the channel is tripped. In the section labelled LOW VOLTAGE, the low voltage channels are shown in a similar way by coloured circles. Temperature and pressure of the vessels are displayed in the corresponding textfields. In the section labelled INFRASTRUCTURE the statuses of the infrastructure devices are displayed. The meaning of the colours is the same as before. In the lowest part of the panel a plot shows the hit rates registered by the detector in real time. Alarms are displayed in the box on the right upper part of the panel.

Panels have been developed according to the objects or device type of each node. For each object appropriate rules for command issuing have been established.

6.5.2 First Beam events

All LUCID DCS functionalities have been tested inside the general ATLAS run control in sub-detector combined runs, simulating real data-taking.

The performance of LUCID DCS in a realistic environment has been tested on September 10th 2008, when the first attempt to inject protons in the LHC accelerator at an energy of 450 GeV was made.

Two separate beams (Beam 1 and Beam 2) were scattered by collimators at 140 m from the central position of ATLAS, producing so called “splash events”. Particles produced by proton scattering within collimators are not correlated with the ATLAS interaction point (IP). The signal generated by such particles in LUCID is smaller than that given by a particle coming from the IP for which the detector response is optimized. For this reason, a threshold smaller than the optimal one planned for *physics* runs was used to define a hit.

The response of LUCID to the particles traversing the detector is shown in Figure 6.11 (orange bubbles), along with other detectors.

In the left plot, the hit rates registered by the Forward Detectors during Beam 1 injection (from side A to side C) versus time are shown. LUCID hit rates are indicated by the orange circles. From top to bottom, the first two plots refer to L1Calo whereas the yellow and brown refer to MBTS. In the right plot, the hit rates registered during Beam 2 injection (from side C to side A), are shown.

The time offset between LUCID and MBTS (40 s) is due to a lack of synchronization between the systems.

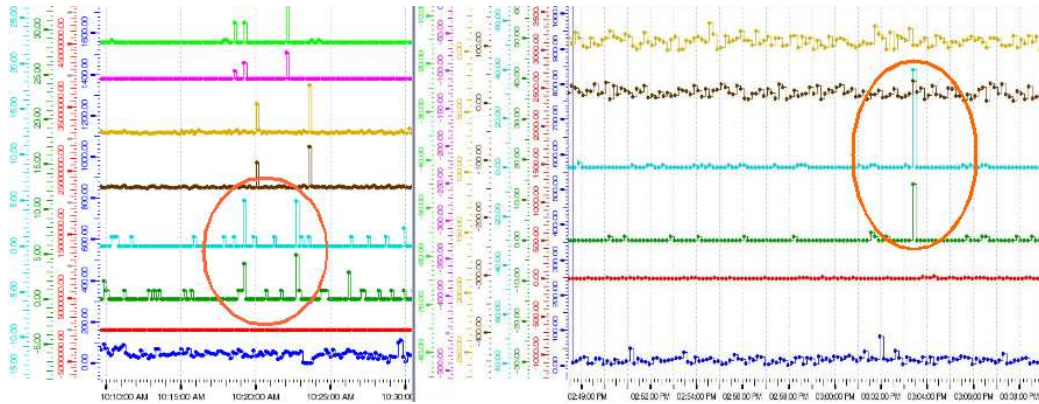


Figure 6.11: *Details of Beam Monitor FSM main panel. Hit rates registered in September 10th “splash events” from Beam 1 (left) and Beam 2 (right) by three systems: LUCID, L1Calo and MBTS.*

6.6 Conclusion

In this Chapter the LUCID Detector Control System has been described. Crucial parameters like high voltage and pressure are continuously monitored and a stability within 1% has been established. During bake-out of the beam pipe, the cooling system has kept the temperature of the vessels well below the critical value, with a minimum value of 10° Celsius difference. LUCID Finite State Machine has been implemented ensuring safe operation of the detector. DCS and FSM have been successfully tested during first beam event in September 2008.

Chapter 7

LUCID Simulation

Monte Carlo simulations have been carried out in order to investigate the response of the detector to inelastic pp interactions occurring at the interaction point of ATLAS. All results presented in this chapter are obtained with a version of the detector geometry made of 32 Cherenkov tubes (out of 40) read out by photomultipliers (Phase I project).

7.1 Introduction

The study of the LUCID simulation is divided in three steps.

The first step is the description of the geometry of the detector in a stand-alone GEANT4 simulation (Section 7.2).

The second step is the study of the detector response to particles of a given energy, position and directions, as illustrated in Section 7.3.

Finally, in Section 7.4 inelastic pp collisions at the center of mass energy of 14 TeV are generated to simulate the production and the decay of particles according to the current knowledge of cross sections and branching ratios. Particles are fed through the ATLAS detector simulation to describe the interaction of primary particles with the different detector materials they cross along their path. All primary and secondary particles are finally used as input for the last simulation step in which the performance of LUCID is studied using a dedicated stand-alone simulation. Background originating from beam halo and beam-gas interactions is not simulated. The main features of tracks entering the LUCID volume are compared to those which are detected.

7.2 Detector description

A realistic simulation of LUCID, including the main detector elements (vessel, cooling system, radiator, tubes, optical surfaces and PMTs) has been developed in a stand-alone GEANT4 simulation (4.7.1p01).

LUCID consists of two detector modules located at a distance of about 17 m from the pp interaction point (IP). Each module is made of twenty aluminium tubes pointing at the IP (see Figure 7.1).

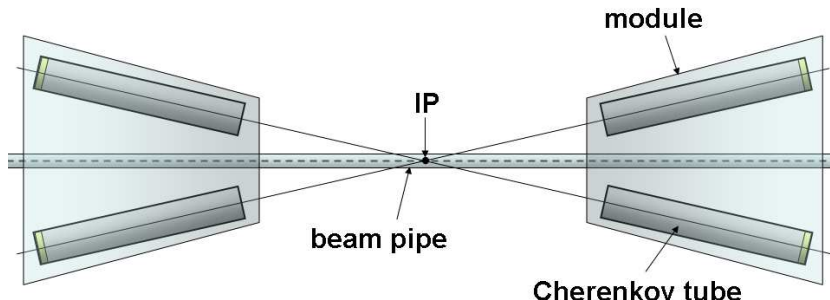


Figure 7.1: *Schematic view of IP pointing geometry of four LUCID tubes (not in scale).*

Tubes are located in a pressure tight aluminium vessel which contains a Cerenkov gas radiator (C_4F_{10} at 1.1 bar). Sixteen tubes per module are directly coupled to the read-out photomultipliers (PMT). A cooling system keeps the vessel temperature well below the critical value for a correct behaviour of the PMTs (50° Celsius). Four tubes per module are read-out via optical fibers. All these parts of the detector are simulated with a Monte Carlo based on GEANT4 code.

A sketch of the geometrical description of a single Cerenkov tube is reported in Figure 7.2

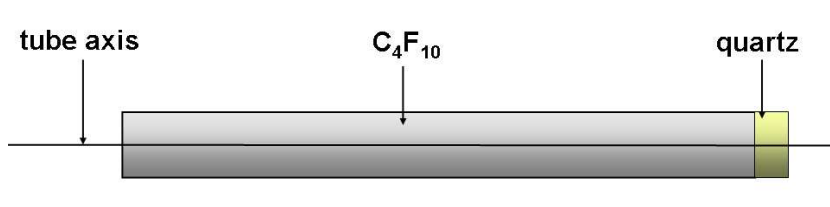


Figure 7.2: *Geometrical description of the Cherenkov tube (not in scale).*

The PMT is simulated with a thin quartz disc matching the trasversal dimension of the tube. The simulation of the PMT quartz window is crucial since it acts as photon emitter, as well as the main gas radiator.

All parameters used to describe the detector geometry are listed in Table 7.1.

Gas pressure [bar]	1.1
Gas temperature [kelvin]	293.15
Gas type	C_4F_{10}
Pmt type	R762 (hamamatsu)
Distance from the IP [mm]	16715.5
Pmt thickness [mm]	1.2
Pmt radius [mm]	7.0
Tube thickness [mm]	1.0
Tube length [mm]	1495
Tube radius [mm]	7.0
Distance Tube-Beam [mm]	96.3 (ring1), 114.7 (ring2)
Cooling radius [mm]	78
Cooling thickness [mm]	2
Vessel length [mm]	1532
Vessel inner radius [mm]	85
Vessel outer radius [mm]	125.15 (min), 147 (max)
Vessel inner thickness [mm]	2.5
Vessel outer thickness [mm]	3.0
Vessel bulkhead thickness [mm]	3.2

Table 7.1: *Parameters used for the geometrical description of LUCID.*

Light emission

Cerenkov light is emitted when a charged particle traverses a material with a speed (v) larger than the speed of light in the medium (c/n)

$$v > \frac{c}{n} \rightarrow \beta = \frac{v}{c} > \frac{1}{n} \quad (7.1)$$

where n is the refraction index of the radiator.

A detailed description of the characteristics of Cerenkov light emission can be found in [33].

The minimal velocity at which Cerenkov emission takes place (c/n) corresponds to an energy threshold (E_{th}) given by

$$E_{th} = \gamma m_0 c^2 = \frac{m_0 c^2}{\sqrt{1 - \left(\frac{v}{c}\right)^2}} = \frac{m_0 c^2}{\sqrt{1 - \left(\frac{1}{n}\right)^2}} \quad (7.2)$$

where m_0 is the rest mass of the charged particle. The emission angle (θ_C) is a function of the refraction index of the medium:

$$\cos \theta_C = \frac{1}{\beta n}. \quad (7.3)$$

For a gaseous radiator, the refraction index of the material (n) depends on the energy (E) of the emitted photons, on the pressure (P) and the temperature (T) of the radiator, according to the formula

$$n = \sqrt{\frac{2x + 1}{1 - x}}, \quad \text{where } x = x(E, P, T) = \frac{KP}{T} \frac{1}{1 - \left(\frac{E}{E_0}\right)^2}. \quad (7.4)$$

For C_4F_{10} , when P is in bar, T in kelvin and E in eV, the constants assume the values $E_0 = 17.0$ and $K = 0.25938$. The refraction index of C_4F_{10} and quartz as a function of the wavelength of the emitted Cerenkov light is reported in Figure 7.3.

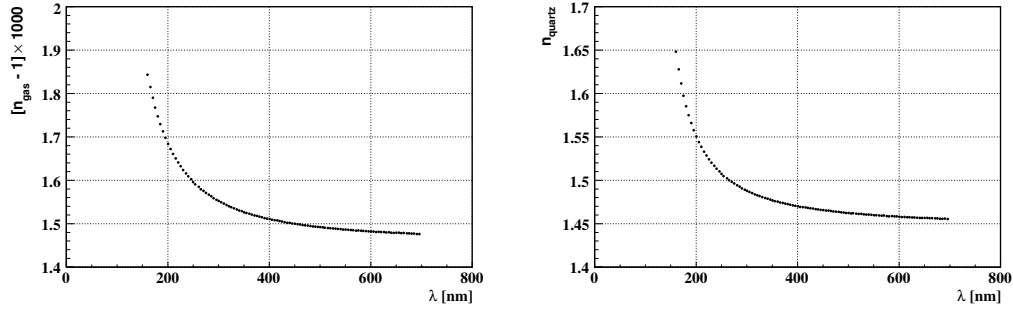


Figure 7.3: *Refraction index of C_4F_{10} (left) and quartz (right) as a function of photon wavelength.*

The number of photons emitted per unit of length (L) in the wavelength range $[\lambda_1, \lambda_2]$ has a simple expression in case of long radiators ($L \gg \lambda$) [33]:

$$\frac{N}{L[\text{nm}]} = 2\pi\alpha \sin^2 \theta_C \int_{\lambda_2}^{\lambda_1} \frac{d\lambda}{\lambda^2} = 2\pi\alpha \left[1 - \left(\frac{1}{\beta n}\right)^2 \right] \int_{\lambda_2}^{\lambda_1} \frac{d\lambda}{\lambda^2}. \quad (7.5)$$

According to this relation, a relativistic charged particle ($\beta \approx 1$) crossing a LUCID tube along its axis at $P = 1.1$ bar, $T = 293.15^\circ$ kelvin emits about 730 photons in the gas and 100 in the quartz in a wavelength range between 200 nm and 700 nm (see Table 7.2).

	L [mm]	$\langle n \rangle$	θ_C [°]	$E_{th}(\pi)$ [MeV]	$E_{th}(e)$ [MeV]	N
C_4F_{10}	1495	1.00149	3.1	2700	9.3	730
Quartz	1.2	1.46	46.8	190	0.7	100

Table 7.2: C_4F_{10} and quartz parameters used for a calculation of Cerenkov photon emission inside LUCID.

Density and thickness of the quartz window are such that Cerenkov effect in the PMT is not negligible with respect to that occurring in main LUCID gas radiator.

Light propagation and detection

After being emitted in C_4F_{10} with a typical angle of $\sim 3^\circ$, photons are reflected by the inner walls of the tube with a certain efficiency (reflectivity). Depending on the position where they are generated, multiple reflections might occur before they actually reach the read-out photomultipliers (see Figure 7.4).

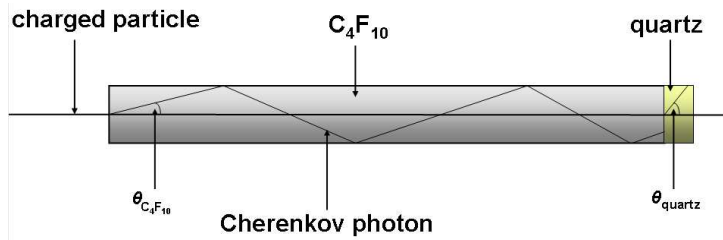


Figure 7.4: Light propagation inside a tube.

The average number of reflections of light in the tube before reaching the PMTs is 2.8. Photons which are not absorbed by the gas reach the end of the tube and are converted by the photomultipliers into photoelectrons. The conversion efficiency (quantum efficiency), which is wavelength dependent, is provided by the manufacturer (Hamamatsu), and is used in the simulation.

Tube reflectivity, which is also a wavelength dependent parameter, and quantum efficiency are used to simulate the propagation and detection of light inside LUCID in the wavelength range accepted by the PMTs [160nm, 650nm] (see Figure 7.5).

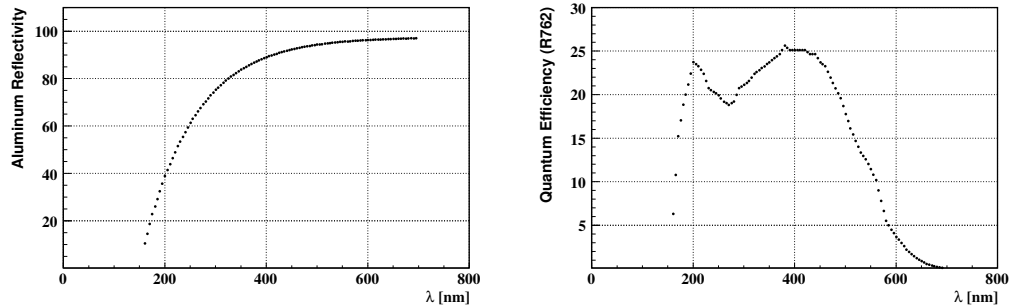


Figure 7.5: *Aluminium tube reflectivity (left) and PMT quantum efficiency (right) as a function of photon wavelength.*

Gas absorption length is 6 m from 650 to 200 nm and suddenly drops to 1 mm at $\lambda = 150$ nm. For the PMTs, the quantum efficiency contains the wavelength dependence of the absorption length in quartz.

7.3 Response to a particle gun

Primary particles originating from the Interaction Point in one case travel exactly along the tube axis (on-axis), in the other case travel along an random angle (off-axis).

Signal from on-axis particles

The geometry of LUCID is such that particle originating from the interaction point (primary) produce more light than particles coming from any other direction (secondaries).

The detector response to primary particles is obtained by using 180 GeV charged pions travelling exactly along the tube axis. The number of photoelectrons read-out by the PMT is shown in Figure 7.6.

A particle entering the tube and travelling along the tube axis traverses the gas first, and then the quartz window of the photomultiplier. The red histogram, peaked at about 75 photoelectrons, represent the amount of Cerenkov light emitted into the gas, whereas the photons emitted into the quartz are represented by the green histogram, which shows a maximum at

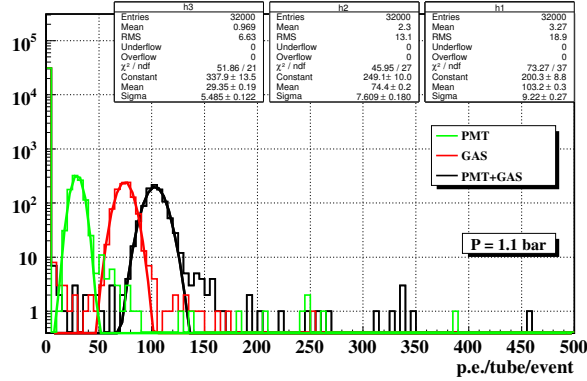


Figure 7.6: Photo-electrons per tube per event read-out by LUCID when one pion per event is shot along the tube axis.

about 30 photoelectrons. The total emitted Cerenkov light is the sum of the two contributions and is peaked at about 105 photoelectrons.

The solid lines superimposed to the histograms are the result of the fit. The width is dominated by the Poissonian nature of the photoelectron generation inside the PMT.

The wavelength spectrum of light propagating in LUCID is illustrated in Figure 7.7, where the wavelength distribution is shown at different propagation steps.

The wavelength distribution of generated photons (black line) exhibits a $1/\lambda^2$ shape, which is characteristic of Cerenkov emission. Generated photons traverse the gas and are reflected by the aluminium walls of the tube until they reach the quartz window (red line): the suppression at low λ is due to absorption inside the gas and to reduced aluminium reflectivity. The effect of quantum efficiency is visible on the spectrum of detected photons (green line), which are strongly suppressed above 600 nm.

Signal from off-axis particles

In a more realistic scenario, primary particles originating from pp collisions travel along directions different from the tube axis.

Since the diameter of the tube is small compared to the distance between LUCID and the interaction point, the angle between the trajectory of an off-axis primary particle entering the tube and the tube axis is negligible. Secondary particles produced on the detector walls might cross the Cerenkov radiators (gas or quartz) and release light which will be added to the signal of the original primary particle. The trajectory of secondary particles is

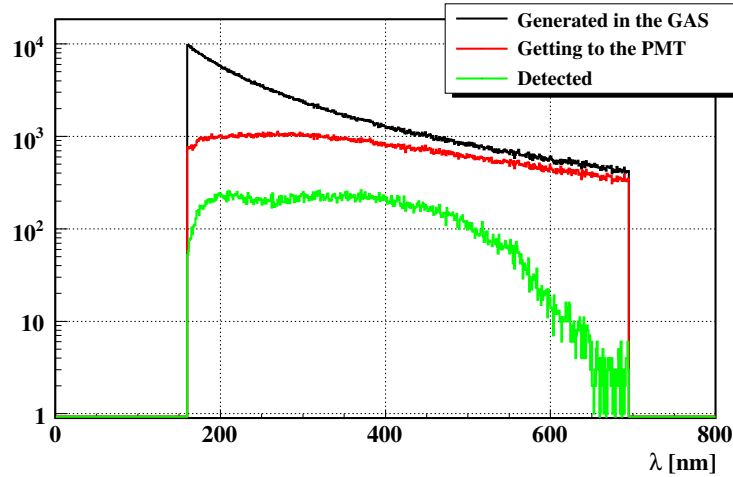


Figure 7.7: *Wavelength distribution of photons generated by an on-axis charged pion inside a LUCID tube. The distributions of photons propagating up to the PMT and finally detected are superimposed.*

typically transverse with respect to the axis of the Cerenkov tube, thus the emission of light is smaller than the one emitted by a primary particle (see Figure 7.8).

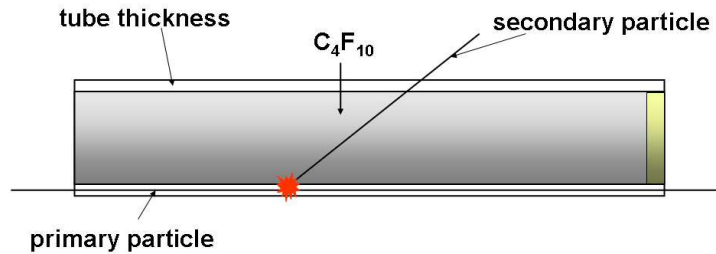


Figure 7.8: *Path of secondary particles produced by the interaction of a primary particle with the tube walls.*

Off-axis primary particles are simulated by shooting 180 GeV pions from the IP with a flat azimuthal angle distribution (between 4 and 10 mrad). The resulting photoelectron spectrum is shown in Figure 7.9, with different assumptions on secondary interactions inside LUCID.

As one can see, the total spectrum of photoelectrons shows two peaks. The peak at about 100 photoelectrons is due to particles, mainly primaries,

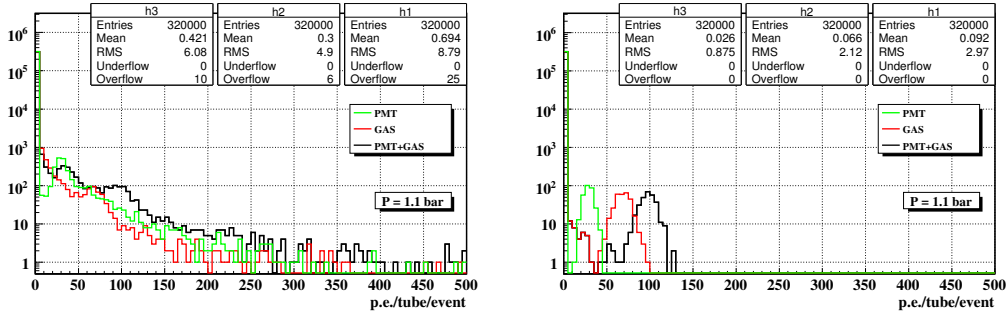


Figure 7.9: *Distribution of photoelectrons produced in LUCID by 180 GeV pions originating from the IP along a random direction (left). Right plot shows the effect of neglecting secondary interactions inside the detector material, obtained by reducing the tube walls to zero.*

crossing both Cerenkov radiators (gas and quartz). The peak at 30 photoelectrons originates from particles crossing only the quartz. This is possible only for secondary particles.

Compared to Figure 7.6, a continuous background is created by secondary particles. Even though tubes are thin (≈ 1 mm), the effective thickness traversed by off-axis primaries is large (≈ 1500 mm), which results in a large probability for secondary interactions. The effect is only partially suppressed by the smaller path length of secondaries inside the Cerenkov radiator.

7.4 Response to inelastic pp collisions

Event generator

Several packages are available for the simulation of the physics processes occurring in pp collision. The difference among them reflects the uncertainty on the models which are used to describe the interaction of protons. The choice of the generator is not unique. Different generators can be used to evaluate the effect of the different physics models.

The known physics processes which are expected to have larger impact on the performance of LUCID are inelastic pp collisions. There are three types of inelastic events: single-, double- and non-diffractive.

Particles produced in diffractive processes are expected to cluster in specific ranges of pseudo-rapidity (see Figure 7.11).

The production cross section of the different inelastic processes predicted by two generators (PYTHIA and PHOJET) at the center-of-mass energy of 14 TeV are reported in Table 7.3.

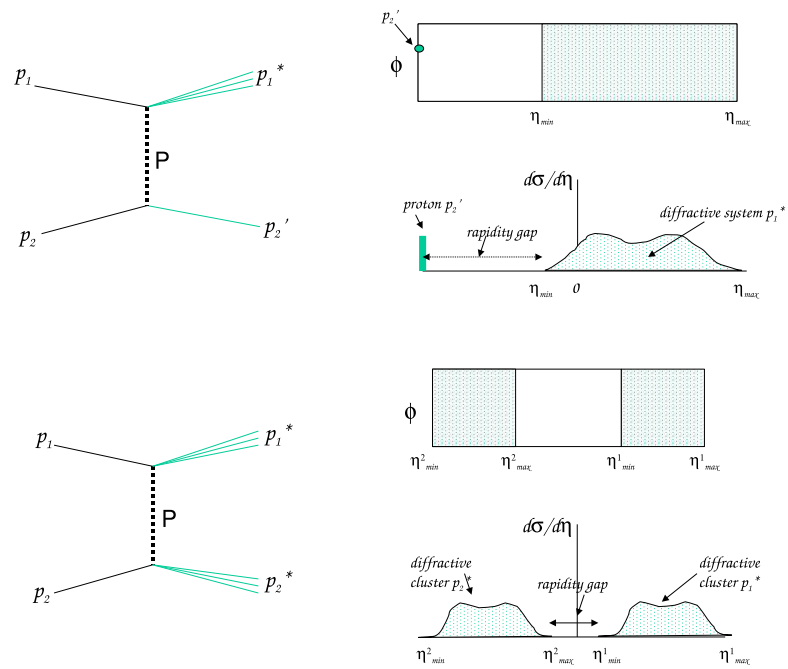


Figure 7.10: Illustration of the concept of rapidity gap for single-diffractive (top) and double-diffractive (bottom) processes.

Type of pp collision	σ [mb] in PYTHIA	σ [mb] in PHOJET
Non-diffractive	55.2	64.9
Single-diffractive	14.3	10.8
Double-diffractive	9.7	4.0
Total	79.2	79.7

Table 7.3: Cross section of the different inelastic processes (single-, double- and non-diffractive) predicted by PYTHIA and PHOJET [11].

According to both generators, the most frequent inelastic collisions are non-diffractive. The pseudo-rapidity distribution of particles produced in single-, double- and non-diffractive processes predicted by PYTHIA and PHOJET are shown in Figure 7.11 [11].

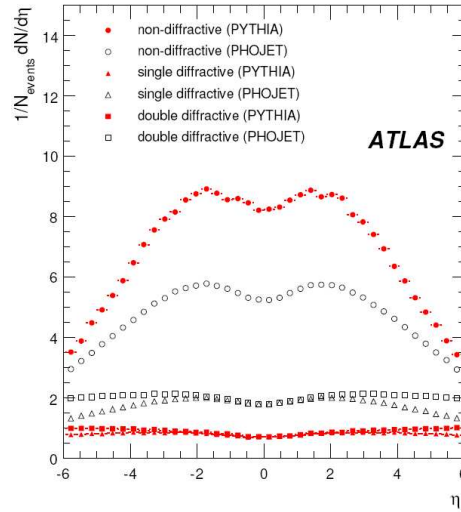


Figure 7.11: Pseudo-rapidity distributions predicted by different event generators for different physics processes. Open (close) symbols correspond to PHOJET (PYTHIA).

The prediction of PYTHIA and PHOJET are close, as far as single- and double-diffractive events are concerned. The largest discrepancies are observed at low values of pseudo-rapidity for non-diffractive events, and over the whole pseudo-rapidity range for single- and double-diffractive events. There is no ground to consider one generator more reliable than the other. The study presented in this thesis is done with a sample of about 10000 events of single pp interactions generated with PHOJET 1.12 in a pseudo-rapidity

range [5.3, 6.1].

7.4.1 Track propagation inside ATLAS and LUCID

Particles generated by PHOJET 1.12 are fed through a GEANT4 simulation of the ATLAS detector including all sub-systems (magnets, trackers, calorimeters etc.), with the exception of LUCID. The ATLAS detector geometry used in a previous study of radiation background [26] is chosen for the particular attention given to low energetic processes, such as electromagnetic showers, which are essential for the study of radiation background.

Being located close to the beam pipe, upstream of the forward muon shielding, LUCID is exposed to a large flux of secondary particles. In fact, primary particles produced by inelastic pp collisions at the interaction point interact with the material of the experiment producing secondary particles that may reach the LUCID volume from any directions.

The energy threshold for detecting charged particle in LUCID (10 MeV for electrons) is such that the effect of secondary particles might be consistent.

The original idea behind the LUCID design was to build a detector which was even capable to distinguish between primary and secondary particles. Due to the projective geometry of LUCID, primary particles travel longer paths inside a tube compared to secondary particles (see Figure 7.12). Primary particles are then expected to emit more Cerenkov light than secondaries.

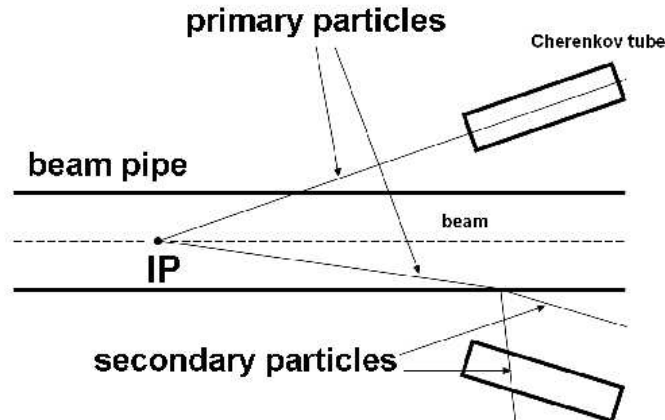


Figure 7.12: *Schematic view of the paths travelled by primary (solid line) and secondary particles (dashed line). Here the secondaries are due to interaction between the primary and the beam pipe.*

LUCID volume

The LUCID volume is defined in the region where LUCID is located, reproducing the external vessel where the Cerenkov tubes are contained. The position and the four-vector (energy and momentum) of all particles hitting the surface delimiting this volume is recorded, together with the information on the type and the origin (primary or secondary) of the particle. The coordinates of the impact points is shown in Figure 7.13. The volume is defined in such a way that it contains LUCID but it must not be too large in order not to superimpose to other objects.

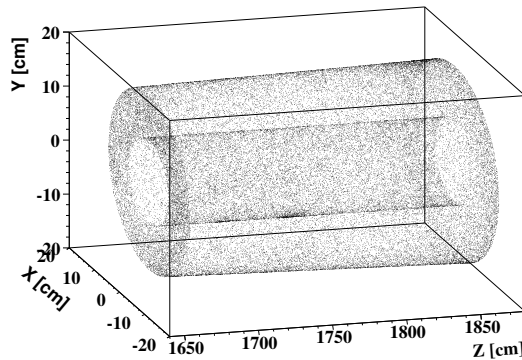


Figure 7.13: *LUCID volume (z coordinate is along the beam axis).*

One can compare the number of particles generated at the IP with that of primary and secondaries reaching the LUCID volume (see Figure 7.14).

The dashed line represents the primary particles produced at the interaction point. They are mostly pions, produced by the interaction of the quarks. The plot shows that a large fraction of primary charged pions travel up to the LUCID volume (filled grey). Photons from $\pi^0 \rightarrow \gamma\gamma$ prompt decays are also labelled as primary particles, but most of them is absorbed before reaching LUCID. The solid line represents the secondary particles reaching the LUCID volume. They are mostly electrons and photons from electromagnetic showers, and neutrons due to back-scattering from the material placed downstream of LUCID.

Particle direction

The number of photoelectrons produced by a charged particle crossing a LUCID tube is proportional to the path length inside the Cerenkov radiators (gas and quartz). Particles coming from the interaction point and hitting

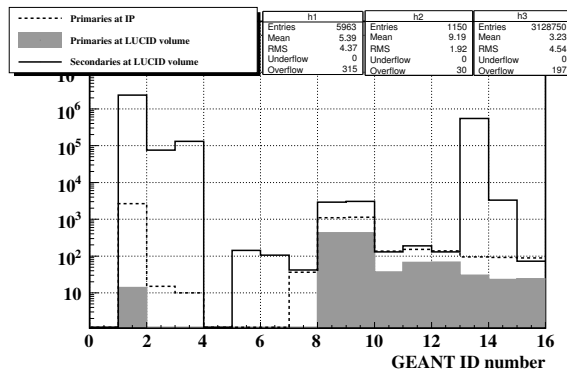


Figure 7.14: *Distribution of particles generated at the IP (dashed line), primary (filled grey) and secondary particles (solid line) reaching the LUCID volume, according to their GEANT4 identification number.*

the LUCID volume on the side facing the interaction point are expected to travel the longer path inside the tubes and give the larger contribution of photoelectrons.

In order to study the correlation between the original direction of the particle and the strength of the signal inside LUCID, a direction is associated to each particle. The coordinate of the impact point (x, y, z) and the momentum (p_x, p_y, p_z) of primary and secondary particles allow to define a direction for each particle, even though the criterion is somewhat arbitrary. In this analysis, particles are divided in three classes:

- “front”;
- “side”;
- “back”.

If $z \times p_z < 0$, the particle is defined “back”. If the particle is not “back” and if $|z| > 16601$ mm, the particle is defined “side”. The remaining particles are defined “front”.

The z coordinate (the one along the beam axis) of the impact point of all particles on LUCID volume is plotted in Figure 7.15.

The larger part of “front” particles are secondaries (red line). As expected, “side” and “back” primaries are negligible, and do not appear in the plot. Secondaries not coming directly from the interaction point are mostly “side” (blue line).

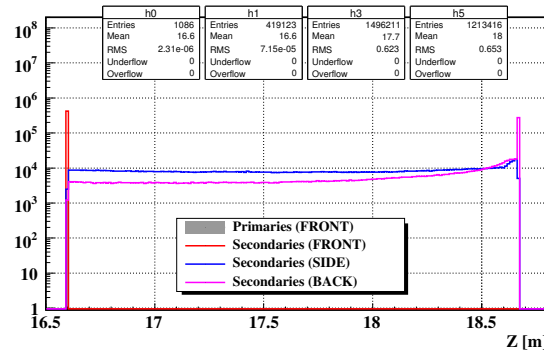


Figure 7.15: Distance along the beam axis from the interaction point of the impact point on LUCID. The results are shown for the three classes of particles: “front”, “side” and “back” (the definition is given in the text).

Track propagation inside LUCID

The impact point, the arrival time and the energy at the LUCID volume is used as seed for track propagation inside the volume with the stand-alone GEANT4 simulation presented in Section 7.2. One important feature of the analysis presented in this chapter is the traceability of primary particles. If a primary particle generates secondaries inside the LUCID detector material, the release of light due to secondaries is associated to the original primary track.

7.4.2 Tube based information

Photoelectron spectrum

The response of LUCID to inelastic pp collisions in terms of photoelectrons per tube per event is shown in Figure 7.16.

On the left plot, peaks at the expected position for production of photoelectrons in the gas (75) and quartz (30) are visible, together with their sum at 105 photoelectrons.

Together with the total number of photoelectrons, the plot on the right shows three contributions: primary particles (grey area), “front” secondaries (red line) and “side” secondaries (green line). The spectrum of primary particles is similar to the one shown in Figure 7.9, which was obtained shooting high energy pions from the IP with a flat azimuthal angle distribution.

Compared to those coming from the “front”, “side” secondaries travel a smaller path into the tube, thus releasing less Cerenkov light.

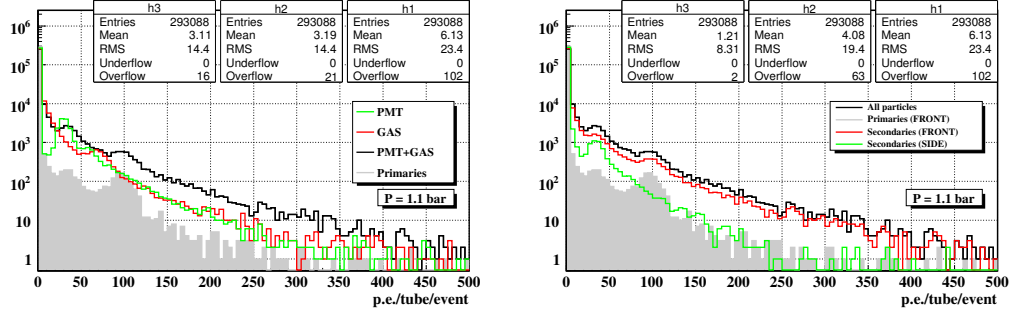


Figure 7.16: Spectrum of photoelectrons read-out by LUCID in 9159 inelastic pp collisions. Contributions from different radiators (left) and particle directions (right) are shown.

Hit definition

A PMT signal is not always due to Cerenkov light produced by a particle. Light detection related effects, such as dark current and thermoionic emission, may generate noise photoelectrons which can be rejected by setting a threshold, provided that signals of “real” particles are not rejected.

The average number of photoelectrons produced by an on-axis primary particle is about 105 (Figure 7.6). The largest fraction of secondaries release light in the PMT only (30 photoelectrons). A cut-off threshold of 50 photoelectrons allows to keep the entire signal of primary particles, while suppressing large fraction of secondaries which are not directly correlated with primary particle. A LUCID hit can be defined as a release of light in a tube larger than 50 photoelectrons.

Event efficiency, hit multiplicity and tube occupancy

The probability to detect a pp interaction (event efficiency) depends on the criteria used to define a hit. If at least 1 hit is required (single side mode), the efficiency is $(55.8 \pm 0.05)\%$. If at least 1 hit in both LUCID module is required (coincidence mode), the efficiency is $(13.5 \pm 0.04)\%$.

The average number of hits per collision is 1.21 ± 0.02 in single side mode, and 0.49 ± 0.01 in coincidence mode. The smaller value in coincidence mode can be explained as due to the smaller probability of having a hit simultaneously in both modules. For each tube, the probability of registering at least one hit is $(3.66 \pm 0.01)\%$, more or less independently of the tube position. This value can also be obtained by dividing the average number of hits per collision in single side mode to the number of tubes (32). Hit multiplicity and tube occupancy are reported in Figure 7.17.

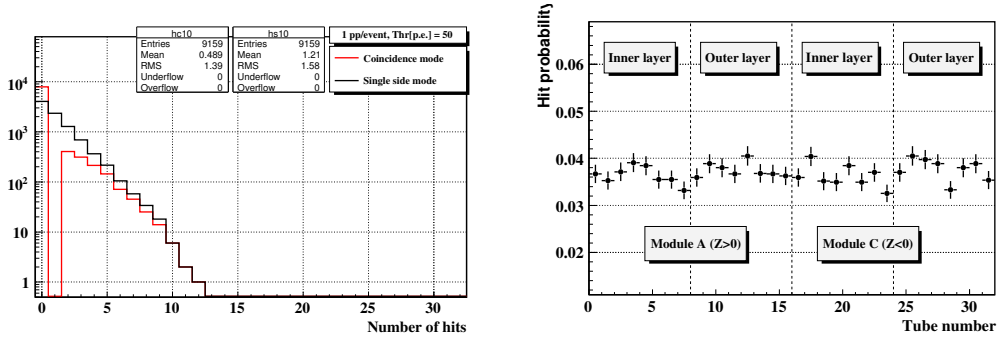


Figure 7.17: Number of hits registered by LUCID (left) and tube occupancy (right) per pp interaction, with a threshold of 50 photoelectrons.

7.4.3 Track based information

The main features of tracks entering the LUCID volume are compared to those of tracks detected by LUCID when a signal of at least 50 photoelectrons is registred.

Pseudo-rapidity

The LUCID tubes cover the pseudo-rapidity range [5.61, 5.92].

In Figure 7.18, the pseudorapidity of generated primary particles is compared to that of particles detected in LUCID.

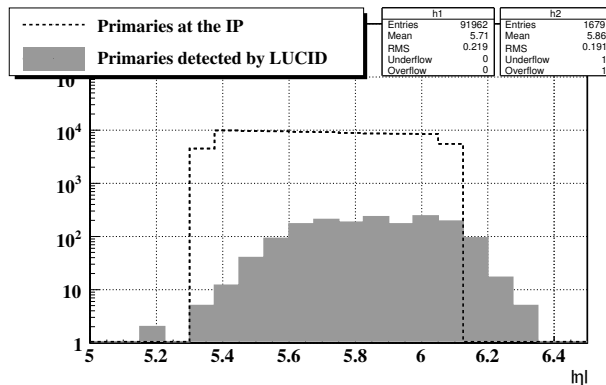


Figure 7.18: Pseudorapidity distribution of charged primaries generated at the Interaction Point (dashed line) and detected by LUCID (greyed area).

The pseudorapidity of primaries detected by LUCID is calculated using the angle of incidence on the LUCID volume. Due to possible scattering

of primaries with the material, this angle can be different from the original angle at the Interaction Point. This effect produces an excess of primaries outside the range of pseudorapidity generated at the IP (grey histogram in Figure 7.18).

In addition, primary particles entering the LUCID volume at pseudorapidity values beyond the range of LUCID may generate secondary particles before getting into LUCID, which then enter a tube and release a signal over threshold.

Time of flight

Particles produced by protons colliding at 14 TeV center of mass energy travel approximately at the speed of light inside the ATLAS detector.

The time needed by primary particles to cover the distance from the interaction point to the front side of LUCID on a straight line is about

$$t \simeq \frac{\text{distance between IP and LUCID}}{\text{speed of light}} = \frac{17 \text{ m}}{2.99 \times 10^8 \text{ m/s}} \simeq 56 \text{ ns.} \quad (7.6)$$

The time of arrival of secondaries is expected to be longer since they travel longer paths before hitting LUCID. This is especially true for side and back secondary particles.

The time of flight of particles produced at the IP and reaching the LUCID volume is shown in Figure 7.19.

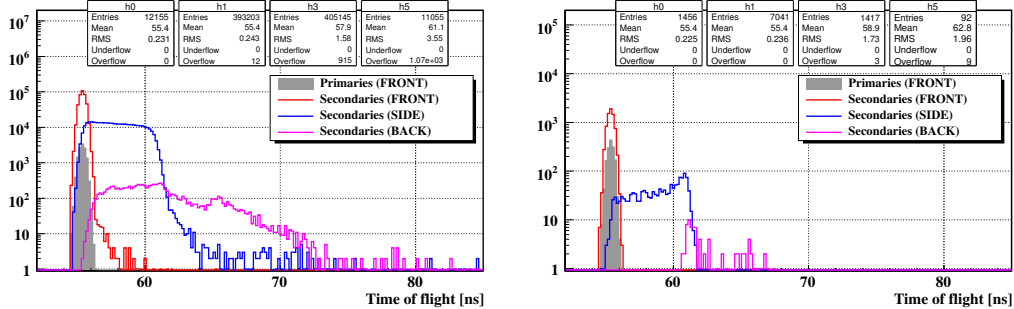


Figure 7.19: The left plot shows the time of arrival of all particles from the IP to the LUCID volume. The right plot is the same plot obtained for particles detected by LUCID (> 50 photoelectrons).

A comparison between the left and right plots shows in particular that most of the detected “side” secondaries travelled a long path before reaching LUCID.

Moreover, the results of the simulation indicate that “front” secondaries are within 2 ns almost in time with primaries, whereas “side” secondaries have a delay of up to 6 ns.

At the moment this thesis is being written, the LUCID collaboration is studying the possibility to upgrade the detector for a Phase II running at LHC design luminosity. One of the proposals to suppress background from “side” secondaries is to apply a time gate on the electronic signal (3 ns coincidence).

Angle with the beam

Primary and secondary particles hit almost simultaneously the front face of the LUCID volume. However, secondary particles, being the product of scattering of primary particles through different materials, are expected to travel along different directions with respect to primaries.

The angle between the beam axis and the trajectory of primary and secondary particles is shown in Figure 7.20.

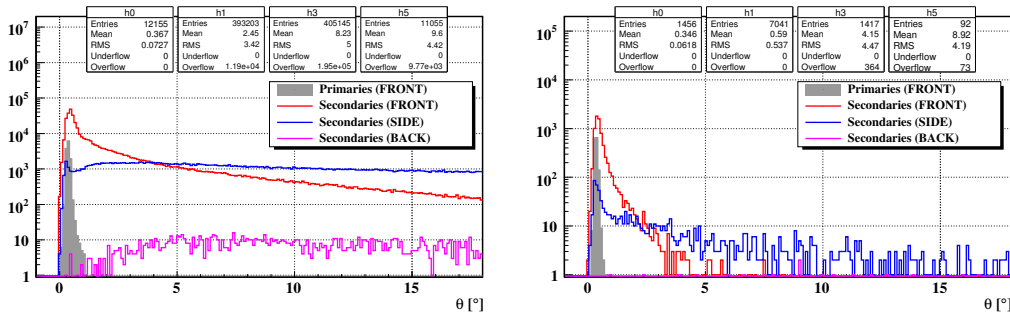


Figure 7.20: The left plot shows the angle with the beam axis of particles crossing the LUCID volume. The right plot is the same plot obtained for particles detected by LUCID (> 50 photoelectrons).

A comparison between the left and right plots shows that “front” and “side” secondaries with angle larger than 2 degrees are both strongly suppressed when arriving at the LUCID volume.

Primary particles form at most an angle of one degree with the beam. The peak of “front” secondaries is broader (two degrees) and the tail extends up to 20 degrees. Within this region, “side” secondaries have a flat angle distribution. Secondaries from the “back” are scattered at larger angles.

Energy

Most primary particles generated at the IP are pions. Pions are also generated in hadronic showers along the path of primary particles. In Figure 7.21

the energy distribution of primary and secondary pions are shown.

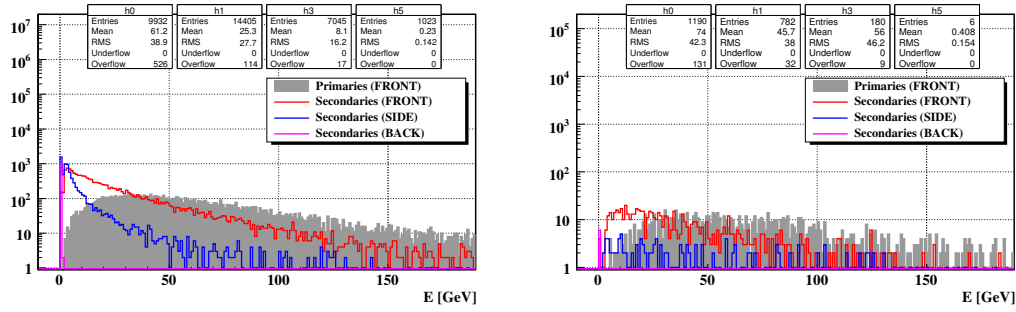


Figure 7.21: Energy distribution of pions crossing the LUCID volume (left) and detected by LUCID (right) requiring more than > 50 photoelectrons.

The requirement of being detected by LUCID suppresses the soft part of the energy spectrum. The average energy of a detected primary pion is 70 GeV, which is close to that of a secondary pion (50 GeV).

Secondary particles are mostly photons and electrons. In Figure 7.22 the energy distribution of secondary particles is shown.

As for pions, the requirement of being detected by LUCID has the effect of suppressing the soft part of the energy spectrum. The average energy of a detected “front” secondary electron is 2 GeV, while “front” secondary photons have 1 GeV. Secondary particles from the “back” are much slower.

7.5 Conclusion

LUCID detects charged particles in the pseudo-rapidity range $[5.61, 5.92]$. Light yield is 105 photoelectrons in the wavelength range $[160\text{nm}, 650\text{nm}]$. The largest fraction of the signal originates from the gas (≈ 75), the rest is coming from the PMT quartz window (≈ 30).

With a cut-off threshold of 50 photoelectrons, the probability to detect inelastic pp collisions is $(55.8 \pm 0.05)\%$, if at least 1 hit in LUCID is required, and $(13.5 \pm 0.04)\%$, when a coincidence between the two detector modules is requested. The average number of hits per collision is 1.21, resulting in a tube occupancy of $(3.66 \pm 0.01)\%$.

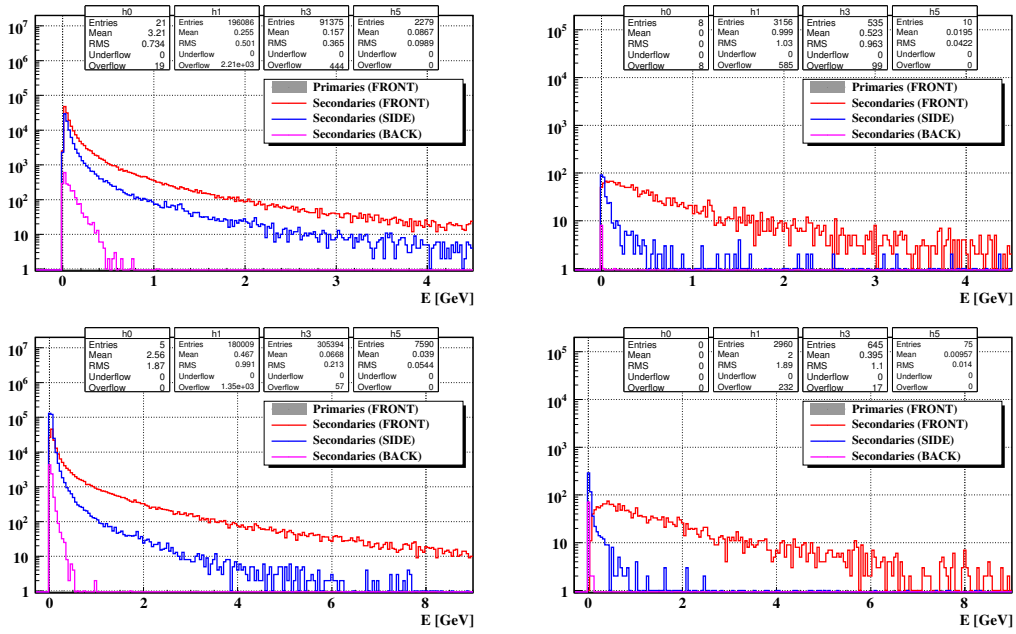


Figure 7.22: Energy distribution of photons (top) and electrons (bottom) crossing the LUCID volume (left) and detected by LUCID (right) requiring more than > 50 photoelectrons.

Chapter 8

Luminosity monitoring

The performance of LUCID, the ATLAS luminosity monitor, are evaluated by means of Monte Carlo simulations. When the average number of interactions per bunch crossing is small ($\mu < 2$), a method based on empty bunches counting gives an accuracy of 1%. A method based on a special calibration procedure can be used for any μ with an accuracy better than 3%.

8.1 Introduction

Given a physical process with cross section σ , the average luminosity per bunch crossing is defined as the ratio between the average number of interactions per bunch crossing (μ) and the cross section:

$$\mathcal{L}_{BX} = \frac{\mu}{\sigma} \quad (8.1)$$

The task of a luminosity monitor is to provide a response which is linear with μ in order to extrapolate absolute luminosity measurements performed at a certain luminosity to any other value. A detailed study of luminosity monitoring in ATLAS with a toy Monte Carlo is reported in [34].

For the measurement of luminosity, two scenarios can be defined. In the *calibration scenario*, luminosity is so low that the probability of having bunches with overlapping interactions is negligible ($\mu \ll 1$). This is needed to calibrate the detector by evaluating the response to a single pp interaction. A *measurement scenario* is any other scenario in which a luminosity monitor is asked to provide the luminosity.

The average bunch luminosity \mathcal{L}_{BX} relates to the instantaneous luminosity L by the bunch crossing frequency ($f_{rev} = 40$ MHz) and the number of circulating bunches (n_{BX}):

$$L = \mathcal{L}_{BX} \cdot f_{rev} \cdot \frac{n_{BX}}{3564} \quad (8.2)$$

Luminosity monitors in ATLAS are asked to cover a wide range of luminosities, from $L = 10^{27} \text{ cm}^{-2}\text{s}^{-1}$ to $L = 10^{34} \text{ cm}^{-2}\text{s}^{-1}$ (LHC design). At the lowest value, the ALFA detector [12] will measure absolute luminosity from elastically scattered protons with a goal accuracy of about 3%. A less precise measurement (10 – 20% accuracy) is foreseen in special beam conditions when absolute luminosity can be determined from the measurement of beam transverse dimensions with a beam separation scan technique.

At design luminosity ($n_{BX} = 2808$ bunches), assuming $\sigma_{inel} = 80$ mb (see Table 7.3), the expected number of inelastic pp interactions per bunch crossing is $\mu \sim 25$. This means that luminosity monitors are required to provide a linear response also in cases of overlapping interactions.

In this chapter, Monte Carlo simulations of the full ATLAS detector described in Chapter ?? are used to study the performances of LUCID as a luminosity monitoring system in a wide range of luminosities.

8.2 Definition of detected interaction

As already discussed, LUCID consists of two modules placed symmetrically around the ATLAS interaction point. Two criteria to detect a pp collision are defined: single side mode and coincidence mode. In single side mode, an interaction is detected if there is at least 1 hit in *one module*. In coincidence mode, an interaction is detected if there is at least 1 hit in *both modules* (see Figure 8.1).

In a), each module detects a particle. This interaction is detected both in single side mode and in coincidence mode. In b), two particles traverse the same module, one of them giving a hit. This interaction is detected in single side mode only. In c) no particle traverses any modules, then no interaction is detected.

The advantage of requiring a coincidence is that background produced by beam interactions with residual gas inside the beam pipe or by the beam-halo with LHC collimators is reduced. Since they are uncorrelated with the ATLAS interaction point, such interactions are detected in one module only.

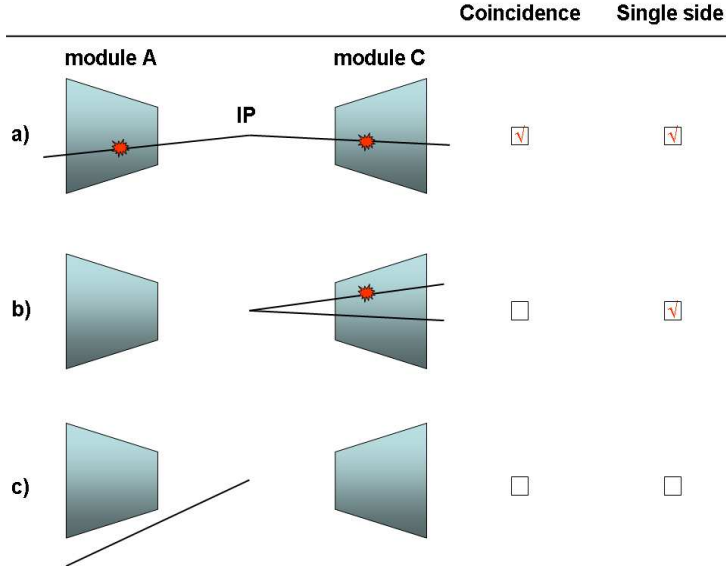


Figure 8.1: *Principle of detection in single side and coincidence modes.*

8.3 Monte Carlo simulation

The efficiency to detect an interaction in single side mode (ε^{Sing}), coincidence mode (ε^{Coin}), in side A (ε^A) and side C (ε^C) and the corresponding average number of hits per interaction are reported in Table 8.1. Efficiencies for side A and side C include the coincidences; in other words, they represent the probability of detecting an interaction regardless of what happens on the other module.

		ε [%]	$N_{hits/pp}$
Single Side	ε^{Sing}	55.8 ± 0.5	1.21 ± 0.02
Coincidence	ε^{Coin}	13.5 ± 0.4	0.49 ± 0.01
Module A	ε^A	34.3 ± 0.5	2.57 ± 0.02
Module C	ε^C	35.0 ± 0.5	2.53 ± 0.02

Table 8.1: *Efficiencies and average number of particles per interaction.*

The **measurement** samples are built by overlapping single inelastic collisions with a Poissonian distribution with average μ . To cover a wide range of luminosities, 10 samples are built with $\mu = 0.01, 0.05, 0.1, 1, 2, 5, 10, 15, 20, 25$. In order to increase the statistics, single interactions are used twice in each

sample. The detector responses in terms of photoelectrons per tube per event for two different luminosity values are shown in Figure 8.2.

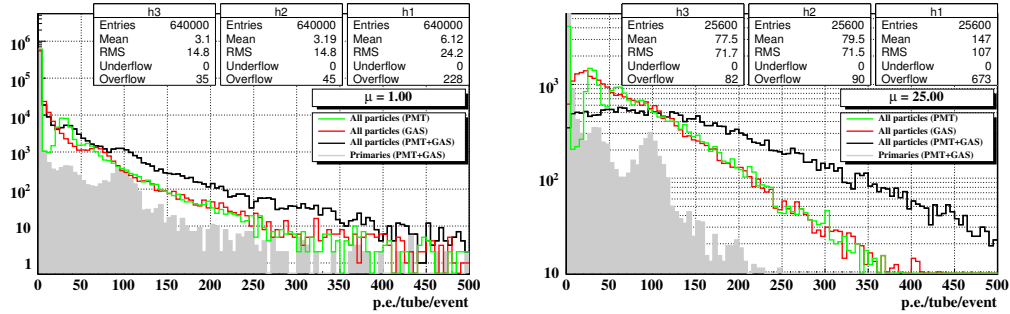


Figure 8.2: Photoelectron spectra when $\mu = 1$ (left) and $\mu = 25$ (right).

The average number of photoelectrons per tube per event increases from 6.1 to 147, when μ goes from 1 to 25. The shape of the total distribution becomes more flat. Due to the increase in track multiplicity, the signal of primary particles is hidden by the combinatorial background of secondaries crossing the tubes at large angles and giving small signals. This effect is called “migration effect”. The corresponding hit distributions with a cut-off threshold of 50 *p.e.* is shown in Figure 8.3.

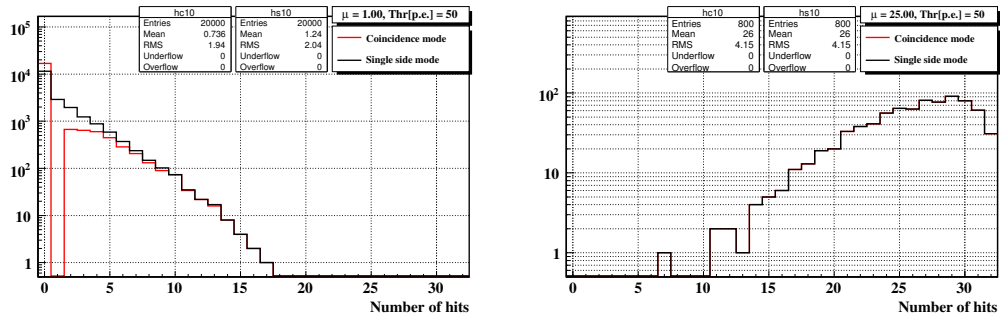


Figure 8.3: Hit distribution when $\mu = 1$ (left) and $\mu = 25$ (right), when the cut-off threshold is 50 photoelectrons.

For $\mu = 1$, the average number of hits per bunch crossing is 1.239 ± 0.008 in single side mode and 0.720 ± 0.006 in coincidence mode. For $\mu = 25$, the hit distributions in single side mode and in coincidence mode becomes indistinguishable. Due to the large detector occupancy, all detected events

have at least 1 hit in both modules. The average number of hits per bunch crossing is 25.99 ± 0.08 for both single side and coincidence mode.

8.4 Zero counting method

The basic idea of a zero counting method is to correlate μ to the frequency of empty bunch crossings (those without pp collisions).

The zero counting method has the advantage of simplicity since it just relies on counting events, rather than hits. A drawback of this method is that the rate of empty events decreases by increasing the luminosity, especially for detectors with large detection efficiency (*zero starvation*).

8.4.1 Single side mode

In single side mode, an interaction is detected if there is at least one hit in one detector module. Empty bunch crossings have 0 hits in both modules.

Calculation

The probability of having an empty bunch (N_0/N_{BX}) is given by two contributions:

I - probability of having 0 interactions;

II - probability of having n interactions with 0 hits in both modules.

Term I is the Poissonian probability of having zero interactions:

$$I = P_\mu(0) = \frac{e^{-\mu}\mu^0}{0!} = e^{-\mu} \quad (8.3)$$

Given the probability to detect an interaction in single side mode (ε^{Sing} , see Table 8.1), term II is the combined probability of not detecting the n interactions occurring in a bunch:

$$II = (1 - \varepsilon^{Sing})^n \quad (8.4)$$

Term II is convoluted with a Poissonian distribution of average μ (the sum starts from $n = 1$ to exclude term I):

$$\sum_{n=1}^{\infty} (1 - \varepsilon^{Sing})^n \frac{e^{-\mu} \mu^n}{n!} = \sum_{n=0}^{\infty} (1 - \varepsilon^{Sing})^n \frac{e^{-\mu} \mu^n}{n!} - e^{-\mu} = e^{-\varepsilon^{Sing} \mu} - e^{-\mu} \quad (8.5)$$

The total probability of observing an empty event is the sum of Equations 8.3 and 8.5:

$$\frac{N_0}{N_{BX}} = e^{-\mu} + e^{-\varepsilon^{Sing} \mu} - e^{-\mu} = e^{-\varepsilon^{Sing} \mu} \quad (8.6)$$

The average number of interactions per bunch crossing is related to the fraction of empty bunches by the formula:

$$\mu = -\frac{1}{\varepsilon^{Sing}} \ln \left(\frac{N_0}{N_{BX}} \right) \quad (8.7)$$

At design luminosity ($L = 10^{34} \text{ cm}^{-2} \text{ s}^{-1}$), the number of interactions per bunch is about 25, which implies a rate of empty bunches of $e^{-25} \times 40 \text{ MHz} = 5.6 \times 10^{-4} \text{ Hz}$ (40 MHz is the crossing rate).

Results

The average number of interactions per bunch crossing measured (μ_{meas}) with the zero counting method in single side mode is extracted from 10 Monte Carlo samples having different μ_{true} , for four values of the threshold ($Thr = 40, 50, 60, 70$ photoelectrons), using Equation 8.7 (see Figure 8.4).

For $\mu < 2$, the agreement between the measured and the expected number of interactions is within 1%, when a threshold of 50 p.e. is set.

At $\mu = 5$, migration effect starts to play a role: the probability to detect an interaction increases with μ compared to the calibration scenario. The number of observed empty bunch crossings is smaller than the one measured with an ideal detector without migration effect, causing an overestimate of μ . Due to the *starvation* of zero counting, for $\mu > 5$, the statistical uncertainty becomes dominant due to limited size of the Monte Carlo sample.

8.4.2 Coincidence mode

In coincidence mode, an interaction is detected if there is at least one hit in both modules. An empty bunch has 0 hits in at least one module.

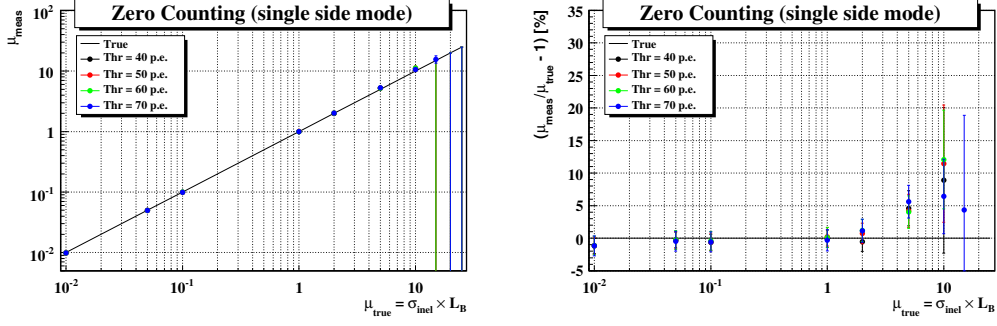


Figure 8.4: Average number of interactions per bunch crossing measured by counting the number of empty bunches when interactions are detected in single side mode (left), and difference from the expected value (right).

Calculation

The total probability of observing an empty bunch is the sum of four contributions:

- I - probability of having 0 interactions;
- II - probability of having n interactions with at least one interaction detected in module A, together with any number of interactions which are not detected in both modules;
- III - probability of having n interactions with at least one interaction detected in module C, together with any number of interactions which are not detected in both modules.
- IV - probability of having n interactions with 0 hits in both modules.

The term I is the Poissonian probability of having zero interactions:

$$I = P_{\mu}(0) = \frac{e^{-\mu} \mu^0}{0!} = e^{-\mu} \quad (8.8)$$

To evaluate contributions II, III and IV, *exclusive* efficiencies to detect a interaction (ε_1 , ε_2 , ε_3 and ε_0) are defined in Table 8.2.

Exclusive efficiencies in Table 8.2 are related to those *inclusive* defined in Table 8.1:

ε_1	probability of detecting an interaction in A, but not in C
ε_2	probability of detecting an interaction in C, but not in A
ε_3	probability of detecting an interaction in both modules
ε_0	probability of detecting no interactions ($=1 - \varepsilon_1 - \varepsilon_2 - \varepsilon_3$)

Table 8.2: *Efficiencies needed for zero counting method in coincidence mode.*

$$\begin{aligned}
\varepsilon_1 &= \varepsilon^A - \varepsilon^{Coin} \\
\varepsilon_2 &= \varepsilon^C - \varepsilon^{Coin} \\
\varepsilon_3 &= \varepsilon^{Coin} \\
\varepsilon_0 &= 1 - \varepsilon^A - \varepsilon^C + \varepsilon^{Coin}
\end{aligned} \tag{8.9}$$

Term II (III) consists of all permutations of k interactions detected in module A (C) and $n - k$ interactions not detected in any module:

$$II = \sum_{k=1}^n \varepsilon_1^k \varepsilon_0^{n-k} \binom{n}{k} = (\varepsilon_1 + \varepsilon_0)^n - \varepsilon_0^n \tag{8.10}$$

$$III = \sum_{k=1}^n \varepsilon_2^k \varepsilon_0^{n-k} \binom{n}{k} = (\varepsilon_2 + \varepsilon_0)^n - \varepsilon_0^n \tag{8.11}$$

Term IV is the probability of having a bunch crossing with n interactions which are not detected neither by any module singularly nor by the both modules together:

$$IV = \varepsilon_0^n \tag{8.12}$$

Terms II, III and IV are convoluted with a Poissonian distribution of average μ (the sum starts from $n = 1$ to exclude term I):

$$\sum_{n=1}^{\infty} \frac{e^{-\mu} \mu^n}{n!} [(\varepsilon_1 + \varepsilon_0)^n - \varepsilon_0^n] = e^{-\mu} [e^{-\mu(\varepsilon_1 + \varepsilon_0)} - e^{\mu\varepsilon_0}] \tag{8.13}$$

$$\sum_{n=1}^{\infty} \frac{e^{-\mu} \mu^n}{n!} [(\varepsilon_2 + \varepsilon_0)^n - \varepsilon_0^n] = e^{-\mu} [e^{-\mu(\varepsilon_2 + \varepsilon_0)} - e^{\mu\varepsilon_0}] \tag{8.14}$$

$$\sum_{n=1}^{\infty} \frac{e^{-\mu} \mu^n}{n!} \varepsilon_0^n = e^{-\mu}(e^{\mu\varepsilon_0} - 1) \tag{8.15}$$

The total probability of observing an empty event is the sum of Equations 8.8, 8.13, 8.14 and 8.15:

$$\frac{N_0}{N_{BX}} = e^{-\mu(1-\varepsilon_0-\varepsilon_1)} + e^{-\mu(1-\varepsilon_0-\varepsilon_2)} - e^{-\mu(1-\varepsilon_0)} \quad (8.16)$$

Given the relations in Table 8.2, Equation 8.16 can be written as:

$$\frac{N_0}{N_{BX}} = f(\mu) = e^{-\mu\varepsilon^A} + e^{-\mu\varepsilon^C} - e^{-\mu(\varepsilon^A + \varepsilon^C - \varepsilon^{Coin})} \quad (8.17)$$

The average number of interactions per bunch crossing is obtained by numerical inversion of Equation 8.17:

$$\mu = f^{-1}\left(\frac{N_0}{N_{BX}}\right) \quad (8.18)$$

Results

The average number of interaction per bunch crossing measured (μ_{meas}) with the zero counting method in coincidence mode is extracted from 10 Monte Carlo samples having different μ_{true} , for four values of the threshold, using Equation 8.18 (see Figure 8.5).

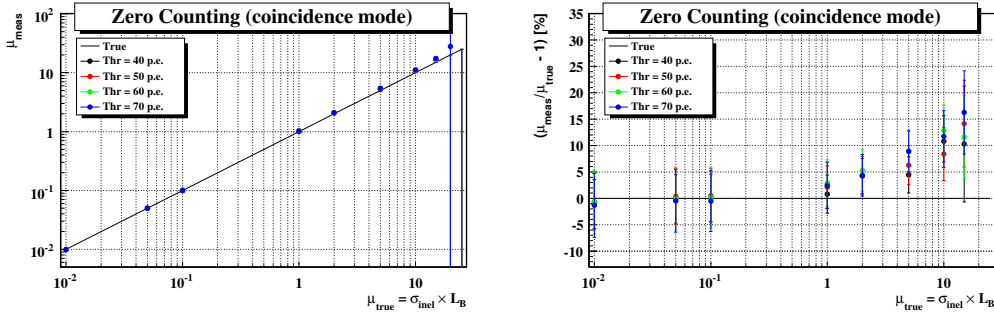


Figure 8.5: Average number of interactions per bunch crossing measured by counting the number of empty bunches when interactions are detected in coincidence mode (left), and difference from the expected value (right).

For $\mu < 1$, the agreement between the measured and the expected number of interactions is within 2%, when a threshold of 50 p.e. is set.

At $\mu = 2$, migration effect starts to play a role. The probability to detect an interaction increases with μ compared to the calibration scenario. The number of empty crossings is smaller than the expected value causing an overestimate of μ .

As in the previous case, for $\mu > 5$ the statistical uncertainty becomes dominant due to limited size of the Monte Carlo sample.

8.5 Hit counting method

The basic idea of a hit counting method is to correlate μ to the number of particles typically produced in a pp collision by counting the number of LUCID tubes hit. The number of particles in a bunch is expected to scale with the number of collisions occurred in the bunch. As a consequence, also the number of hit tubes is expected to scale in the same way.

A drawback of this method is that the detector counts hits rather than particles: if a tube is traversed by two or more particles, it counts only one hit. Since the number of hits per bunch is limited to a maximum of 32, a saturation effect is expected when the number of simultaneous collisions in a bunch increases. Under certain assumptions, this effect can be parametrized.

8.5.1 Single side mode

Calculation

The average number of pp interactions per bunch crossing can be written as:

$$\mu = \frac{N_{particles/BX}}{N_{particles/pp}} \quad (8.19)$$

where $N_{particles/BX}$ is the average number of particles per bunch crossing and $N_{particles/pp}$ is the average number of particles per single interaction.

From hits to particles. A signal generated by two or more particles crossing the same tube is not distinguished by the signal of a single particle. The maximum number of particles which can be registered by the detector corresponds to the number of tubes ($N_{tubes} = 32$). This leads to a *saturation* effect of the hit counting method, arising when the average number of interactions goes beyond a certain value.

By taking into account all combinations of particles going through the tubes, saturation effect can be parametrized. The way particles distribute

among the tubes depends to a certain extent on the dynamics of the interactions: single- and double-diffractive, non diffractive etc. Assuming that particles spread uniformly over the detector, the average number of particles hitting one tube is $N_{particles}/N_{tubes}$, where $N_{particles}$ is the total number of detected particles.

Assuming that particles distribute according to a Poissonian, the probability to have at least one particle in a tube, namely a hit, is:

$$1 - e^{-\frac{N_{particles}}{N_{tubes}}} \quad (8.20)$$

Such probability is turned into number of hits with the following formula:

$$N_{hits} = N_{tubes} \left[1 - e^{-\frac{N_{particles}}{N_{tubes}}} \right] \quad (8.21)$$

Equation 8.21 allows to extract the number of particles registered in the detector from the number of hits by using the following relation:

$$N_{particles} = -N_{tubes} \log \left(1 - \frac{N_{hits}}{N_{tubes}} \right) \quad (8.22)$$

Using Equation 8.22, Equation 8.19 can be written as:

$$\mu = \frac{\log \left(1 - \frac{N_{hits/BX}}{N_{tubes}} \right)}{\log \left(1 - \frac{N_{hits/pp}}{N_{tubes}} \right)} \quad (8.23)$$

where the number of hits per single interaction $N_{hits/pp}$ is measured during calibration runs. The value of $N_{hits/pp}$ for single side mode is reported in Table 8.1.

Results

The average number of interactions per bunch crossing measured (μ_{meas}) with the hit counting method in single side mode is extracted from 10 Monte Carlo samples having different μ_{true} , for four values of the threshold, using Equation 8.23 (see Figure 8.6).

For $\mu < 1$, the agreement between the measured and the expected number of interactions is within 2.6%, when a threshold of 50 p.e. is set.

For larger values of μ , the disagreement increases exponentially due to migration effect which causes an overestimate of μ .

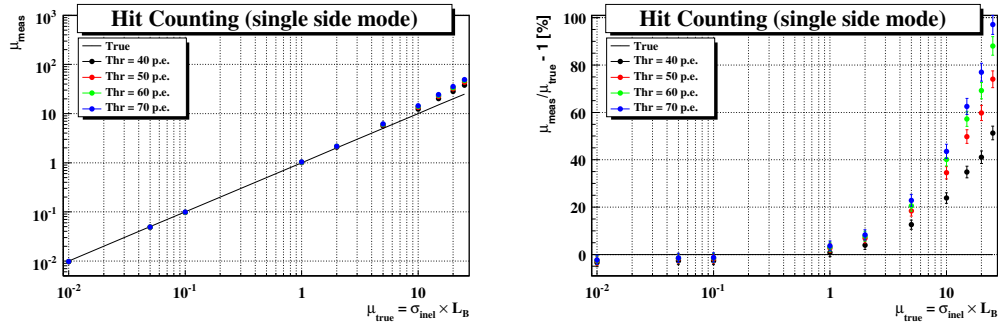


Figure 8.6: Average number of interactions per bunch crossing measured by counting the number of hits per bunch crossing when interactions are detected in single side mode (left), and difference from the expected value (right).

8.5.2 Coincidence mode

In coincidence mode, there are two possibilities to detect a bunch with multiple interactions.

A *true* coincidence occurs when at least one interaction is detected simultaneously in both modules.

A *fake* coincidence occurs when no interaction is detected simultaneously in both modules, but at least two interactions are separately detected in different modules.

Calculation

In coincidence mode, the average number of detected particles in a bunch with n interactions is the sum of two contributions:

- I - the bunch contains at least one interaction which is detected in both modules, together with any number of interactions which are only detected in module A and not in C, and viceversa;
- II - the bunch contains 0 interactions detected in both modules, together with at least one interaction which is only detected in module A and one which is only detected in module C.

The average number of particles corresponding to terms I and II is the sum of the probability of each configuration times the corresponding number of detected interactions, times the number of particles per detected interaction.

Four *exclusive* definitions of average number of particles per detected interaction are used (Table 8.3).

C_1	no. of particles per detected interaction in A, but not in C
C_2	no. of particles per detected interaction in C, but not in A
C_3	no. of particles per detected interaction in both modules
C_4	no. of particles per detected interaction in one module, not in both

Table 8.3: *Exclusive definitions of average number of particles.*

The probability of each configuration is evaluated by using the efficiencies to detect an interaction defined in Table 8.2 (ε_1 , ε_2 , ε_3 and ε_0), together with the efficiency to detect an interaction in one module, but not in both (ε_4).

Terms I and II can be written as:

$$I = \sum_{k=1}^n \varepsilon_3^k \binom{n}{k} \left[\sum_{l=0}^{n-k} \varepsilon_4^l (1 - \varepsilon_4 - \varepsilon_3)^{n-k-l} \binom{n-k}{l} \right] [kC_3 + lC_4] \quad (8.24)$$

$$II = \sum_{k=1}^n \varepsilon_1^k \binom{n}{k} \left[\sum_{l=1}^{n-k} \varepsilon_2^l \varepsilon_0^{n-k-l} \binom{n-k}{l} \right] [kC_1 + lC_2] \quad (8.25)$$

Suppose n interactions occurred in a bunch crossing.

Term I The first contribution consists of k interactions detected in both modules, l of the remaining $n - k$ interactions detected in only one module and the remaining $n - k - l$ interactions undetected.

The probability of detecting k interactions in both modules is ε_3^k . The probability of detecting l interactions in only one module is ε_4^l . The probability of not detecting $n - k - l$ interactions is $(1 - \varepsilon_4 - \varepsilon_3)^{n-k-l}$.

Binomial factors are used to account for all permutations of k out of n interactions and l out of $n - k$ interactions.

The average number of particles given by k interactions detected in both modules is kC_3 , while that of l interactions detected in one module is lC_4 .

Term II The second contribution consists of k interactions detected in module A but not in C, l of the remaining $n - k$ interactions detected in module C but not in A, and the remaining $n - k - l$ interactions undetected.

The probability of detecting k interactions in module A is ε_1^k . The probability of detecting l interactions in module C is ε_2^l . The probability of not detecting $n - k - l$ interactions is ε_0^{n-k-l} .

Binomial factors are used to account for all permutations of k out of n interactions and l out of $n - k$ interactions.

The average number of particles given by k interactions detected in both modules is kC_1 , while that of l interactions detected in one module is lC_2 .

Sum over l The l -sums in Equations 8.24 and 8.25 can be evaluated by means of the binomial theorem:

$$kC_3 \sum_{l=0}^{n-k} \varepsilon_4^l (1 - \varepsilon_4 - \varepsilon_3)^{n-k-l} \binom{n-k}{l} = kC_3(1 - \varepsilon_3)^{n-k} \quad (8.26)$$

$$C_4 \sum_{l=0}^{n-k} l \varepsilon_4^l (1 - \varepsilon_4 - \varepsilon_3)^{n-k-l} \binom{n-k}{l} = C_4(n-k)\varepsilon_4(1 - \varepsilon_3)^{n-k-1} \quad (8.27)$$

$$kC_1 \sum_{l=1}^{n-k} \varepsilon_2^l \varepsilon_0^{n-k-l} \binom{n-k}{l} = kC_1 [(\varepsilon_0 + \varepsilon_2)^{n-k} - \varepsilon_0^{n-k}] \quad (8.28)$$

$$C_2 \sum_{l=1}^{n-k} l \varepsilon_2^l \varepsilon_0^{n-k-l} \binom{n-k}{l} = C_2(n-k) \varepsilon_2(\varepsilon_0 + \varepsilon_2)^{n-k-1} \quad (8.29)$$

Sum over k Equations 8.26-8.29 are used to evaluate the k -sums in Equations 8.24 and 8.25 by means of the binomial theorem:

$$C_3 \sum_{k=1}^n k \varepsilon_3^k (1 - \varepsilon_3)^{n-k} \binom{n}{k} = C_3 \varepsilon_3 n \quad (8.30)$$

$$C_4 \varepsilon_4 \sum_{k=1}^n n \varepsilon_3^k (1 - \varepsilon_3)^{n-k-1} \binom{n}{k} = C_4 \varepsilon_4 n \left[\left(\frac{1}{1 - \varepsilon_3} \right) - (1 - \varepsilon_3)^{n-1} \right] \quad (8.31)$$

$$-C_4 \varepsilon_4 \sum_{k=1}^n k \varepsilon_3^k (1 - \varepsilon_3)^{n-k-1} \binom{n}{k} = -C_4 \varepsilon_4 n \frac{\varepsilon_3}{1 - \varepsilon_3} \quad (8.32)$$

$$C_1 \sum_{k=1}^n k \varepsilon_1^k (\varepsilon_0 + \varepsilon_2)^{n-k} \binom{n}{k} = C_1 \varepsilon_1 n (\varepsilon_0 + \varepsilon_1 + \varepsilon_2)^{n-1} \quad (8.33)$$

$$-C_1 \sum_{k=1}^n k \varepsilon_1^k \varepsilon_0^{n-k} \binom{n}{k} = -C_1 \varepsilon_1 n (\varepsilon_0 + \varepsilon_1)^{n-1} \quad (8.34)$$

$$C_2\varepsilon_2 \sum_{k=1}^n n\varepsilon_1^k (\varepsilon_0 + \varepsilon_2)^{n-k-1} \binom{n}{k} = C_2\varepsilon_2 n \left[\frac{(1 - \varepsilon_3)^n}{\varepsilon_0 + \varepsilon_2} - (\varepsilon_0 + \varepsilon_2)^{n-1} \right] \quad (8.35)$$

$$-C_2\varepsilon_2 \sum_{k=1}^n k\varepsilon_1^k (\varepsilon_0 + \varepsilon_2)^{n-k-1} \binom{n}{k} = -C_2\varepsilon_2 n\varepsilon_1 \frac{(1 - \varepsilon_3)^{n-1}}{\varepsilon_0 + \varepsilon_2} \quad (8.36)$$

Sum of terms I and II Given that $C_1\varepsilon_1$ is the number of particles registered in the whole detector when the interaction is detected in module A only and $C_2\varepsilon_2$ is the number of particles registered in the whole detector when the interaction is detected in module C only, the sum of these terms gives the number of particles registered in the whole detector when the interaction is detected in module A or in module C but not in both:

$$C_4\varepsilon_4 = C_1\varepsilon_1 + C_2\varepsilon_2 \quad (8.37)$$

Using Equation 8.37, the sum of Equations 8.30-8.36 results:

$$I + II = C_3\varepsilon_3 n + C_1\varepsilon_1 n \left[1 - (\varepsilon_0 + \varepsilon_1)^{n-1} \right] + C_2\varepsilon_2 n \left[1 - (\varepsilon_0 + \varepsilon_2)^{n-1} \right] \quad (8.38)$$

Poissonian sum The average number of particles per bunch is given by the convolution of Equation 8.38 with a Poissonian of average μ :

$$N_{particles/BX} = \sum_{n=0}^{\infty} (I + II) \frac{e^{-\mu} \mu^n}{n!} \quad (8.39)$$

Given the relations:

$$\sum_{n=0}^{\infty} n \frac{e^{-\mu} \mu^n}{n!} = \mu \quad \text{and} \quad \sum_{n=0}^{\infty} \frac{k^n}{n!} = e^k \quad (8.40)$$

Equation 8.39 becomes:

$$N_{particles/BX} = C_3\varepsilon_3 \mu + C_1\varepsilon_1 \mu \left[1 - e^{-\mu(\varepsilon_2 + \varepsilon_3)} \right] + C_2\varepsilon_2 \mu \left[1 - e^{-\mu(\varepsilon_1 + \varepsilon_3)} \right] \quad (8.41)$$

C^A	no. of particles per detected interaction in A
C^C	no. of particles per detected interaction in C
C^{Coin}	no. of particles per detected interaction in both modules

Table 8.4: *Inclusive definitions of average number of particles.*

The *inclusive* average numbers of particles are defined in Table 8.4.

Using Equation 8.9 and the following relations

$$\begin{aligned} C_1\varepsilon_1 &= C^A\varepsilon^A - C^{Coin}\varepsilon^{Coin} \\ C_2\varepsilon_2 &= C^C\varepsilon^C - C^{Coin}\varepsilon^{Coin} \end{aligned} \quad (8.42)$$

Equation 8.41 can be written as:

$$\begin{aligned} N_{particles/BX} &= \mu C^{Coin}\varepsilon^{Coin} + \\ &\mu C^{Coin}\varepsilon^{Coin} \left(\frac{C^A\varepsilon^A}{C^{Coin}\varepsilon^{Coin}} - 1 \right) \left(1 - e^{-\mu\varepsilon^C} \right) + \\ &\mu C^{Coin}\varepsilon^{Coin} \left(\frac{C^C\varepsilon^C}{C^{Coin}\varepsilon^{Coin}} - 1 \right) \left(1 - e^{-\mu\varepsilon^A} \right) \end{aligned} \quad (8.43)$$

The average number of particles defined in Table 8.4 and used in Equation 8.43 are obtained converting the corresponding number of hits from Table 8.1 into particles by using Equation 8.22.

Results

The average number of interactions per bunch crossing measured (μ_{meas}) with the hit counting method in single side mode is extracted from 10 Monte Carlo samples having different μ_{true} , for four values of the threshold, using Equation 8.43. The average number of particles per bunch ($N_{particles/BX}$) is obtained converting the number of hits registered by the detector by means of Equation 8.22. The result is shown in Figure 8.7.

Already at $\mu = 1$, the disagreement between the measured and the expected number of interactions is 6%, when a threshold of 50 p.e. is set.

For larger values of μ , the disagreement increases exponentially due to migration effect which causes an overestimate of μ .

8.6 Ad-hoc parameterization method

The counting methods presented in the previous sections have a limited range of applicability in terms of μ . As a matter of fact, the average number of

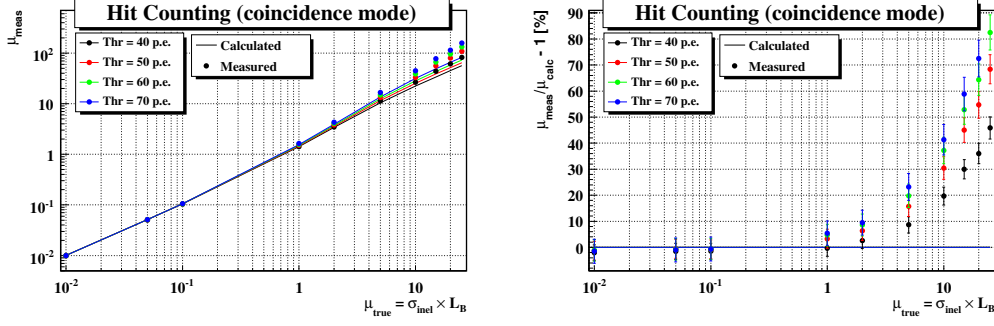


Figure 8.7: Average number of interactions per bunch crossing measured by counting the number of hits per bunch crossing when interactions are detected in coincidence mode (left) and difference from the expected value (right).

hits per bunch crossing ($N_{hits/BX}$) has three reasons to be non-linear with μ :

- I - Saturation effect due to hit counting instead of particle counting;
- II - Combinatorial effects arising in coincidence mode;
- III - Migration above threshold of small signals at high μ .

The first two effects can be analytically calculated, so one can apply corrections. The migration effect produces a consistent overestimate of μ (already at $\mu = 1$ for hit counting in coincidence mode) which has not been numerically evaluated.

The accuracy of the luminosity monitor increases for $\mu > 1$ by parametrizing all non-linear effects with a *calibration curve*. In other words, the method is based on the evaluation of a calibration function rather than a calibration constant. The calibration curve is obtained by fitting the average number of hits registered by LUCID at different luminosities:

$$N_{hits/BX} = f(\mu) \quad (8.44)$$

The inverse of the fit function 8.44 is used in the measurement scenario to evaluate the average number of interactions per bunch crossing corresponding to a given average number of hits collected with the detector:

$$\mu = f^{-1}(N_{hits/BX}) \quad (8.45)$$

For this purpose, the Monte Carlo sample is divided into two equal subsets of events. Each set is used to build 10 samples of multiple interaction events by overlapping events according to a Poissonian distribution with $\mu_{true} = 0.01, 0.05, 0.1, 1, 2, 5, 10, 15, 20, 25$. One of the two samples is used for the calibration fit (Equation 8.44), the other simulates the measurement scenario and is used to test the performance of luminosity monitoring (Equation 8.45).

8.6.1 Single side mode

Figure 8.8 shows the results of Monte Carlo simulations where the average number of hits per bunch crossing ($N_{hits/BX}$) registered in single side mode is plotted as a function of the number of interactions μ_{true} .

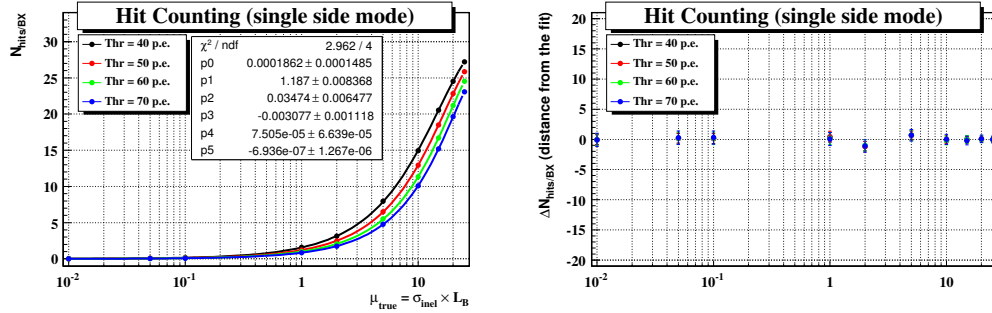


Figure 8.8: *Fifth order polinomial fit of $N_{hits/BX}$ registered in LUCID as a function of μ_{true} (left). Deviation of the points from the fit (right).*

A fifth order polinomial of $N_{hits/BX}$ as a function of μ_{true} fits well the measured points: the maximum deviation from the fit is 1% and represents the systematic uncertainty associated to the inversion of the fit function.

At the optimal threshold (50 p.e.), the maximum deviation from linearity is 3% and represents a systematic uncertainty of the method.

8.6.2 Concidence mode

Figure 8.10 shows the results of Monte Carlo simulations where the average number of hits per bunch crossing ($N_{hits/BX}$) registered in coincidence mode is plotted as a function of the number of interactions μ_{true} .

A fifth order polinomial of $N_{hits/BX}$ as a function of μ_{true} fits well the measured points: the maximum deviation from the fit is 3% and represents the systematic uncertainty associated to the inversion of the fit function.

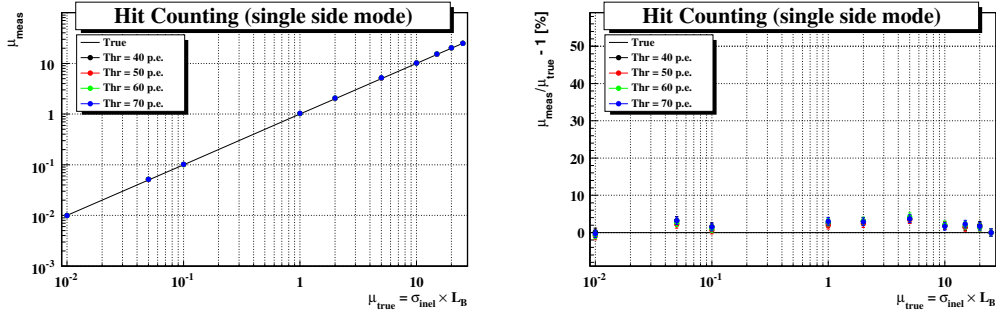


Figure 8.9: Measured number of interactions per bunch crossing as a function of the expected value, measured with a hit counting method in single side mode by using a calibration curve (left). Deviation from linearity (right).

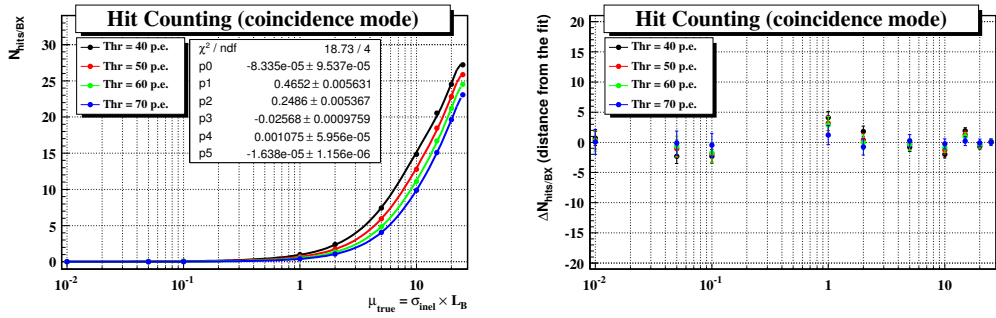


Figure 8.10: Fifth order polinomial fit of $N_{hits/BX}$ registered in LUCID as a function of μ_{true} (left). Deviation of the points from the fit (right).

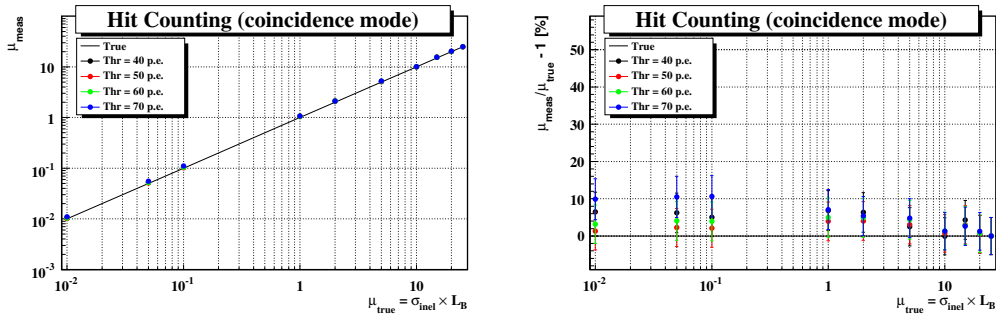


Figure 8.11: Measured number of interactions per bunch crossing as a function of the expected value, measured with a hit counting method in coincidence mode by using a calibration curve (left). Deviation from linearity (right).

At the optimal threshold (50 p.e.), the maximum deviation from linearity is 4% and represents a systematic uncertainty of the method.

Calibration from a low luminosity data sets

To be less dependent from Monte Carlo simulations, the multiparameter hit counting method can be calibrated with data. The response of LUCID to single interaction events (average number of hits per bunch crossing) can be sampled during calibration runs at such low luminosity that the probability of having more than one interaction per event is negligible.

However, the *calibration curve* presents some issues.

It requires stable running conditions. Once calibrated, the procedure may give wrong results if internal or external conditions change (such as gain in the electronics chain, activation of the material etc.).

This problem can be partially addressed repeating the calibration on a regular basis. However, calibration runs cannot be performed frequently since they require an accelerator tuned down in luminosity (not easy to foresee, especially once the accelerator reaches a stable high luminosity performance).

Another issue is that calibration might need an external trigger. In order to reproduce correctly the migration above threshold of the small signals taken during calibration runs, the detector cannot trigger on its own signals. An external *unbiased* trigger is needed to select those interactions in which some activity was registered in LUCID but was not enough to trigger on. However, the external trigger is not requested to be fully efficient for inelastic collision (it would be actually a good competitor of LUCID), rather it must be *unbiased*. This means that it must keep the relative weight of all inelastic sub-processes identical to those at generation level: single diffractive, double diffractive, non-diffractive etc.

Finally, the method relies on the Poissonian distribution of the interaction rate. Any deviation from this behaviour may cause loss in accuracy.

The advantage of this procedure is that it is *self-calibrating* to some extents. It can provide an estimate of the average number of inelastic *pp* collisions per bunch crossing without relying on an independent measurement of absolute luminosity. In turns, this means that the independent measurement of luminosity can be used to provide a measurement of inelastic *pp* cross section:

$$\sigma^{inel} = \frac{\mu_{LUCID}}{L_{external}} \quad (8.46)$$

This measurement can be done in the early stage of the LHC machine, with the absolute luminosity provide by the van der Meer scan, a high statis-

tics calibration run at low luminosity with an *interaction* trigger, and a luminosity monitor capable of extrapolating luminosity from calibration run to a high statistics physics run for the measurement of cross section.

8.7 Conclusions

Several methods for monitoring luminosity with LUCID have been presented.

Two methods are based on a Monte Carlo calibration: a zero counting method based on detection of empty bunch crossings and a hit counting method based on the average number of hits registered in the detector.

A third method, also based on hit counting, is calibrated with low luminosity data ($\mu \ll 1$) and is to large extent independent from Monte Carlo simulations.

The performances of all methods are evaluated using different Monte Carlo simulations and two different criteria to detected an interaction. In single side mode, the interaction is detected if at least one module registers a hit. In coincidence mode, the interaction is detected only if both modules register a hit simultaneously.

All methods provide a measurement of the average number of interactions per bunch crossing which is compared to the corresponding Monte Carlo truth. The systematic deviation from linearity of the different methods is reported in Table 8.5.

	Mode	Calibration	Range	Systematics
Zero Counting	Single Side	Monte Carlo	$\mu < 2$	1%
Zero Counting	Coincidence	Monte Carlo	$\mu < 1$	2%
Hit Counting	Single Side	Monte Carlo	$\mu < 1$	2.6%
Hit Counting	Coincidence	Monte Carlo	$\mu < 1$	6%
Hit Counting	Single Side	Data	any μ	3%
Hit Counting	Coincidence	Data	any μ	4%

Table 8.5: *Systematic uncertainty of luminosity monitoring with LUCID for different methods and range of validity.*

Due to the migration effect, which is not analytically calculated, the first four methods prove to be rather inefficient when the number of interactions is larger than 1, independently of the detection mode (single side or coincidence).

For $\mu < 1$, the best method based on Monte Carlo calibration is zero counting in single side mode (1% accuracy).

For $\mu > 5$, the only usable method is the one calibrated with data, with an accuracy of 3% in single side mode.

Chapter 9

Conclusions

The work described in this thesis is concerning the luminosity measurement in the ATLAS experiment.

The present work concerns the development and maintaining of the Detector Control System for LUCID and the study of the performance of LUCID as a luminosity monitor.

LUCID is the main luminosity monitor of the ATLAS experiment. The detector consists of two modules placed symmetrically on both sides of the interaction point of ATLAS. Each module contains 20 aluminium tubes, about 1.5 m long and of 1.5 cm of diameter, containing C_4F_{10} for particle detection through Cerenkov effect. Light detection and collection is performed by means of photomultipliers. The Cerenkov radiator technique is radiation hard and allows fast response of the detector, so as to follow each bunch crossing (40 MHz). LUCID covers a pseudo-rapidity range [5.61, 5.92].

The tubes are pointing to the interaction point of ATLAS in order to allow background suppression: primary particles emerging from the interaction point are expected to travel inside the tubes along paths parallel to the axis, whereas secondary particles generated by interaction of primary particles with the material surrounding LUCID are expected to enter the tubes through the lateral walls. Primaries are then expected to emit more Cerenkov light than secondaries. Test beams measurements confirm the validity of the pointing geometry: a particle crossing the tube with an angle of 6° emits 25% less photoelectrons than a particle travelling along the tube axis.

Luminosity calculations are performed by the LUMAT card. Luminosity values are provided both for each one of the 3564 bunches and for the sum of all bunches; values are integrated over a luminosity block while taking into account busy conditions and dead-times. The LUMAT card may run in parallel four algorithms, and allows tuning of the algorithms at later stages. The work of this thesis addresses the study, the optimization and the validation

of these algorithms. The LUCID trigger is also handed over by the LUMAT card.

The safe operation of LUCID is ensured by the Detector Control System. Software tools like scripts and panels monitor continuously the status of the detector, avoid issuing of potentially dangerous commands and set alarms if an error condition arises. Crucial parameters like high and low voltage channels and pressure of the vessels are stable within 1 %. Temperature is also monitored, especially during critical periods like the bake-out procedure of the beam pipe. Communication with the TDAQ is also active. The LUCID DCS is fully integrated into the ATLAS DCS. The Finite State Machine, which provides tools for integration and control in the ATLAS experiment, has also been implemented and successfully tested during the first beam event in September 2008.

In order to investigate the response of LUCID to pp collisions at 14 TeV center-of-mass energy at the interaction point of ATLAS, Monte Carlo simulations have been carried out. A primary particle (typically a pion) interacting with LUCID emits about 105 photoelectrons in the wavelength range [160 nm, 650 nm]. The gas accounts for about 75 photoelectrons, whereas the quartz window of the PMT is responsible for the remaining 30 photoelectrons. Background can be suppressed by setting a threshold on the number of photoelectrons. A tube registers a “hit” if the light yield of a particle is over a given threshold like for example 50 photoelectrons. In these conditions, the probability to detect inelastic pp collisions is $(55.8 \pm 0.05)\%$ if at least 1 hit is required (single side mode), and $(13.5 \pm 0.04)\%$ when coincidence between the two modules is required. This method is aimed at background suppression since particles generated in interactions of the beam with the residual gas, or beam halo interaction with the collimators are expected to leave a signal only in one side (uncorrelated). The average number of hits per collision registered in LUCID is 1.21, whereas the probability of registering a hit in a tube is $(3.66 \pm 0.01)\%$, more or less independently of the position of the tube.

Three basic methods for luminosity monitoring have been investigated: the zero counting method, the hit counting method and the “ad-hoc” parametrization. The zero counting method counts the fraction of empty bunch crossings. The main drawback of this method is the low rate of empty bunch crossings at high luminosity. The hit counting method counts the number of hits per bunch crossing. These two methods are affected by the migration effect: having set a threshold, the number of signals under threshold increases with the number of interactions per bunch crossing, giving as a result signals over threshold and, as a consequence, overestimation of the number of particles. This effect is already visible when the average number

of interactions per bunch crossing is of order 1. The hit counting method is also affected by the saturation effect: since the tubes register a hit even if two or more particles release a signal over threshold, the maximum number of hits registered can not exceed the number of tubes (32). When counting hits in coincidence mode, combinatorial effects arise. Finally, the “ad-hoc” parametrization method is based on calibration at low luminosity, i.e. conditions at which probability of having more than one interaction per bunch crossing is negligible. These single interaction events are then overlapped for different values of interactions μ per bunch crossing according to a Poissonian distribution and the corresponding number of hits is recorded as a function of μ . During measurement, the function is inverted and the number of interactions is obtained from the number of hits registered.

As a general result, the zero counting and the hit counting methods give their best performance only within a limited range of luminosities, whereas the “ad-hoc” method is valid over the whole dynamic range of LHC luminosity. In the range $\mu < 2$ the zero counting method in single side mode has an accuracy of $\sim 1\%$. The “ad-hoc” parametrization has an accuracy of $\sim 3\%$ in single side mode and $\sim 4\%$ in coincidence mode. The advantage of the “ad-hoc” parametrization is that it is independent of Monte Carlo. In order to work correctly, the method needs stable running conditions, an external trigger in order to reproduce correctly the migration of signals under threshold and no deviation from Poissonian behaviour of the interaction rate. The “ad-hoc” parametrization can provide measurement of the pp inelastic cross-section if a reliable estimate of the luminosity is available.

Bibliography

- [1] ALEPH, DELPHI, L3 and OPAL Collaborations, *Phys. Lett.* B565 (2003) 61.
- [2] The LEP Collaborations ALEPH, DELPHI, L3 and OPAL, the LEP Electroweak Working Group, the SLD Electroweak and Heavy Flavour Groups, A combination of preliminary electroweak measurements and constraints on the Standard Model, hep-ex/0312023; Updated numbers from the LEP Electroweak Working Group: <http://lepewwg.web.cern.ch/LEPEWWG>. The LEP Collaborations ALEPH, DELPHI, L3 and OPAL, the LEP Electroweak Working Group, Precision Electroweak Measurements and Constraints on the Standard Model, arXiv:0712.0929 [hep-ex], December 2007.
- [3] B.W. Lee et al., *Phys. Rev. Lett.* **38** (1977) 883;
M. Quiros, *Constraints on the Higgs boson properties from the effective potential*, hep-ph/9703412;
A. Ghinculov and T. Binoth, *Acta Phys. Polon.* **B30** (1999) 99.
- [4] L. Maiani, G. Parisi and R. Petronzio, *Nucl. Phys.* **B136** (1979) 115;
N. Cabibbo et al., *Nucl. Phys.* **B158** (1979) 295;
R. Dashen and H. Neunberger, *Phys. Rev. Lett.* **50** (1983) 1897;
D.J.E. Callaway, *Nucl. Phys.* **B233** (1984) 189;
M.A. Beg et al., *Phys. Rev. Lett.* **52** (1984) 883;
M. Lindner, *Z. Phys.* **C31** (1986) 295.
- [5] G. Altarelli and G. Isidori, *Phys. Lett.* **B337** (1994) 141;
J.A. Casas, J.R. Espinosa and M. Quiros, *Phys. Lett.* **B342** (1995) 171, *Phys. Lett.* **B383** (1996) 374;
B. Grzadkowski and M. Lindner, *Phys. Lett.* **B178** (1986) 81;
T. Hambye and K. Riesselmann, *Phys. Rev.* **D55** (1997) 7255.
- [6] <http://linac2.home.cern.ch/linac2/default.htm#one>

- [7] G. Arduini et al. *Standard filling schemes for various LHC operation modes* LHC-OP-ES-0003 (11 November 2004).
- [8] ATLAS Collaboration, *The ATLAS Physics TDR (Vol. I)* CERN/LHCC/99-14.
- [9] ATLAS Collaboration *Technical Proposal* CERN/LHCC/94-43 (16 December 1994).
- [10] ATLAS Collaboration, *The ATLAS Physics TDR (Vol. II)* CERN/LHCC/99-15.
- [11] ATLAS Collaboration, *Expected Performance of the ATLAS Experiment - Detector, Trigger, Physics* CERN-OPEN-2008-020 (2008).
- [12] ATLAS Collaboration, *ATLAS Forward Detectors for Measurement of Elastic Scattering and Luminosity*, ATLAS TDR 018, CERN/LHCC 2008-04 (2008).
- [13] A. K. Amundsen et al. *The control system of the OPAL detector at LEP*, Nucl. Inst. and Meth., **A293** 145-147 (1990).
- [14] A. Rosca *Standard Model Higgs Physics at Colliders* Romanian Reports in Physics **59-4** 987-1002 (2007).
- [15] *LHC Design Performance* EDMS CERN-0000020013.
- [16] S. Ask, D. Malon, T. Pauly, M. Shapiro, *ATLAS Report from the Luminosity Task Force* ATL-GEN-PUB-2006-002 (10 July 2006).
- [17] M. Month *Collider Performance with Ideal Collisions* Accel. Div. Report 85-1, D0 Note 201 (1985).
- [18] W. Herr, B. Muratori *Concept of luminosity*, CERN 2006-002 (2006) 361-377.
- [19] E. D. Courant, H. S. Snyder *Ann. Phys.*, **3**, 1 (1958).
- [20] H. Burkhardt, P. Grafstrom *Absolute Luminosity from Machine Parameters*, LHC Project Report 1019 (2007).
- [21] H. Schmickler *How to measure beam intensity?*, Talk given to Atlas 27 June 2005.
- [22] S. Van der Meer *Calibration of the effective beam height in the ISR* CERN-ISR-PO-68-31.

- [23] W. Herr *Dynamic behaviour of nominal and PACMAN bunches for different LHC crossing schemes*, LHC Project Report 856, CERN, Geneva 12/2005.
- [24] V. Papadimitriou *Luminosity measurements at hadron colliders* Nucl. Instr. and Meth. A **598** (2009) 14-18.
- [25] ATLAS Collaboration, *ATLAS Forward Detectors for Luminosity Measurement and Monitoring Letter of Intent* CERN/LHCC/2004-010 (22 March 2004).
- [26] S. Baranov et al., *Estimation of Radiation Background, Impact on Detectors, Activation and Shielding Optimization in ATLAS* ATL-GEN-2005-001.
- [27] P. Giovannini *LUCID beam test results*, Master Thesis at the Università di Bologna (Italy) (2008).
- [28] I. Chirikov-Zorin, I. Fedorko, A. Menzione, I. Sykora, S. Tokar *Nucl. Instr. and Meth. A* 461 (2001) 587-590.
- [29] A. Barriuso Poy et al. *The detector control system of the ATLAS experiment*, JINST **3** P05006 (2008).
- [30] H.J. Burckhart *ATLAS Detector Control System: User Requirements Document*, ATLAS DCS-URD1 (1995).
- [31] A. Barriuso Poy, S. Schlenker *ATLAS DCS - FSM Integration Guidelines*, (6 February 2007) ATL-DQ-ON-0010.
- [32] B. I. Hallgren, H. Boterenbrood, H. J. Burckhart, H. Kvedalen *The Embedded Local Monitor Board (ELMB) in the LHC Front-end I/O Control System* CERN report 2001-005 (2001).
- [33] J. D. Jackson *Classical Electrodynamics*, Wiley & Sons (1975).
- [34] S. Ask *Simulation of Luminosity Monitoring in ATLAS*, ATLAS LUM Internal Note (September 2005) ATL-LUM-PUB-2006-001.